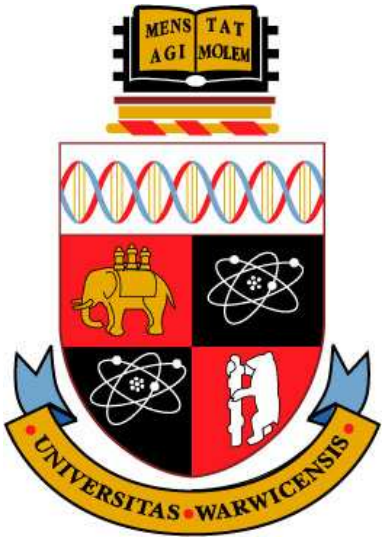

Transient Growth of Separated Flows

by

Christopher David Cantwell

Thesis

Submitted to the University of Warwick

for the degree of

Doctor of Philosophy

Centre for Scientific Computing

September 2009

THE UNIVERSITY OF
WARWICK

Contents

List of Figures **vii**

List of Tables **xi**

Acknowledgments **xiii**

Declarations **xiv**

Abstract **xv**

Abbreviations and Notation **xvi**

Chapter 1 Introduction **1**

1.1 Outline of Thesis 4

Chapter 2 Stability Analysis of Fluid Flow **6**

2.1 Overview 6

2.2 Local Stability Analysis 11

2.2.1 Ginzburg-Landau Model 12

2.3 Global Stability Analysis 14

2.4 A Global Approach to Convective Instability and Transient Growth . . . 16

2.4.1 Calculating Transient Growth 19
2.4.2 Adjoint Form of the Linearised Navier-Stokes Equations 21
2.4.3 Cylindrical Coordinates 25
2.4.4 Span-wise Wavenumber Dependence 26

Chapter 3 Numerical Techniques **28**

3.1 Spectral Element Formulation in One-Dimension 28
3.1.1 Domains and Elements 29
3.1.2 Method of Weighted Residuals 34
3.1.3 Numerical Integration 36
3.1.4 Numerical Differentiation 37
3.2 Implementation in One Dimension 37
3.2.1 Spectral Transforms 37
3.2.2 Discrete Derivative Operators 40
3.2.3 Global Assembly 42
3.2.4 Solving Linear Partial Differential Equations 43
3.3 Formulation in 2-Dimensions 45
3.3.1 Global Assembly 46
3.3.2 Two-dimensional Quadrature Points and Modes 49
3.3.3 Integration and Differentiation in 2D 50
3.3.4 Spectral Transforms and Operators in Two Dimensions 50
3.3.5 Derivative Operators 51
3.4 Copy Boundary Condition 53
3.4.1 Implementation 54
3.4.2 Example 58
3.5 Numerical Schemes for the Incompressible Navier-Stokes Equations . . . 60

3.5.1 Derivation . . . 60
3.5.2 Stiff Stability . . . 62
3.5.3 Pressure Correction Substep . . . 63
3.5.4 Flowrate control . . . 64
3.5.5 Streamwise Periodic Boundaries . . . 65
3.6 Eigenvalue Computation . . . 66
3.6.1 Eigenvalue Deflation . . . 70

Chapter 4 Transient Growth through a Sudden Expansion 74

4.1 Introduction . . . 74
4.2 Methodology . . . 77
4.2.1 Governing Equations and Flow Geometry . . . 77
4.2.2 Linear Stability and Transient Growth Problems . . . 79
4.2.3 Further Details . . . 83
4.3 Results . . . 87
4.3.1 Base Flows . . . 87
4.3.2 Linear Stability . . . 89
4.3.3 Transient Energy Growth . . . 90
4.3.4 Response to Noise . . . 103
4.4 Summary and Discussion . . . 109

Chapter 5 Convective Instability in Flow past a Cylinder 116

5.1 Introduction . . . 116
5.2 Formulation . . . 119
5.2.1 Linear Stability Analysis . . . 120
5.2.2 Transient Growth . . . 121

5.2.3 Numerical Method 121
5.3 Influence of Domain Size 122
5.3.1 Base Flow 123
5.3.2 Linear Stability 126
5.3.3 Transient Growth 126
5.3.4 Polynomial Order 127
5.3.5 Direct and Indirect Effects of Geometry 127
5.4 Quantitative Transient Growth Results 131
5.4.1 Base Flows 131
5.4.2 Global Stability 131
5.4.3 Transient Growth 132
5.5 Discussion 139

Chapter 6 Turbulent Puffs in a Gradually Expanding Pipe 143

6.1 Introduction 143
6.2 Methodology 147
6.2.1 Periodic Domain 147
6.2.2 Geometrical Configurations 147
6.2.3 Numerical Techniques 148
6.2.4 Boundary Conditions and Turbulence Generation 149
6.3 Results 149
6.3.1 Puff Structure 150
6.3.2 Large Reynolds Number Drop 152
6.3.3 Small Reynolds Number Drop 152
6.4 Discussion 157

Chapter 7 Summary and Future Work **159**

Appendix A Spectral Element Methods **161**

A.1 Jacobi Polynomials 161

A.1.1 Special Cases 163

A.2 Interpolation Polynomials 163

A.3 Nodal Bases 163

A.3.1 Zeros and Weights for Nodal Bases 164

A.4 Modal Bases 166

A.5 Global Assembly in 2D 166

A.6 Efficiency of 2D Matrix Systems 169

A.6.1 Computing the Diagonal Coefficients 170

Appendix B Spectral Element Heat Equation Formulation **172**

B.1 Solving the 1D Heat Equation with Forcing 172

B.1.1 Validation of Results 173

B.2 Solving the 2D Heat Equation 175

B.2.1 Validation of Results 176

List of Figures

1.1 A real-world fluid flow. 2

2.1 Local velocity profile. 7
2.2 Diagrams of the types of flow stability and instability. 8
2.3 Evolution of a perturbation in a shear flow. 8
2.4 Relation between local and global perspectives. 10
2.5 Instabilities of the Ginzburg-Landau equation with linear and quadratic coefficient μ. 14
2.6 Diagram of transient growth. 17

3.1 Diagram of a one-dimensional domain decomposition. 30
3.2 Basis of Lagrange interpolation polynomials. 33
3.3 Quadrature point ordering for a 2D element. 47
3.4 Global ordering for a two-dimensional element. 48
3.5 Diagram of the *copy boundary condition*. 53
3.6 Example of a *copy boundary condition* session file entry. 54
3.7 Code excerpt of the source data location routine. 56
3.8 Code excerpt of the source data retrieval routine. 57
3.9 Code excerpt of the routine to apply the boundary condition. 58

3.10 Example flow using the *copy boundary condition*. 59
3.11 Code excerpt to perform eigenvalue projection. 72

4.1 Sketch illustrating the evolution of a perturbation through an expanding pipe. 76
4.2 Geometry of the expanding pipe. 78
4.3 A spectral element mesh used in this study. 88
4.4 Contour plot of the base-flow streamfunction at $Re = 600$. 88
4.5 Relationship between downstream reattachment point x_r and Reynolds number for base flows with a fully-developed inlet profile. 89
4.6 Energy growth envelopes at Re=600 for azimuthal mode numbers up to m=6 92
4.7 Contours of optimal transient energy growth as a function of time horizon, τ, and Reynolds number. 94
4.8 Energy growth under linear evolution at Re=1200. 95
4.9 Evolution of optimal initial disturbance in the m=1 mode. 97
4.10 Evolution of optimal initial disturbance in the m=0 mode. 97
4.11 Physical interpretation of the maximal disturbance at Re=1200. 98
4.12 Optimal energy growth, $G_m^{\max}$, as a function of Re for each of the first four azimuthal modes. 99
4.13 Location of the centroid of the disturbance at its maximum growth. . . 101
4.14 Leading four growth envelopes for the optimal and suboptimal perturbations for the m=1 mode at Re=600. 103
4.15 Iso-surfaces of azimuthal velocity for the four leading perturbations at Re=600, m=1 evolved to time $t = 50$. 104
4.16 Modal energy in a noisy inflow DNS of the expanding pipe flow. 105

4.17 Visualisation of noise-driven flow and optimal perturbation. 107
4.18 Isosurfaces of streamwise, radial and azimuthal velocity components for the noise-driven flow. 107
4.19 Energy of noise-driven flow. 108
4.20 Radial profiles of velocity component standard deviations comparing the noise-driven simulation with the linear analysis. 109

5.1 Diagram of the cylinder geometry. 119
5.2 Convergence of the base flow stagnation point with mesh size. 124
5.3 Streamwise velocity profiles of base flows. 125
5.4 Convergence of critical eigenvalue with mesh size. 126
5.5 Convergence of optimal growth calculation with mesh geometry. 128
5.6 Elemental mesh determined necessary to attain an acceptable accuracy for transient growth calculations. 129
5.7 Streamlines of the base flow at Re=40. 132
5.8 Energy growth of perturbations. 133
5.9 Contour plot of perturbation growth. 134
5.10 Linear evolution of perturbations. 135
5.11 Maximum growth over all time horizons. 136
5.12 Contours of energy showing optimal initial condition. 137
5.13 Contours of energy showing evolved optimal perturbations. 138
5.14 Growth of perturbations against wavenumber at Re=40. 139
5.15 Contour plot of growth of perturbations for different spanwise wavelengths. 140

6.1 Schematic velocity traces for a puff and a slug. 144
6.2 Geometry of the puff generator (not to scale). 148

6.3 Computational mesh for the gradual expansion. 149
6.4 Turbulent puff at Re=2050. 151
6.5 Puff structure appearing at a downstream Reynolds number of $Re = 2200$.153
6.6 Streamwise velocity trace at $x = 250$. 154
6.7 Puffs at Re=1925. 156

A.1 Tree diagram showing the different options for expansion bases on the standard element. 169

B.1 Plot showing decay rate of numerical simulations of three different sine waves. Gradients match the decay rate results found through the analytical solution. 175
B.2 Plot showing decay rate of numerical simulations of three different two-dimensional sine functions. The gradient matches the decay rate found through Fourier analysis of the problem. 177

List of Tables

4.1 Streamwise position of base flow reattachment point at Re=1000. . . . 84

4.2 Leading eigenvalues for linear stability of flows in the 1 to 2 axisymmetric expansion for Reynolds numbers indicated. 90

4.3 Table of critical Reynolds numbers, Re_m^c, maximum growth values $G_m^{\max}$ and corresponding time horizons for maximum growth, $\tau_m^{\max}$. 93

4.4 Characteristics of the optimal perturbations at the time of maximum growth, $\tau^{\max}$, for m=1 modes. 101

5.1 Convergence of optimal growth with polynomial order. 128

5.2 Effect of mesh geometry and base flow on the evolution of perturbations. 131

List of Algorithms

1 Algorithm to produce the global assembly mapping - preprocessing. . . 167

2 Algorithm to produce the global assembly mapping. 168

Acknowledgments

First and foremost, I am immeasurably grateful to my supervisor, Professor Dwight Barkley, for the invaluable advice, dedication and support he has given me over the past years. Without his enthusiastic involvement and guidance, this thesis would not have been possible. I would also like to thank Hugh Blackburn for fruitful discussions and advice throughout my degree.

I acknowledge EPSRC for the financial support and the Centre for Scientic Computing for providing the computing facilities used throughout my postgraduate studies. I would like to thank the staff of both the Mathematics Institute and the Centre for Scientific Computing for their administrative and technical assistance.

I would like to extend my appreciation to all my friends and colleagues, who have assisted, encouraged and inspired me over the course of my degree. In particular, Paul Clifford, Dave Moxey and Brenda Quinn for many stimulating discussions. Special thanks also go to Silvia Liverani for copious amounts of proof-reading of meaningless mathematics.

Finally, I would like to thank my Mum and Dad for their unfaltering support and endless encouragement throughout the ups and downs.

Declarations

I declare that this thesis contains entirely my own research, conducted under the supervision of Dwight Barkley, except where stated otherwise. It has not been submitted for a degree at any other university. The material in Chapter 4 is from a paper submitted to the Physics of Fluids journal (Cantwell et al. [2009]).

Abstract

Transient growth is quantitatively examined in two prototype separated flows using Direct Numerical Simulation (DNS). Separated flows typically exhibit regions of convective instability due to the inflectional velocity profiles inherent in the shear flow. This can lead to the transient growth of small disturbances by many orders of magnitude.

After reviewing the mathematical tools and numerical techniques required, we present an analysis of transient growth in an axisymmetric pipe with a 1:2 diametral expansion. A direct method is used to calculate the optimal transient energy growth for specified time horizons and Reynolds numbers up to Re=1200, and low-order azimuthal wavenumber m. At each Re the maximum growth is in azimuthal mode m=1 and this maximum is found to increase exponentially with Re. The time evolution of optimal perturbations is presented and shown to correspond to sinuous oscillations of the shear layer. Finally, full three-dimensional DNS with the inflow perturbed with Gaussian white-noise confirms the presence of the structures determined by the transient growth analysis.

The second prototype flow considered is the cylinder wake in the subcritical regime. Large energy growth is observed at Reynolds numbers close to the onset of global instability and the optimal perturbations which lead to this growth are determined. Three-dimensional spanwise perturbations are also examined and it is found that, except for short time horizons, the zero wavenumber is dominant. Furthermore, performing accurate linear and transient growth analysis is found to be highly dependent on the size of the computational domain. Adjoint eigenmodes extend far upstream of the cylinder necessitating a long inflow. More importantly, constrictions in the cross-stream direction are found to distort the basic flow, which has a substantial effect on the accuracy of the analysis.

Transition in pipe flow is a topic for which there is still relatively little understanding. Puffs are small regions of turbulence observed close to the transitional Reynolds number. A gradually expanding pipe is proposed as a means to effectively produce turbulent puffs and study their creation and decay.

Abbreviations and Notation

The following abbreviations shall be used throughout this thesis:

Eqn.	Equation.
Fig.	Figure.
Sec.	Section.
DNS	Direct Numerical Simulation.
LHS	Left-hand side.
PDE	Partial Differential Equation.
Re	Reynolds number.
RHS	Right-hand side.

The following notational conventions shall be used to aid understanding throughout the discussion of spectral element methods in Chapter 3.

Indexing	
q, r	Physical space index
p	Spectral space index
k	Global index
$\boldsymbol{q}, \boldsymbol{r}$	Multi-index (physical space)
$\boldsymbol{p}$	Multi-index (spectral space)
$\boldsymbol{M}[j]$	Matrix column
$\boldsymbol{M}[i][j]$	Matrix element (row i,col j)
$\square$	Standard element quantity
$\square^e$	Element e quantity
$\square_g$	Global quantity

Symbol	Meaning
ξ	Independent variable on standard element
x	Independent variable on domain
u	Continuous physical space function
u^δ	Discretisation of u
v_j	Test space function
Ω	Domain
Ω^e	Element e
$\overline{\Omega}$	Standard element
χ_e	Mapping from standard element to element e
$\mathcal{P}_n(\Omega)$	Set of order-n polynomials on Ω.
ϕ	Local basis function
Φ	Global basis function
h_p	Lagrange interpolation basis (nodal)
ψ_p	Modal basis
$\boldsymbol{u}$	Physical space vector
$\hat{\boldsymbol{u}}$	Spectral coefficients vector
$\boldsymbol{B}$	Matrix of basis evaluations
$\boldsymbol{W}$	Quadrature weights matrix
$\boldsymbol{M}$	Mass Matrix
$\boldsymbol{D}$	Derivative coefficient matrix in 1D
$\boldsymbol{D}_1, \boldsymbol{D}_2$	Derivative matrices in 2D

Chapter 1

Introduction

In the real world fluid dynamics, such as that of an ocean wave, is very complex - too complex to be understood in every detail, whether through experiment, analysis or computation. Ultimately, these approaches can only ever hope to approximate certain aspects of these highly complex flows, either through selectively resolving particular aspects of the problem, or by simplifying the model sufficiently so that through analysis some meaningful conclusion can still be drawn. Nevertheless, important aspects of real-world flows can usually be understood by looking at prototype geometries, such as those considered in this thesis - a sudden expansion in a circular pipe and flow past a uniform circular cylinder. A limited number of key questions can then be posed to assess properties such as the stability of the flow, or the transient growth of perturbations. Through techniques of direct numerical simulation, we endeavour to compute hydrodynamic stability properties of these flows, both global and transient in nature, to better understand how these model problems behave and, by extension, how more complicated flows behave. This information is valuable in many engineering applications. Techniques such as flow control in industrial settings are one particularly important example.

Figure 1.1: A real-world fluid flow, such as an ocean wave, is too complex to be understood in every detail.

Hydrodynamic stability analysis is the process of examining the response of a flow to infinitesimal disturbances. Such disturbances may potentially cause the flow to transition from one state to another, such as from a laminar state to a turbulent state. This has been a focus of research for over a century with early studies of stability being either experimental or analytical in nature. Reynolds [1883] examined the transition from laminar flow to turbulence in a straight pipe, and Lord Rayleigh examined, among other flows, the instability of jets (Rayleigh [1878]) and of fluid interfaces (Rayleigh [1883]) - later to be known as the Rayleigh-Taylor instability.

Both experiment and analysis suffer drawbacks. Experimental observations are almost always hampered by noise in the system, making it challenging to assess critical parameter values with a high degree of accuracy. On the other hand, analytical approaches are limited by the complexity of the Navier-Stokes equations and the necessity of simplification. Only in the latter decades of the 20th Century have numerical techniques become viable. The processing capabilities of computers continue to increase dramatically, and they are now powerful enough to resolve the finer details of turbulent

flow in non-trivial geometries within a practical time frame. Computationally, stability was first treated from a local perspective, but with the increased availability of computing power, it is now feasible to resolve all the essential details of a flow to obtain a global stability theory.

In this thesis we focus on incompressible Newtonian fluids which are governed by the incompressible Navier-Stokes equations

$$\partial_t \boldsymbol{u} + (\boldsymbol{u} \cdot \nabla)\boldsymbol{u} = -\nabla p + \nu \nabla^2 \boldsymbol{u}, \tag{1.1a}$$

$$\nabla \cdot \boldsymbol{u} = 0 \tag{1.1b}$$

where $\boldsymbol{u}$ is the fluid velocity and ν is the kinematic viscosity. In all cases considered the density, ρ, is constant and can be fixed at unity without any loss of generality. We are primarily concerned with open flows, i.e those in which particles pass through the domain of interest, as opposed to closed flows in which particles of fluid remain within the domain boundaries for all time. The methodologies used in our analysis will utilise the linearised form of these equations, which approximates the dynamics of infinitesimal perturbations to some basic flow. Through this we can establish the global stability, or instability, of this basic flow. Until recently, there lacked a cohesive theory relating the features obtained from local stability analysis, such as regions of convective and absolute instability, with the global framework for the stability problem. Direct optimal growth analysis provides a global perspective on convective instabilities. We consider such analysis for two flow problems: a sudden axisymmetric expansion, and flow past a circular cylinder. Both problems contain a separated region of the flow which is typically associated with a region of convective instability. This is effectively demonstrated through the optimal growth analysis.

1.1 Outline of Thesis

We now give a brief outline of the material to follow. In Chapter 2 we outline the fundamental details of the local and global stability analyses, augmented through the Ginzburg-Landau equation as a simplified model of hydrodynamic problems. We then give a rigorous formulation of the optimal growth methodology and how it might be structured around an existing Navier-Stokes solver. This discussion includes a comprehensive derivation of the adjoint linearised Navier-Stokes equations and appropriate boundary conditions. In many cases flow geometries may be more appropriately formulated in a cylindrical coordinate system, and so we discuss the auxiliary terms introduced through the expression of the Navier-Stokes equations in this form.

Chapter 3 discusses the numerical techniques used for conducting the optimal growth analysis. We use an existing spectral element implementation for the results presented in this thesis, but provide an overview of this discretisation technique in one and two dimensions. This first section concludes with details of the implementation of a new boundary condition to enforce a periodic region within part of the domain. The second section in this chapter provides the higher level numerical details of the multi-step discretisation of the Navier-Stokes equations and the Arnoldi-based algorithm used for computing eigenvalues of the linearised and adjoint Navier-Stokes operators. This section includes details of an implemented eigenvalue deflation algorithm.

Chapters 4 and 5 contain direct optimal growth analyses for a sudden expansion of a circular pipe, and flow past a uniform circular cylinder, respectively. These analyses have been performed using the methodologies outlined in Chapters 2 and 3. Both these flows exhibit energy growth of several orders of magnitude, promoted by the separation bubbles and associated shear layers. Chapter 6 contains the results of numerical simulations of the creation of turbulent puffs in a gradually expanding pipe. The expan-

sion provides an effective drop in Reynolds number which allows the formation of such phenomena through transition from a turbulent state to a laminar state.

In conclusion, Chapter 7 discusses the results obtained in the preceding chapters, along with potential avenues of future research.

Chapter 2

Stability Analysis of Fluid Flow

2.1 Overview

We will begin by giving a brief summary of two approaches to stability analysis of open flows. Flow stability may be considered from a local or global perspective and, through such analyses, we can determine the control parameters, such as the Reynolds number, at which different state bifurcations occur. We will then focus on a global approach to assessing convective instability in open flows.

Parallel viscous flows have been studied throughout the 20th century with early examples being solutions to the Orr-Sommerfeld equations. There is a wide literature on the analysis of parallel flows with an extensive review being given by Drazin and Reid [1981]. Local stability analysis was originally developed in the context of plasma physics (see, for example, Briggs [1964] and Bers [1975]) to distinguish convective and absolute instabilities in plasmas. The technique has also appeared in the context of geophysical flows, and only in the 1980s did it first appear in the hydrodynamical literature. Huerre and Monkewitz [1990] give a comprehensive early history. The methodology is described

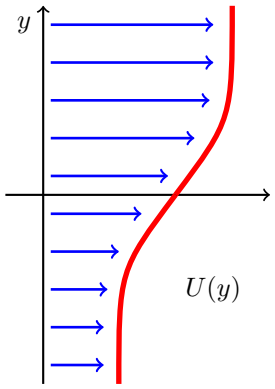

Figure 2.1: Local velocity profile. Local analysis examines the stability of the velocity profile $U(y)$ at a given streamwise station.

by Schmid and Henningson [2001], with Cossu and Chomaz [1997] and Chomaz [2005] giving a detailed theoretical description in the context of applications.

In such analysis the susceptibility of the flow to instability at a particular streamwise station in the flow is determined by examining the stability of the parallel velocity profile at that point (see Fig. 2.1). Regions of the domain may then be classified into one of three categories:

- locally stable;
- convectively unstable;
- absolutely unstable.

At a given station, x, the flow is considered locally stable if a fictitious parallel flow with profile matching that at station x is stable. In such flows all disturbances always dissipate with time. If such a parallel flow is unstable, but a disturbance propagates upstream or downstream, such that at a given spatial location the flow eventually returns to the basic state, the flow at that point is considered convectively unstable. On the other hand, if at that fixed streamwise station the magnitude of the disturbance grows

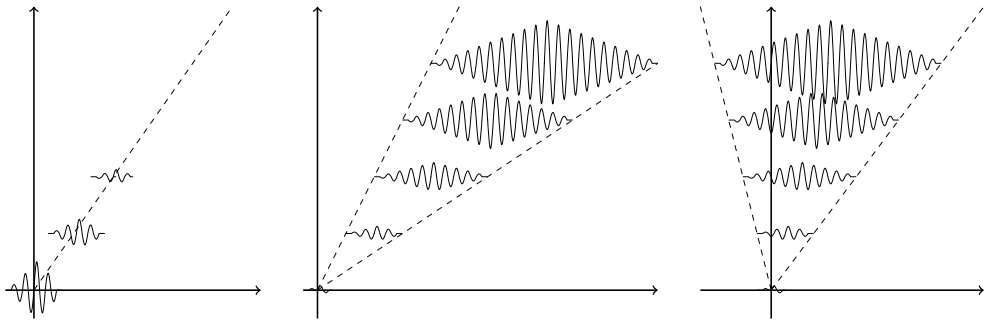

Figure 2.2: Diagrams of the types of flow stability and instability. In locally stable regions (left), the disturbance decays. In convective instability (middle), the disturbance grows as it is advected downstream, but at each streamwise station, the flow returns to its original state as $t \to \infty$. In absolute instability (right), the disturbance at a fixed point grows in time.

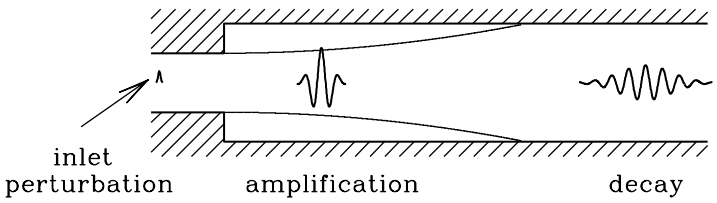

Figure 2.3: Evolution of a perturbation in a shear flow. The perturbation grows in one region of the flow, while decaying in another.

with time, it is described as absolutely unstable. This can be effectively seen in Fig. 2.2. However, this local approach is only valid when the flow is approximately parallel - that is, it varies slowly in the streamwise direction on a length scale comparable to the wavelength of the instability waves. For model flows such as mixing layers and Poiseuille flow, this is a good approximation. Inflectional velocity profiles, such as shear layers and wakes, are typically associated with locally convective and absolute instabilities. However, the velocity profiles of wakes rarely vary slowly and consequently, for many open flow problems, the local approach is not a valid approximation.

Global linear stability analysis resolves all aspects of the flow enabling a basic

flow to be classified as either globally stable or globally unstable, as indicated by the sign of the leading eigenvalues of the associated linear operator. This basic flow and any transported perturbations are considered the result of the interaction of global modes. Early uses of global stability techniques in the context of the cylinder wake are Noack and Eckelmann [1994] and Barkley and Henderson [1996]. The former establishes the stability of the linearised Navier-Stokes operator through direct eigenvalue computation (for example, using algorithms from Press et al. [1992]) while the latter uses an iterative time-steppers approach. This iterative approach to global stability analysis is comprehensively described in Tuckerman and Barkley [2000]. More recent studies (for example Marquet et al. [2008a], Marquet et al. [2008c] and Ehrenstein and Gallaire [2005]) typically use this method to compute global modes, since highly refined computational meshes on more complex geometries make the direct approach too costly. This technique is extended to the transient growth problem providing a global approach to establishing the presence of convective instability. The transient growth process was first proposed by Kelvin [1887] and explored by Orr [1907]. However, it is only in the last thirty years that a more detailed understanding of the mechanism behind this phenomenon has been achieved. It has recently been applied to a wide variety of applications such as the backward-facing step (Blackburn et al. [2008a]), stenotic flow (Blackburn et al. [2008b]), curved channels (Marquet et al. [2008b]) and the circular cylinder in the unstable regime (Abdessemed et al. [2009]).

The local and global perspectives do not necessarily coincide. There is an ongoing contest between the local instability which is liable to destabilise the flow, and the global advection promoting stability by drawing disturbances away from the unstable regions.

While a globally unstable flow must necessarily expose a region of local absolute instability (Chomaz et al. [1991]), a flow with a sufficiently small pocket of local abso-

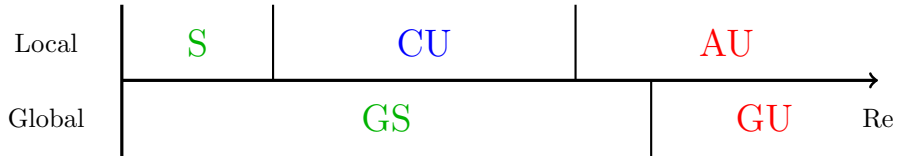

Figure 2.4: The local and global perspectives do not necessarily coincide, with a finite region of local absolute instability being necessary for global instability.

lute instability may remain globally stable as shown in Fig. 2.4. This is demonstrated efficaciously by Pier [2002] and Giannetti and Luchini [2007] for the prototype flow past a circular cylinder in which a region of absolute instability develops at Reynolds number 25, while the flow remains globally stable until Reynolds number ≈ 47. In the context of shear layers and separation bubbles Hammond and Redekopp [1998] report the onset of absolute, and ultimately global, instability with increased reverse flow. Such inflectional profiles are well known for being convectively unstable and imposing large transient amplifier dynamics upon perturbations in the shear layer. One prototype flow demonstrating this is the flow through a sudden axisymmetric expansion which is considered in Chapter 4; other examples will be discussed later.

This thesis is primarily concerned with the global techniques. We will first give an overview of the local stability analysis technique and describe the Ginzburg-Landau model as a prototype equation for demonstrating many of the fundamental concepts, before introducing global stability analysis. The remaining discussion in this chapter will then concern the use of global techniques to determine convective instabilities in flows which are traditionally considered globally stable.

2.2 Local Stability Analysis

For this type of analysis the velocity profile at any given streamwise location must vary slowly in the direction of flow, in accordance with the Wentzel-Kramers-Brillouin-Jeffreys (WKBJ) theory. Typically, the basic flow has a profile $U(y, Re)$ extending indefinitely in the streamwise direction. The linearised Navier-Stokes equations, $\mathcal{H}$, acting on a flow perturbation, $\boldsymbol{u}'(x,t)$, may be expressed in the form

$$D\left[i\frac{\partial}{\partial t}, -i\frac{\partial}{\partial x}; Re\right]\boldsymbol{u}'(x,t) = \mathcal{H}\boldsymbol{u}'(x,t) = 0,$$

with an associated dispersion relation,

$$D[\omega, k; Re] = 0,$$

governing the relationship between the wavenumbers, k, and the frequencies, ω, of the instability waves. The temporal modes, $\omega(k, Re)$, may be determined as a function of wavenumber, and the spatial branches, $k(\omega, Re)$, as a function of frequency. The impulse response, $G(x,t)$, of the flow determines whether the profile is convectively or absolutely unstable, and is given by

$$D\left[i\frac{\partial}{\partial t}, -i\frac{\partial}{\partial x}; Re\right]G(x,t) = \delta(x)\delta(t)$$

which can be solved directly in (k,ω)-space (Huerre and Monkewitz [1990]). If $\lim_{t\to\infty} G(x,t) = 0$ along every ray with x/t constant, then the flow is linearly stable. Otherwise, the limit along the ray $x/t = 0$ determines the type of instability as one of:

- $\lim_{t\to\infty} G(x,t) = 0$ along $x/t = 0 \Rightarrow$ convectively unstable;
- $\lim_{t\to\infty} G(x,t) = \infty$ along $x/t = 0 \Rightarrow$ absolutely unstable.

This is evident from the diagram in Fig. 2.2. This technique may be best demonstrated by an example on the Ginzburg-Landau equation.

2.2.1 Ginzburg-Landau Model

The Ginzburg-Landau equation is considered an accurate prototype for many physical processes, and has been used to explore aspects of these systems on a more fundamental level. In our context, the governing equation is well suited to modelling aspects of hydrodynamic systems and it exhibits many of the eminent features one sees in these situations, including the transient dynamics we are interested in. While not specifically in a hydrodynamic context, Deissler [1987] explored many of the properties of this equation, including the limits for convective and absolute instability. Subsequently, the equation has been used as a demonstrative model in numerous studies, for instance Chomaz et al. [1988] and Cossu and Chomaz [1997], as well as the reviews by Huerre and Monkewitz [1990] and Chomaz [2005].

The Ginzburg-Landau equation models a complex amplitude function $A(x,t)$ satisfying

$$\frac{\partial A}{\partial t} + U\frac{\partial A}{\partial x} = \mu(x)A + (1+ic_d)\frac{\partial^2 A}{\partial x^2} - (1+ic_n)|A|^2 A. \tag{2.1}$$

Linearising Eqn. (2.1) about $A = 0$, the model exposes the local stability concepts through variation of the parameter μ. We now fix μ and examine the linearised Ginzburg-Landau equation,

$$D\left[i\frac{\partial}{\partial t}, -i\frac{\partial}{\partial x}; Re\right]\tilde{A}(x,t) = i\frac{\partial \tilde{A}}{\partial t} + iU\frac{\partial \tilde{A}}{\partial x} - i\mu\tilde{A} - (i-c_d)\frac{\partial^2 \tilde{A}}{\partial x^2} = 0, \tag{2.2}$$

and consider travelling wave solutions of the form $\tilde{A}(x,t) = \rho e^{i(kx-wt)}$. The linearised model has the dispersion relation,

$$\omega = i\mu + kU + k^2(c_d - i). \tag{2.3}$$

Eigenvalues of this linear operator are

$$\lambda = -i\omega = \mu - ikU - k^2(1+ic_d) \tag{2.4}$$

and so it is required that $\mu < 0$ for stability at all wavenumbers, k. To distinguish between the convectively and absolutely unstable states, we are interested in the evolution of the solution in a static frame of reference (along the ray $x/t = 0$) or, equivalently in spectral space, the wave having zero group velocity,

$$\frac{\partial \omega}{\partial k} = 0. \tag{2.5}$$

This gives a critical wavenumber, k_0, and frequency, ω_0, as

$$k_0 = -\frac{U}{2(c_d - i)}$$
$$\omega_0 = i\left(\mu - \frac{U^2}{4(1 + ic_d)}\right)$$

The condition for absolute instability is that $\omega_0 > 0$ and so the solution becomes absolutely unstable at

$$\mu_t = \frac{U^2}{4(1 + c_d^2)}. \tag{2.6}$$

In the interval $0 < \mu < \mu_t$, for $U > 0$, the solution is convectively unstable.

This solution is relatively straightforward if μ is a constant, but does not represent the dynamics of real flows where there are regions of convective and absolute instability. We now consider the case where μ is slowly varying. Chomaz et al. [1988] set $\mu(x) = \mu_0 + \mu' x$ with the restriction that $\mu' < 0$. This model now presents both convective and absolute instability as well as linear stability in different parts of the domain, with disturbances being convected towards the region of stability. In this paper they contrast bifurcations to both local and global modes in the context of the Ginzburg-Landau model and conclude that regions of absolute instability may lead to self-sustained oscillations in the system. This provides a qualitative explanation for the hydrodynamic oscillations seen in some flows. This phenomenon is precisely that reported for flow past a circular cylinder where Pier [2002] reports oscillations associated with the region of absolute

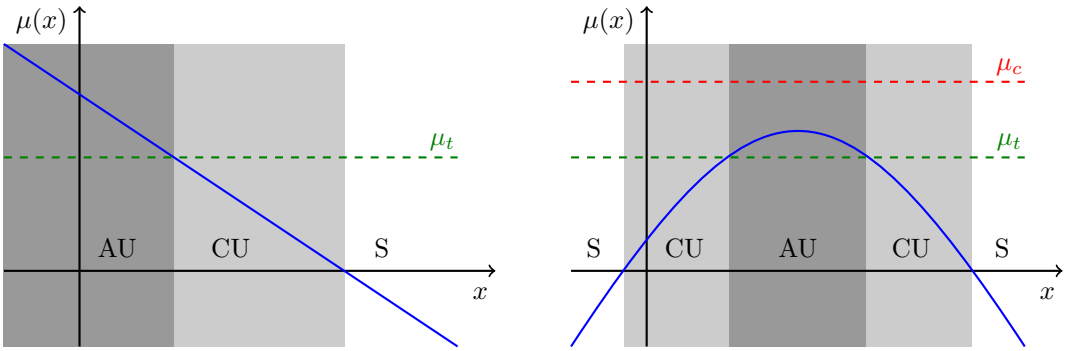

Figure 2.5: Instabilities of the Ginzburg-Landau equation with linear and quadratic coefficient μ. With μ having linear form (left), the equation exhibits a pocket of convective instability (CU) between regions of absolute instability (AU) and local stability (S). With μ having quadratic form (right), it exposes a pocket of absolute instability surrounded by regions of convective instability, representative of real flows.

instability developing behind the cylinder. In Cossu and Chomaz [1997], they use a quadratic form $\mu = \mu_0 + \mu_2 x^2$, with $\mu_2 \leq 0$. This form allows for a pocket of convective instability to exist (see Fig. 2.5), surrounded by local stability, and is a valid model for many shear flows. With μ_2 non-zero, a spatial dependence exists and a global stability problem leads to a critical value $\mu_c > \mu_t$ above which global instability occurs. The strict inequality indicates that a pocket of absolute instability exists prior to global instability, as seen in real flows.

2.3 Global Stability Analysis

In the context of a non-linear dynamical system, global stability is defined as the system's susceptibility to infinitesimal disturbances from an equilibrium point, which in our case is a steady-state solution to the Navier-Stokes Eqns. (1.1), as expressed in the following theorem.

Theorem 2.3.1. *Given a non-linear system* $\dot{\mathbf{u}} = f(\mathbf{u})$*, let* $\mathbf{u}_0$ *be an equilibrium point,*

such that $f(\mathbf{u})$ is continuously differentiable about a neighbourhood of $\mathbf{u}_0$. Let $Df(\mathbf{u}_0)$ be the Jacobian of f evaluated at $\mathbf{u}_0$ and so $\dot{\mathbf{u}} = Df(\mathbf{u}_0)\mathbf{u}$ is the linearisation of $\dot{\mathbf{u}} = f(\mathbf{u})$ about $\mathbf{u}_0$. Then,

- *The point $\mathbf{u}_0$ is asymptotically stable if $Re(\lambda_i) < 0$ for all eigenvalues λ_i of $Df(\mathbf{u}_0)$;*
- *The point $\mathbf{u}_0$ is unstable if $Re(\lambda_i) > 0$ for one or more eigenvalues λ_i of $Df(\mathbf{u}_0)$.*

We now present a brief discussion of the tools for our analysis, namely the linearised Navier-Stokes equations. We define a basic flow, $\boldsymbol{U}$, as a steady solution to the Navier-Stokes equations. The assumption is made that any disturbance is small, so as to justify a linear approximation, and express a solution, $\boldsymbol{u}$, as a linear combination of the steady base-flow, $\boldsymbol{U}$, and an infinitesimal disturbance, $\boldsymbol{u}'$. That is, $\boldsymbol{u} = \boldsymbol{U} + \epsilon\boldsymbol{u}'$. Substitution into Eqns. (1.1) leads straight to the linearised Navier-Stokes equations for the disturbance,

$$\frac{\partial \boldsymbol{u}'}{\partial t} + (\boldsymbol{u}' \cdot \nabla)\boldsymbol{U} + (\boldsymbol{U} \cdot \nabla)\boldsymbol{u}' = -\nabla p + Re^{-1}\nabla^2 \boldsymbol{u}' \tag{2.7a}$$

$$\nabla \cdot \boldsymbol{u}' = 0 \tag{2.7b}$$

The base flow, $\boldsymbol{U}$, is a time-independent solution to Eqns. (1.1) and we have taken the density, ρ, to be unity without loss of generality. Equations (2.7) can be expressed more eloquently as

$$\frac{\partial \boldsymbol{u}'}{\partial t} = \mathcal{L}\boldsymbol{u}' \tag{2.8}$$

with solution $\boldsymbol{u}'(t) = \mathcal{A}(t)\boldsymbol{u}'(0)$ in terms of the state transition operator $\mathcal{A}(t) = \exp \mathcal{L}t$. A solution to Eqns. (2.7) can be considered as a linear combination of the eigenmodes of $\mathcal{L}$, each with associated eigenvalue λ_i. The stability of the flow is then determined by

these eigenvalues, with those having a positive real part being associated with a globally unstable mode. In practice, we compute not the eigenvalues of $\mathcal{L}$, but the eigenvalues, μ_i, of $\mathcal{A}(t)$ for an arbitrary time t. These are then related as

$$\mu_i = \exp \lambda_i t \tag{2.9}$$

and as such the condition of global stability can be formulated as $|\mu_i| < 1, \forall i$.

2.4 A Global Approach to Convective Instability and Transient Growth

So far we have only determined global stability through fully resolved DNS. With the recent increases in computing power there is a great desire to unify the local and global approaches to stability. One aspect of this is achieved through being able to quantify convective instabilities within a global framework. From a global perspective, a convectively unstable flow is one which exposes a region of localised convective instability, while remaining globally stable. In such flows a disturbance passing through this region will experience energy growth as it is transported by the base flow. The growth will continue as the disturbance advects downstream until it enters a region of local stability where it decays.

Mathematically, these effects can be examined in the context of the normality of the linear operator $\mathcal{A}(t)$ and its eigenvectors (Chomaz [2005]). For a given linearly stable flow described by this operator, the set of complex eigenvalues lies within the unit circle. Consequently, the eigenvalues of the linear operator $\mathcal{L}$ lie in the negative half-plane and therefore each associated eigenvector is necessarily decaying. In a normal operator all eigenvectors are pairwise orthogonal, forming a basis of the image, and any given vector within this image is necessarily a linear combination of these eigenvectors and as such

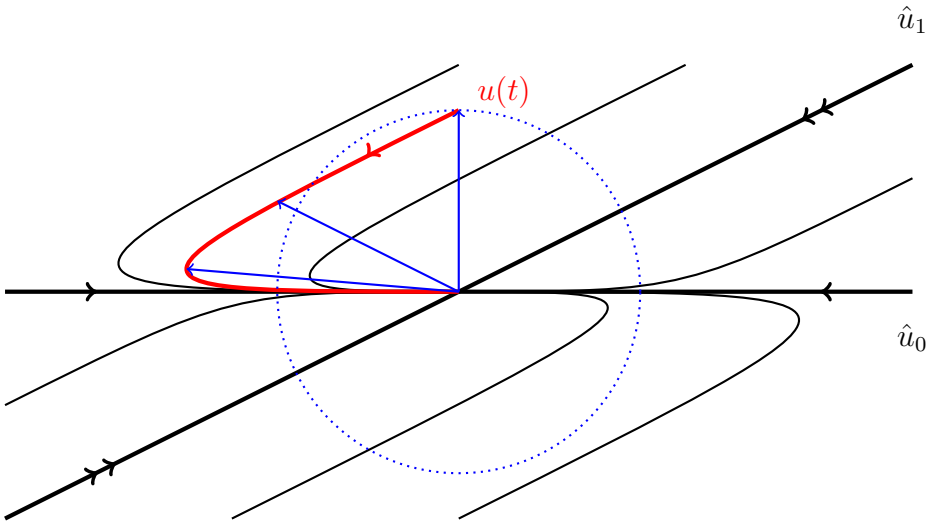

Figure 2.6: Phase plane diagram of transient growth. The growth of the blue vector arises due to the non-orthogonality and largely differing decay rates of the eigenvectors u_0 and u_1. The dotted line shows the initial magnitude of the vector.

must decay. In contrast a non-normal operator has non-orthogonal eigenvectors which, if decaying at substantially different rates, can induce an initial growth of a vector due to their non-orthogonal interaction. This concept is most effectively portrayed through a phase plane diagram such as that in Fig. 2.6. It shows the evolution of the blue vector, indicated by the red line $u(t)$, under the decay of the two eigenvectors u_0 and u_1, where u_1 decays substantially faster than u_0. The linearised Navier-Stokes operator is an example of a non-normal operator and is therefore not self-adjoint.

This interpretation leads to the pseudospectra of the linear operator $\mathcal{L}$, where the extent into which the spectrum protrudes into the right half of the complex plane characterises the magnitude of the potential transient growth. This idea, in the context of fluid flow, is discussed extensively in Trefethen and Embree [2005], but it is outside of the scope of this thesis. Instead we shall concentrate on physical interpretations of the observed phenomena.

There are a number of studies in the existing literature applying these global techniques to a range of separated flows to assess the presence of convective instabilities. In particular, these transient dynamics have been studied in the context of the backward facing step (Blackburn et al. [2008a]), stenosis (Blackburn et al. [2008b]), a curved channel (Marquet et al. [2008b]) and a cavity (Åkervik et al. [2007]). Together they provide a broad insight into the presence of convective instabilities in these types of shear layer flows.

The backward-facing step flow is the ideal model for separated flows, creating a strong shear layer in the simplest of geometries. Blackburn et al. [2008a] found large transient growths occurred even for Reynolds numbers within the linearly stable regime. They find the step-edge is most sensitive to disturbances with growth on the order of 10^5 observable, if the flow is suitably perturbed there. The energy continues to grow as the disturbance passes through the recirculation bubble and peaks at a point beyond the reattachment point. Maximum growth is seen around 25 step-heights beyond reattachment of the primary separation bubble, but an additional recirculation bubble on the upper wall may complicate matters. In this respect the rotational analogue of this geometry - the axisymmetric sudden expansion, considered in Chapter 4 - is a cleaner example with only a single recirculation region.

Stenoses are of fundamental biological relevance and consequently the transient properties of this flow have important medical repercussions. For steady flow in an arterial constriction, Blackburn et al. [2008b] find that energy growth on the order of 10^5 is possible, while for the pulsatile case this could be as high as nine orders of magnitude. More recently, Mao et al. [2009] have shown growths on the order of 10^25 could occur in a more physiologically realistic flow. The resulting wave packet takes the form of a sinuous oscillation of the shear layer, qualitatively different from the roll

structures seen in the backward-facing step (Blackburn et al. [2008a]).

Marquet et al. [2008a] compute the global stability of an S-shaped air-intake. The flow is found to first become unstable to three-dimensional perturbations deforming the recirculation bubble - the same as was reported for the discontinuous backward-facing step (Barkley et al. [2002]). They examine both the leading direct and adjoint modes to explain both the lift-up and convective non-normalities present in the linearised Navier-Stokes operator (see Sec. 2.4.2) and they propose techniques for passive and active flow control. Subsequently, Marquet et al. [2008b] have examined and compared the two types of local dynamics - amplifiers and resonators - in the context of this S-shaped duct and find that given extrinsic noise in the system, the amplifier dynamics dominate.

In much the same way, optimal growth has been computed for a cavity flow which encapsulates the recirculation bubble by Åkervik et al. [2007]. They demonstrate the oscillatory flow can be represented as a summation of global modes and therefore derive a reduced model consisting only of those modes which capture the main dynamics of the flow, a process with value in an industrial setting. Henningson and Åkervik [2008] similarly demonstrate the construction of low-order dynamical models of other flows, including a liquid curtain and Blasius boundary layer.

2.4.1 Calculating Transient Growth

Due to the local nature of convective instabilities they can not be determined immediately from the previous eigenvalue analysis outlined in Sec. 2.3. This only describes the behaviour of global modes in the evolution of the flow. Instead, we introduce an extra parameter to the problem and examine the maximum energy growth at a particular time horizon, τ, of the flow disturbance, $\boldsymbol{u}'$, over all possible initial conditions. This allows us to essentially map out convectively unstable regions of the domain, characterised by

growth in the perturbation energy. Full details of this procedure are available in Barkley et al. [2008], but an overview shall be provided here.

We begin the problem formulation by defining the energy of a disturbance at a time t, expressed in terms of the L_2 norm, as

$$E(t) = \langle \boldsymbol{u}'(t), \boldsymbol{u}'(t) \rangle_{L_2}.$$

We will subsequently assume (and thus drop the notation) that all fields are in L_2. We are then interested in the greatest relative energy gain, at a specified time horizon τ, by any initial condition $\boldsymbol{u}'(0)$,

$$G(\tau) = \max_{\boldsymbol{u}'(0)} \frac{E(\boldsymbol{u}'(\tau))}{E(\boldsymbol{u}'(0))}. \tag{2.10}$$

We can assume without loss of generality that $||\boldsymbol{u}'(0)|| = 1$.

Recall that the evolution operator $\mathcal{A}(t)$ takes $\boldsymbol{u}'(0)$ to a future time $\boldsymbol{u}'(t)$ as $\boldsymbol{u}'(t) = \mathcal{A}(t)\boldsymbol{u}'(0)$. Substitution for E in Eqn. (2.10) gives

$$\begin{aligned} G(\tau) &= \max_{\boldsymbol{u}'(0)} \langle \mathcal{A}(\tau)\boldsymbol{u}'(0), \mathcal{A}(\tau)\boldsymbol{u}'(0) \rangle \\ &= \max_{\boldsymbol{u}'(0)} \langle \boldsymbol{u}'(0), \mathcal{A}^*(\tau)\mathcal{A}(\tau)\boldsymbol{u}'(0) \rangle \\ &= ||\mathcal{A}^*(\tau)\mathcal{A}(\tau)||, \end{aligned} \tag{2.11}$$

where $\mathcal{A}^*(\tau)$ is the adjoint of the operator $\mathcal{A}(\tau)$. The operator $\mathcal{A}^*(\tau)\mathcal{A}(\tau)$ is self-adjoint (and thus normal) and, as a consequence of Eqn. (2.11), $||\mathcal{A}^*(\tau)\mathcal{A}(\tau)|| = \max_i \lambda_i$, the largest eigenvalue of $\mathcal{A}^*(\tau)\mathcal{A}(\tau)$. Since $\mathcal{A}^*(\tau)\mathcal{A}(\tau)$ is self-adjoint, these eigenvalues are necessarily non-negative and real. Instead of finding the eigenvalues of $\mathcal{A}(t)$ (i.e. at any arbitrary time) and looking for eigenvalues of $\mathcal{L}$ with positive real part, we now find the eigenvalues of $\mathcal{A}^*(\tau)\mathcal{A}(\tau)$ of which the largest eigenvalue corresponds to the maximum possible relative growth attainable over the time horizon, τ. Note that $\mathcal{A}^*(\tau)\mathcal{A}(\tau)$ is

computed by first applying $\mathcal{A}(\tau)$, followed by $\mathcal{A}^*(\tau)$. The eigenvector $\boldsymbol{v}_j$ corresponding to λ_j is the disturbance which induces this optimal growth and satisfies

$$\mathcal{A}^*(\tau)\mathcal{A}(\tau)\boldsymbol{v}_j = \lambda_j \boldsymbol{v}_j. \tag{2.12}$$

In terms of the singular value decomposition, $\mathcal{A}(\tau)\boldsymbol{v}_j = \sigma \boldsymbol{u}_j$, we see that

$$\mathcal{A}^*(\tau)\mathcal{A}(\tau)\boldsymbol{v}_j = \sigma^2 \boldsymbol{v}_j \tag{2.13}$$

which is exactly the preceding eigenvalue equation. Geometrically, the singular value decomposition of $\mathcal{A}(\tau)$ maps the basis of functions $\boldsymbol{V}$ to the new basis of functions $\boldsymbol{U}$. As such, the optimal initial conditions $\boldsymbol{v}_j$ are evolved, under the operator $\mathcal{A}(\tau)$, to their point of maximum growth, $\boldsymbol{u}_j$. The $\boldsymbol{u}_j$ can be found simultaneously during the iterative eigenvalue techniques at little extra computational cost.

2.4.2 Adjoint Form of the Linearised Navier-Stokes Equations

We now discuss the derivation of the adjoint operator $\mathcal{A}^*(\tau)$. We express mathematically and subsequently discretise this operator, rather than computing the adjoint of the forward operator discretisation. Proceeding like this ensures all boundary conditions on the adjoint operator are correctly applied and, given an existing implementation of the forward system, does not require knowledge or modification of the specific underlying solver in order to form the adjoint.

Definition (Adjoint operator) The adjoint operator $\mathcal{A}^*(\tau) : L_2 \rightarrow L_2$ of the operator $\mathcal{A}(\tau) : L_2 \rightarrow L_2$, is defined as that which satisfies

$$\langle \mathcal{A}(\tau)\boldsymbol{u}', \boldsymbol{v}' \rangle = \langle \boldsymbol{u}', \mathcal{A}^*(\tau)\boldsymbol{v}' \rangle \quad \forall \boldsymbol{u}', \boldsymbol{v}' \in L_2 \tag{2.14}$$

with $\langle \cdot, \cdot \rangle$ being the inner product

$$\langle \boldsymbol{u}', \boldsymbol{v}' \rangle = \int_\Omega \boldsymbol{u}'\boldsymbol{v}' \mathrm{d}\Omega. \tag{2.15}$$

In our context, we are specifically working in the L_2 space even though this definition generalises to any Hilbert space.

We begin by considering the derivation of the adjoint form of fundamental spatial and temporal derivatives in a space-time domain - namely first- and second-order spatial derivatives and first-order time derivatives. Using integration by parts the adjoint forms of these operators are computed as

$$\frac{\partial}{\partial x_i}: \quad \int_T \int_\Omega \frac{\partial u_i}{\partial x_i} v_j \mathrm{d}\boldsymbol{x}\mathrm{d}t = \int_T [u_i v_j]_\Omega \mathrm{d}t - \int_T \int_\Omega u_i \frac{\partial v_j}{\partial x_i} \mathrm{d}\boldsymbol{x}\mathrm{d}t, \tag{2.16a}$$

$$\frac{\partial}{\partial t}: \quad \int_T \int_\Omega \frac{\partial u_i}{\partial t} v_j \mathrm{d}\boldsymbol{x}\mathrm{d}t = \int_\Omega [u_i v_j]_T \mathrm{d}\Omega - \int_T \int_\Omega u_i \frac{\partial v_j}{\partial t} \mathrm{d}\boldsymbol{x}\mathrm{d}t, \tag{2.16b}$$

$$\begin{aligned} \frac{\partial^2}{\partial x_i^2}: \quad & \int_T \int_\Omega \frac{\partial^2 u_i}{\partial x_i^2} v_j \mathrm{d}\boldsymbol{x}\mathrm{d}t \\ & = \int_T \left[\frac{\partial u_i}{\partial x_i} v_j\right]_\Omega \mathrm{d}t - \int_T \left[\frac{\partial u_i}{\partial x_i}\frac{\partial v_j}{\partial x_i}\right]_\Omega \mathrm{d}t + \int_T \int_\Omega u_i \frac{\partial^2 v_j}{\partial x_i^2} \mathrm{d}\boldsymbol{x}\mathrm{d}t. \end{aligned} \tag{2.16c}$$

In practice the boundary terms introduced by the integration by parts will evaluate to zero since, for the moment, we assume that $\boldsymbol{u}$ and $\boldsymbol{v}$ have compact support in the space-time domain. These boundary conditions will be discussed in more detail later in this section.

We now consider Eqns. (2.7) and the evolution of both the velocity components, $\boldsymbol{u}'$, and the pressure field p', in time. To simplify notation we combine these components into a single vector, $\boldsymbol{q}'$, defined as

$$\boldsymbol{q}' = \begin{bmatrix} \boldsymbol{u}' \\ p' \end{bmatrix}. \tag{2.17}$$

Equations (2.7) can then be expressed using the single operator

$$\mathcal{H} = \left[\begin{array}{c|c} -\partial_t - \boldsymbol{D}\boldsymbol{N} + Re^{-1}\nabla^2 & -\nabla \\ \hline \nabla\cdot & 0 \end{array}\right] \tag{2.18}$$

as $\mathcal{H}\boldsymbol{q}' = 0$, where $\boldsymbol{DN} = (\boldsymbol{U} \cdot \nabla) + (\nabla \boldsymbol{U})$. We can rewrite the above operator in terms of its component derivatives. Let the 3×3-matrices A, B, C and D, and their adjoint forms, be defined as:

$$A_{ij} = -A^*_{ij} = -\delta_{ij} \frac{\partial}{\partial t} \tag{2.19a}$$

$$B_{ij} = -B^*_{ij} = \delta_{ij} \sum_i \boldsymbol{U}_i \frac{\partial}{\partial x_i} \tag{2.19b}$$

$$C_{ij} = C^*_{ji} = \frac{\partial \boldsymbol{U}_i}{\partial x_j} \tag{2.19c}$$

$$D_{ij} = D^*_{ij} = \delta_{ij} Re^{-1} \frac{\partial^2}{\partial x_i^2}. \tag{2.19d}$$

These matrices correspond to the temporal (A), linearised advection (B and C), and viscous diffusive (D) operators. Note that only C contains off-diagonal entries. The linearised advection terms are at the centre of the non-normality of the operator. The C matrix, with its off-diagonal elements, generates streamwise velocity perturbations due to the transport of base flow momentum by cross-stream velocity terms (Schmid and Henningson [2001]). This lift-up non-normality, first explored by Butler and Farrell [1992], arises due to the adjoint operator transposing the $\partial_y U$ from the streamwise component to the cross-stream component. In contrast, the convective non-normality, a feature only present in open flows, arises due to the change in sign of $(\boldsymbol{U} \cdot \nabla)$. This has a consequence of spatially separating the direct and adjoint modes, as observed by Marquet et al. [2008a] for the S-shaped duct.

Our linearised Navier-Stokes equations can then be written as

$$\left[\begin{array}{c|c} A + B + C + D & -\nabla \\ \hline \nabla\cdot & 0 \end{array}\right]. \tag{2.20}$$

Following on from Eqns. (2.19) and Eqns. (2.16a), we can express the adjoint operator $\mathcal{H}^*$ (that is, the trans-conjugate of $\mathcal{H}$) as

$$\mathcal{H}^* = \left[\begin{array}{c|c} \partial_t - \boldsymbol{DN}^*(\boldsymbol{u}') + Re^{-1}\nabla^2 & -\nabla \\ \hline \nabla\cdot & 0 \end{array}\right] \tag{2.21}$$

as $\mathcal{H}^*\boldsymbol{q}'^* = 0$, where $\boldsymbol{DN}^* = -(\boldsymbol{U}\cdot\nabla) + (\nabla\boldsymbol{U})^\top$. The sign of the pressure term and incompressibility condition are unchanged due to the effective sign cancellation of the matrix transpose and integration by parts. However, the sign of the adjoint pressure term is essentially arbitrarily defined, given the equations should be equally valid with the divergence condition negated.

Boundary conditions

Up to now we have considered $\boldsymbol{u}'$ to have compact support which equates to zero Dirichlet boundary conditions on all domain boundaries, which includes initial conditions to both the forward and adjoint systems. Of course, this will only present the trivial solution and so we must allow for non-zero initial conditions while still satisfying the restrictions imposed by the forward and adjoint systems. Specifically, Eqn. (2.16b) imposes the restriction that

$$\int_\Omega \left[\boldsymbol{u}'\cdot\boldsymbol{u}'^*\right]_T \mathrm{d}\Omega = 0 \tag{2.22}$$

which in terms of the inner product $(\cdot,\cdot)$ requires

$$\langle \boldsymbol{u}'(\tau), \boldsymbol{u}'^*(\tau)\rangle = \langle \boldsymbol{u}'(0), \boldsymbol{u}'^*(0)\rangle. \tag{2.23}$$

Consequently, we have that

$$\langle \mathcal{A}(\tau)\boldsymbol{u}'(0), \boldsymbol{u}^*(\tau)\rangle = \langle \boldsymbol{u}'(0), \mathcal{A}^*(\tau)\boldsymbol{u}^*(\tau)\rangle \tag{2.24}$$

as defined in Eqn. (2.14).

2.4.3 Cylindrical Coordinates

We now consider the Navier-Stokes equations in cylindrical coordinates for conducting transient growth analysis in geometries that lend themselves to this system. One typical example is a sudden expansion in a circular pipe (see Chapter 4) and the gradually expanding pipe (see Chapter 6). Let the velocity be defined as

$$\boldsymbol{u} = u_x \boldsymbol{e}_x + u_r \boldsymbol{e}_r + u_\theta \boldsymbol{e}_\theta. \tag{2.25}$$

where $\boldsymbol{e}_x$, $\boldsymbol{e}_r$ and $\boldsymbol{e}_\theta$ denote the unit vectors in the x, r and θ directions respectively. For a scalar field f, derivative operators in cylindrical coordinates take the form:

$$\nabla f = \left(\partial_x f, \quad \partial_r f, \quad \frac{1}{r} \partial_\theta f \right), \tag{2.26a}$$

$$\nabla \cdot f = \partial_x f + \frac{1}{r} \partial_r (r f) + \frac{1}{r} \partial_\theta f, \tag{2.26b}$$

$$\nabla^2 f = \partial_{xx} f + \frac{1}{r} \partial_r (r \partial_r f) + \frac{1}{r^2} \partial_{\theta\theta} f. \tag{2.26c}$$

Additionally, extra terms arise from differentiation of the unit vectors with respect to the azimuthal coordinate:

$$\partial_\theta \boldsymbol{e}_r = \boldsymbol{e}_\theta, \tag{2.27a}$$

$$\partial_\theta \boldsymbol{e}_\theta = -\boldsymbol{e}_r. \tag{2.27b}$$

This will consequently introduce extra terms in the Navier-Stokes equations

$$\partial_t \boldsymbol{u} + \mathcal{N}(\mathbf{u}) = -\nabla p + Re^{-1} \mathcal{D}(\boldsymbol{u})$$

$$\mathcal{N}(\boldsymbol{u}) = (\boldsymbol{u} \cdot \nabla) \boldsymbol{u}$$

$$\mathcal{D}(\boldsymbol{u}) = \nabla^2 \boldsymbol{u}$$

with incompressibility constraint

$$\nabla \cdot \boldsymbol{u} = \partial_x u_x + \frac{1}{r} \partial_r (r u_r) + \frac{1}{r} \partial_\theta u_\theta - \frac{u_\theta}{r} = 0.$$

Specifically, in component form the non-linear operator $\boldsymbol{N}(\boldsymbol{u})$ takes the form

$$\begin{aligned}
\mathcal{N}(\boldsymbol{u})_x &= u_x\partial_x u_x + u_r\partial_r u_x + \frac{1}{r}u_\theta\partial_\theta u_x \\
\mathcal{N}(\boldsymbol{u})_r &= u_x\partial_x u_r + u_r\partial_r u_r + \frac{u_\theta}{r}(\partial_\theta u_r - u_\theta) \\
\mathcal{N}(\boldsymbol{u})_\theta &= u_x\partial_x u_\theta + u_r\partial_r u_\theta + \frac{u_\theta}{r}(\partial_\theta u_\theta + u_r)
\end{aligned}$$

where the additional term $-u_\theta^2/r$ arises from Eqn. (2.27b) and similarly $u_\theta u_r/r$ arises from Eqn. (2.27a). The $\mathcal{D}(\boldsymbol{u})$ operator takes the form

$$\begin{aligned}
\mathcal{D}(\boldsymbol{u})_x &= \partial_{xx}u_x + \frac{1}{r}\partial_r r\partial_r u_x + \frac{1}{r^2}\partial_{\theta\theta}u_x \\
\mathcal{D}(\boldsymbol{u})_r &= \partial_{rr}u_r + \frac{1}{r}\partial_r r\partial_r u_r + \frac{1}{r^2}\partial_{\theta\theta}u_r - \frac{u_\theta}{r^2} - \frac{2}{r^2}\partial_\theta u_\theta \\
\mathcal{D}(\boldsymbol{u})_\theta &= \partial_{xx}u_\theta + \frac{1}{r}\partial_r r\partial_r u_\theta + \frac{1}{r^2}\partial_{\theta\theta}u_\theta - \frac{u_\theta}{r^2} + \frac{2}{r^2}\partial_\theta u_r
\end{aligned}$$

again with the additional terms introduced from Eqn. (2.27). The equations are typically multiplied by r to remove all but a $1/r$ singularity on the diffusive term. Boundary conditions for the cylindrical case are detailed in Blackburn and Sherwin [2004].

2.4.4 Span-wise Wavenumber Dependence

In geometries with a homogeneous third direction, the linear solution $\boldsymbol{u}'$ may be decomposed into a Fourier series

$$\boldsymbol{u}'(x,y,z) = \hat{\boldsymbol{u}}(x,y)e^{i\beta z} + cc.$$

The linear nature of the solution results in a decoupling of these waves, allowing the solutions for individual wavenumbers, β, to be computed separately in a two-dimensional

context. Eigenmodes of $\mathcal{A}^*(\tau)\mathcal{A}(\tau)$ then have the trigonometric form

$$\tilde{u}_x(x,y,z) = \hat{u}_x(x,y)\cos(\beta z)$$
$$\tilde{u}_y(x,y,z) = \hat{u}_y(x,y)\cos(\beta z)$$
$$\tilde{u}_z(x,y,z) = \hat{u}_z(x,y)\sin(\beta z)$$
$$\tilde{p}(x,y,z) = \hat{p}(x,y)\cos(\beta z)$$

The azimuthal symmetry in cylindrical coordinates results in a Fourier decomposition with azimuthal modes. In this case we consider β discrete, rather than continuous and have $\beta z = m\theta$ for $m \in \mathbb{N}$.

We will use the techniques covered in this chapter for solving the problems discussed in Chapters 4, 5 and 6. In the next chapter we will review the numerical methods used for solving the Navier-Stokes equations.

Chapter 3

Numerical Techniques

In this chapter we discuss the formulation of numerical methods to solve the problems outlined in the previous chapter. These methods include the discretisation of the Navier-Stokes equations as well as the outer level eigenvalue algorithms required for the linear analysis. This chapter additionally includes details of two modifications made to the existing code base: a *copy boundary condition* (Sec. 3.4); and an eigenvalue deflation algorithm (Sec. 3.6.1). However, we will first examine the spectral element method which underpins the direct numerical simulation code (Blackburn and Sherwin [2004]) used throughout this thesis.

3.1 Spectral Element Formulation in One-Dimension

The spectral element method, first pioneered by Patera [1983], draws on the geometric flexibility of a piecewise linear finite element scheme, and the high order accuracy and exponential convergence properties of spectral techniques. In analogy to a finite element method, the domain is broken down into elemental regions on which a polynomial basis is used to represent the solution. This synergy gives the flexibility to refine both globally,

by increasing polynomial order (p-refinement), or locally, by refining those elemental regions where greater resolution in the solution is required (h-refinement). We give a description of the technique in the one-dimensional case, before discussing how the method extends to two-dimensions where it is used to solve the fluid problems included in this thesis.

3.1.1 Domains and Elements

Consider a one-dimensional domain Ω, decomposed into a set of elemental regions $\Omega_e = [x_e, x_{e+1}]$, such that

$$\Omega = \bigcup_e \Omega_e$$

and for the corresponding open intervals $\tilde{\Omega}_e = (x_e, x_{e+1})$,

$$\tilde{\Omega}_e \cap \tilde{\Omega}_f = \emptyset \qquad \forall e \neq f.$$

The dependent variable of our PDE is discretised at fixed quadrature points in the element and represented in terms of an orthogonal expansion basis. With this formulation the necessary numerical integration and differentiation can be performed to solve a given problem.

To express a function in terms of the orthogonal basis efficiently on any arbitrarily-shaped element, each one is mapped from a *standard element*, $\overline{\Omega}$, on which the polynomial basis is defined, and is the foundation on which we define our integration and differentiation. This is, in the simplest case, a straightforward linear mapping, although more complex functions may account for curved elemental surfaces. We first consider how to represent a function on the one-dimensional standard element.

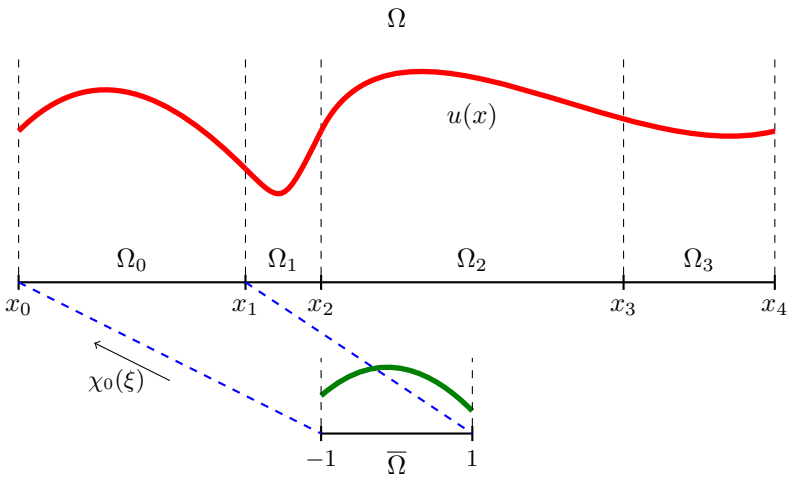

Figure 3.1: Diagram of a one-dimensional domain decomposition. A continuous function $u(x)$ on the domain Ω is approximated on each element separately through a polynomial expansion basis on the standard element $\overline{\Omega} = [-1, 1]$. The mapping χ_e maps the standard element onto the element Ω_e.

Definition The one-dimensional standard element is defined as

$$\overline{\Omega} = [-1, 1].$$

We can map the standard element onto an arbitrary element by defining a linear mapping $\chi_e : \bar{\Omega} \rightarrow \Omega_e$ such that

$$x = \chi_e(\xi) = \frac{1-\xi}{2} x_e + \frac{1+\xi}{2} x_{e+1} \qquad \xi \in \bar{\Omega}.$$

This mapping has an analytical inverse

$$\xi = \chi_e^{-1}(x) = 2\frac{x - x_e}{x_{e+1} - x_e} - 1 \qquad x \in \Omega_e.$$

Using this map we can now translate a function, defined on $\overline{\Omega}$, to any element and thus provide the ability to extend numerical operations on the standard element onto an element of any size and orientation. This is summarised in the diagram in Fig. 3.1.

The standard element is discretised at Q points, also termed quadrature points due to their subsequent use in numerical integration. Furthermore we construct a basis of P polynomials with which to represent a function on the standard element.

Definition The space of all polynomials of degree n or less on the standard element $\bar{\Omega}$ shall be denoted by $\mathcal{P}_n(\bar{\Omega})$.

Definition (Local basis functions) A continuous function on the standard element is approximated by a set of P polynomial basis functions, denoted as $\{\phi_p\}$, $p = 0, \ldots, P-1$, $\phi_p \in \mathcal{P}_{P-1}(\bar{\Omega})$. Using the above mapping, $\chi_e(\xi)$, we denote the basis on each arbitrary element, e, as

$$\phi_p^e(x) = \phi_p(\chi_e^{-1}(x)).$$

We use ϕ to denote general basis functions where the context is independent of the exact choice of function, but will shortly define symbols to represent specific classes of bases for which the type is relevant.

Definition (Global basis function) For the pth elemental basis function on element e, denoted locally as $\phi_p^e(x)$ with $x \in \Omega_e$, the corresponding basis function on Ω is defined as

$$\Phi_{k=k(p,e)}(x) = \begin{cases} \phi_p^e(x), & \text{if } x \in \Omega_e, \\ 0, & \text{otherwise.} \end{cases}$$

The choice of $\phi_p^e(x)$ is critical in finding a balance between the quality of the numerical convergence properties and the computational efficiency of the scheme - the resulting mass matrix should be numerically efficient to implement in terms of minimising its bandwidth. Some bases will expose a structure which can be exploited to significantly

reduce computation time for matrix-matrix and matrix-vector operations. However, these benefits must be weighed against the ability of the basis to accurately approximate the solution and the computational complexity of generating the matrix system. The basis functions we will consider are chosen from one of two polynomial categories which, as shall be discussed next, exhibit different numerical characteristics.

Unlike a trigonometric bases, polynomial bases allow for non-periodic boundaries on individual elements - a property which is essential for domain decomposition. The categories of polynomial bases we consider are:

- *Nodal* - a basis of interpolation polynomials through a fixed set of zeros;
- *Modal* - a hierarchical basis of polynomials.

Nodal bases are typically more straightforward to implement due to their correlation with the physical domain - the spectral coefficients approximate the solution at the interpolation points. However, they can produce a more structured and computationally efficient matrix system (reduced bandwidth) which will provide better performance and potentially more scope for parallelisation. The modal coupling can be circumvented using boundary-interior decomposition to separate off those boundary modes liable to create dependencies.

Definition (Nodal expansion basis) Given a set of Q points $\Gamma = \{\xi_0, \ldots, \xi_{Q-1}\}$ on the standard element, a nodal expansion basis, $\phi_p = h_p$, is a set of Q polynomials of order $P = Q - 1$, such that

$$\mathcal{N}_P = \{h_p(\xi) \in \mathcal{P}_P(\bar{\Omega}) | h_p(\xi_q) = \delta_{pq}, p = 0, 1, \ldots, Q-1\}$$

Locally, they shall be denoted as $h_p^e(x)$, and globally as $H_k(x)$.

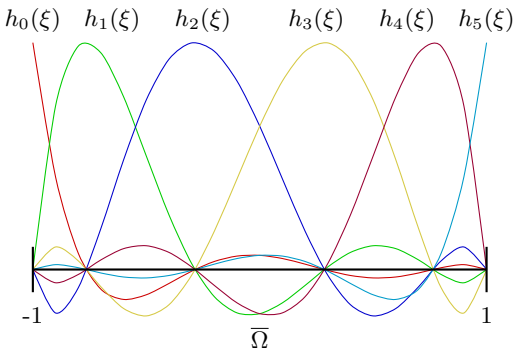

Figure 3.2: Basis of Lagrange interpolation polynomials. They are defined through the zeros of Legendre polynomials and the points -1 and 1. Here $Q = 6$ and each of the six polynomials are of order $P = 5$.

Note that while the discretisation matches the solution at the nodes, that is $u(\xi_q) = \hat{u}_q$, the PDE is approximated at these points. Typically a nodal expansion basis is generated using Lagrange interpolation through the nodal points. This is defined as

$$\phi_p(\xi) = h_p(\xi) = \frac{\prod_{q=0,q\neq p}^{Q}(\xi - \xi_q)}{\prod_{q=0,q\neq p}^{Q}(\xi_p - \xi_q)}.$$

A graphical representation of the Lagrange polynomial basis is given in Fig. 3.2

While any choice of interior nodal points could be used, the zeros of a class of Jacobi polynomials (see App. A.1) leads to a highly optimal implementation. It was first noticed by Gauss that integration using specific choices of n points could yield an exact result for polynomials of order $2n - 1$ or less. This idea forms the basis of Gaussian quadrature rules. Specifically, the end points of the interval together with zeros of Legendre polynomials (see App. A.3) are chosen for the quadrature points in our code base, which are denoted as the Gauss-Lobatto-Legendre points. Legendre polynomials are a subset of the Jacobi polynomial family with $\alpha = \beta = 1$.

The pth nodal Lagrange interpolation polynomial basis function, $h_p(x)$, through

the nodes $\xi_{i,Q}^{\alpha,\beta}$ (zeros of Jacobi polynomial $P_{Q-1}^{\alpha,\beta}$) can then be expressed as,

$$h_p(\xi) = \begin{cases} 1, & \text{if } \xi = \xi_p, \\ \frac{(\xi^2-1)\left[P_{Q-1}^{\alpha,\beta}(\xi)\right]'}{(Q-1)(Q+\alpha+\beta)P_{Q-1}^{\alpha,\beta}(\xi_j)(\xi-\xi_j)}, & \text{otherwise.} \end{cases}$$

In the code used throughout this thesis, the choice of polynomial basis is the Lagrange interpolation polynomials through the Gauss-Lobatto-Legendre points.

Definition (Modal expansion basis) The modal basis $\phi_p(x) = \psi_p(x)$ is a set of P polynomial functions such that $\psi_p(x) \in \mathcal{P}_p(\bar{\Omega})$, that is,

$$\mathcal{B}_P = \left\{\psi_p(x) \in \mathcal{P}_p(\bar{\Omega}) | 0 \leq p \leq P-1\right\},$$

and $\mathcal{B}_P \subset \mathcal{B}_{P+1}$.

Consequently, modal bases can be easily extended through the addition of a single mode to the basis. This would make them particularly effective for implementing p-type refinement since any pre-computed values (such as Gaussian integration weights) need not be recomputed. Only those values for the additional mode need be computed.

3.1.2 Method of Weighted Residuals

The method of weighted residuals is formulated around the discretisation error, or *residual*, in u^δ of a continuous function u given a set of basis functions $\{\phi_p\}$. By applying different *test functions* with the Legendre inner product, different projection operations can be applied. Initially, we restrict ourselves to the standard element.

Definition The Legendre inner product of two functions f and g is defined as

$$(f, g) = \int_{-1}^{1} f(x)g(x)\mathrm{d}x.$$

Definition For a continuous solution $u(\xi)$ on the domain $\bar{\Omega}$, the finite element approximation $u^{\delta}(\xi)$ in terms of elemental modes is expressed as

$$u^{\delta}(\xi) = \sum_{p=0}^{P} \hat{u}_p \phi_p(x). \tag{3.1}$$

We consider the residual of our approximation in relation to the true solution,

$$R(\xi) = u^{\delta}(\xi) - u(\xi). \tag{3.2}$$

Given the set of test functions, v_j, the spectral coefficients, $\hat{u}_k$, are computed such that the Legendre inner product of the residual with the test functions is zero. That is,

$$(v_j(\xi), R(\xi)) = 0.$$

Note that the test functions are defined to be zero on all Dirichlet boundaries. Taking the inner product of Eqn. (3.2) gives

$$\left(v_j(\xi), \sum_p \hat{u}_p \phi_p(\xi) \right) = \left(v_j(\xi), u(\xi) \right).$$

The choice of test functions v_j will result in different types of projection. For the Galerkin projection, the set of test functions are chosen to be the same set of basis functions, that is, $\{v_j\} = \{\phi_j\}$. Therefore, we have that

$$\left(\phi_j(\xi), \sum_p \hat{u}_p \phi_p(\xi) \right) = \left(\phi_j(\xi), u(\xi) \right). \tag{3.3}$$

Hence, the weak Galerkin form of a PDE is found by forming the inner product with the test functions v_j, thus for $\mathbb{F}u = 0$ we require that

$$(v, \mathbb{F}u) = 0$$

3.1.3 Numerical Integration

Numerical integration, in our case called Gaussian quadrature, is the technique used to compute a numerical approximation to the integral of a discretised function on a domain. It is a weighted sum of function values at a set of fixed quadrature points. The integrand is expressed in terms of Lagrange polynomials in the same way as for a nodal basis, and is given by

$$u(\xi) = \sum_q u(\xi_q) h_q(\xi) + \epsilon(u).$$

Consequently, we have

$$\int_{-1}^{1} u(\xi) \mathrm{d}\xi = \sum_q u(\xi_q) w_q, \tag{3.4a}$$

$$w_q = \int_{-1}^{1} h_q(\xi) \mathrm{d}\xi. \tag{3.4b}$$

The quadrature weights w_q are precomputed for the standard element. This form of integration is particularly accurate for carefully chosen quadrature points, ξ_q, at the roots of Jacobi polynomials. For the exact values of ξ_q and w_q at such zeros see App. A.3.1.

To extend this to arbitrary elements we use a change of variable to account for the mapping $\chi_e(\xi)$. To compute the integral of a function $u(x)$ on the element $e = [a, b]$ we evaluate

$$\begin{aligned}
\int_a^b u(x) dx &= \int_a^b \sum_q \hat{u}_q h_q^e(x) \mathrm{d}x, \\
&= \sum_q \hat{u}_q \int_a^b h_q^e(x) \mathrm{d}x, \\
&= \sum_q \hat{u}_q \int_{-1}^{1} h_q(\chi_e^{-1}(x)) \frac{\mathrm{d}\xi}{\mathrm{d}x} \mathrm{d}\xi, \\
&= \frac{b-a}{2} \sum_q \hat{u}_q w_q,
\end{aligned}$$

where the w_q are as defined in Eqn. (3.4b). The coefficients $(b-a)/2$ are also precomputed for each element e.

3.1.4 Numerical Differentiation

Given the approximation of $u(\xi)$ in terms of the expansion basis ϕ_p from Eqn. (3.1), the derivative of $u(\xi)$ at a given node ξ_q is evaluated as

$$\left.\frac{\mathrm{d}u(\xi)}{\mathrm{d}\xi}\right|_{\xi=\xi_q} = \sum_p \hat{u}_p \left.\frac{\mathrm{d}\phi_p}{\mathrm{d}\xi}\right|_{\xi_q},$$

which requires knowledge of $\frac{d\phi_p}{d\xi}$. This is known as collocation differentiation since it is performed in physical space. Differentiation on an arbitrary element is achieved using the chain rule. If we wish to evaluate the derivative of a function $u(x)$ with respect to x, at the point z in element e, it follows that

$$\begin{aligned}
\left.\frac{\mathrm{d}u}{\mathrm{d}x}\right|_{x=z} &= \frac{\mathrm{d}}{\mathrm{d}x}\left[\sum_p \hat{u}_p \phi_p^e(x)\right]\Bigg|_{x=z} \\
&= \sum_p \hat{u}_p \left.\frac{\mathrm{d}\phi_p^e(x)}{\mathrm{d}x}\right|_{x=z} \\
&= \sum_p \hat{u}_p \left.\frac{\mathrm{d}\phi_p(\xi)}{\mathrm{d}\xi}\right|_{\xi=[\chi^e]^{-1}(z)} \frac{\mathrm{d}\xi}{\mathrm{d}x} \\
&= \frac{2}{b-a}\sum_p \hat{u}_p \left.\frac{\mathrm{d}\phi_p(\xi)}{\mathrm{d}\xi}\right|_{\xi=[\chi^e]^{-1}(z)}.
\end{aligned}$$

3.2 Implementation in One Dimension

3.2.1 Spectral Transforms

After establishing the form of our spectral expansion and a technique for performing numerical integration, we now turn our attention to the process of transforming between *physical space* and *spectral space* and ultimately to discretise linear operators. The final

description will be in a matrix form which will be directly applicable to computational implementations. First we define several important fundamental matrices on the standard element. Recall that a function on the standard element is discretised using Q quadrature points and approximated by a basis of P polynomials in spectral space.

Definition (Basis Matrix $\boldsymbol{B}$) The columns of the $P \times Q$ matrix $\boldsymbol{B}$ contain the evaluation of the P basis functions, ϕ_j, at the Q quadrature points, ξ_i. That is, $\boldsymbol{B}_{ij} = \phi_j(\xi_i)$, and it takes the form

$$\boldsymbol{B} = \begin{bmatrix} \phi_0(\xi_0) & \cdots & \phi_{P-1}(\xi_0) \\ \vdots & & \vdots \\ \phi_0(\xi_{Q-1}) & \cdots & \phi_{P-1}(\xi_{Q-1}) \end{bmatrix}.$$

Note In the case of the nodal Lagrange interpolated polynomial basis, $Q = P + 1$ for convenience.

Definition (Weights Matrix $\boldsymbol{W}$) This is a diagonal matrix containing the quadrature weights, w_k, from Eqn. (3.4a) with elements defined as $\mathbf{W}_{ij} = w_i \delta_{ij}$. Therefore,

$$\boldsymbol{W} = \begin{bmatrix} w_0 & & 0 \\ & \ddots & \\ 0 & & w_{Q-1} \end{bmatrix}.$$

With these two operators, we can perform numerical integration and thus consider how to perform forward and backward transforms between physical and spectral space on the standard element.

Forward Transform

To perform the transform from physical space into spectral space the coefficients $\hat{u}_p$ need to be computed.

We continue our Galerkin formulation from Eqn. (3.3). Considering the RHS, we apply the method of numerical integration defined in Eqn. (3.4a) to give

$$\begin{aligned}(\phi_j(\xi), u(\xi)) &= \int_{\bar{\Omega}} \phi_j(\xi) \cdot u(\xi) \mathrm{d}x \\ &= \sum_q \phi_j(\xi_q) \cdot u(\xi_q) \cdot w_q \\ &= \boldsymbol{\phi_j}^\top \boldsymbol{W} \boldsymbol{u} \\ &= \left(\boldsymbol{B}^\top \boldsymbol{W} \boldsymbol{u}\right)[j]\end{aligned}$$

where $\mathbf{u}$ is the vector of $u(\xi)$ evaluated at the quadrature points and the $[j]$ denotes the jth column of the resulting matrix. For the LHS:

$$\begin{aligned}\left(\phi_j(\xi), \sum_p \hat{u}_p \phi_p(\xi)\right) &= \sum_p \hat{u}_p (\phi_j(\xi), \phi_p(\xi)) \\ &= (\boldsymbol{B}^\top \boldsymbol{W} \boldsymbol{B} \hat{\boldsymbol{u}})[j].\end{aligned}$$

Combining these, the coefficients, $\hat{\mathbf{u}}$, can be found by solving the matrix system

$$\boldsymbol{B}^\top \boldsymbol{W} \boldsymbol{B} \hat{\boldsymbol{u}} = \boldsymbol{B}^\top \boldsymbol{W} \boldsymbol{u} = \boldsymbol{f}.$$

Definition (Mass Matrix $\boldsymbol{M}$) The mass matrix $\boldsymbol{M}$ is defined as

$$\boldsymbol{M} = \boldsymbol{B}^\top \boldsymbol{W} \boldsymbol{B}.$$

In general $\boldsymbol{B}$ is not square, whereas $\boldsymbol{M}$ is positive definite and thus non-singular. The optimal structure for the mass matrix is diagonal. However, this needs to be weighed up against the computational cost of constructing the matrix. Once a basis function is defined and numerical integration has been implemented on the standard element, creating the mass matrix and $\boldsymbol{f}$ is relatively straightforward.

Backward Transform

From Eqn. (3.1), transforming the spectral mode coefficients back to physical space involves only the trivial operation

$$\boldsymbol{u} = \boldsymbol{B}\hat{\boldsymbol{u}}.$$

3.2.2 Discrete Derivative Operators

The techniques of numerical integration and differentiation in spectral space can be combined to formulate a set of differential operators which will be used in the time stepping of a particular PDE. The fundamental derivative matrix is defined, based on the method of numerical differentiation described in the previous section. Translation of the derivative matrix onto an arbitrary element is achieved through a diagonal coefficient matrix used to apply the chain rule.

Definition (Differentiation Matrix $\boldsymbol{D}$) The square $Q \times Q$ differentiation matrix $\boldsymbol{D}$ is defined as

$$\boldsymbol{D}_{qr} = \left.\frac{\mathrm{d}h_r(\xi)}{\mathrm{d}\xi}\right|_{\xi_q},$$

where $h_r(\xi)$ are the Q Lagrange interpolation polynomials through the Q quadrature points ξ_q.

This is the fundamental matrix used to build discretised differential operators on the standard element. To differentiate on any arbitrary element, we need to apply the chain rule using a second matrix of coefficients.

Definition (Diagonal Coefficient Matrix $\boldsymbol{\Lambda}(f(\xi))$) This matrix, denoted by $\boldsymbol{\Lambda}$ is defined as

$$\boldsymbol{\Lambda}_{qr} = f(\xi_q)\delta_{qr}.$$

$\boldsymbol{D}^e$ can now be defined for an arbitrary element as

$$\boldsymbol{D}^e = \boldsymbol{\Lambda}\left(\frac{\mathrm{d}\xi}{\mathrm{d}x}\right)\boldsymbol{D}.$$

We now have the necessary tools to define the familiar linear differential operators required to solve PDEs on the standard element.

Weak advection operator: $\boldsymbol{L^{(1)}} = \nabla$

This is represented in discrete form on the standard element as

$$\boldsymbol{L}^{(1)} = \boldsymbol{B}^\top \boldsymbol{W}\boldsymbol{D}\boldsymbol{B}.$$

This can be derived by differentiating Eqn. (3.1) and applying the Galerkin formulation to give

$$\begin{aligned}\left(\phi_j(\xi), \frac{\partial}{\partial\xi}\sum_p \hat{u}_p\phi_p(\xi)\right) &= \sum_p \hat{u}_p\left(\phi_j(\xi), \frac{\partial}{\partial\xi}\phi_p(\xi)\right)\\ &= (\boldsymbol{B}^\top\boldsymbol{W}\boldsymbol{D}\boldsymbol{B}\hat{\boldsymbol{u}})[j]\end{aligned}$$

The operator for a general element can be derived simply through the use of the linear map $x = \chi(\xi)$ and the chain rule in the derivative term.

Weak Laplacian operator: $\boldsymbol{L^{(2)}} = \nabla^2$

Consider the Laplacian operator ∇^2. In applying the Galerkin construction to this operator, the inner product $(v, \nabla^2 u)$ is transformed into $(\nabla v, \nabla u)$ using the *Divergence theorem*. This allows us to simply apply the previous technique twice to obtain the numerical form of the Laplacian. The Divergence Theorem equates the outward flux of a vector field through a surface with the integral of the divergence within, and is quoted below.

Theorem 3.2.1. *(Divergence Theorem) Let V be a compact subset of $\mathbb{R}^n$ with piecewise continuous boundary. If F is a continuously differentiable vector field defined on a neighbourhood of V, then*

$$\int_V (\nabla \cdot \boldsymbol{F}) dV = \int_{\partial V} \boldsymbol{F} \cdot \boldsymbol{n} dS.$$

Using the vector identities, the above expression can be formulated in the following form.

$$\int_V \nabla f \cdot \nabla g dV + \int_V g(\nabla \cdot \nabla f) dV = \int_{dV} g \nabla f dS$$

Finally, formulating this as a matrix equation gives an expression for the Laplacian operator,

$$\boldsymbol{L}^{(2)} = \boldsymbol{\Gamma} - (\boldsymbol{DB})^\top \boldsymbol{W} (\boldsymbol{DB})$$
$$\boldsymbol{\Gamma}_j = \int_{\partial\Omega} \phi_j \nabla u \cdot \boldsymbol{n} d\boldsymbol{\xi}.$$

We now have all the operators necessary to solve Helmholtz and Poisson problems which are fundamental steps in the time stepping of the Navier-Stokes equations.

3.2.3 Global Assembly

A one-dimensional domain, Ω, is divided up into N_e elements, each expanded using an expansion of P polynomials. The above fundamental matrices are constructed separately on each element, and then combined using Global Assembly (sometimes known as Direct Stiffness Assembly). This produces a global matrix system with $P_g = N_e \times (P-1) + 1$ modes. Global Assembly is performed through the use of a sparse assembly matrix A which maps the block-concatenated local matrices into a global matrix. Given its sparsity it is implemented as a mapping matrix, mapping local mode numbers onto global mode numbers. In the one-dimensional formulation, this mapping is relatively straightforward

due to the clear arrangement of the physical nodes and spectral modes in the system. More details of the exact nature of A will be given in Sec. 3.3.1 in the context of the two-dimensional case. We will work with the global system in what follows, denoting such matrices using a subscript $\boldsymbol{g}$.

3.2.4 Solving Linear Partial Differential Equations

We now describe how to apply the underlying discretisation, detailed in Sec. 3.1, to solve a PDE. After discussing the procedure for constructing and assembling the time-stepping algorithm, we will give a practical example by solving the heat equation. In formulating the procedure, first consider the one-dimensional linear parabolic PDE

$$\frac{\partial u(x)}{\partial t} = \sum_r \lambda_r(x)\mathcal{L}_r u(x), \text{with}$$
$$\mathcal{L}_r = \frac{\partial^r}{\partial x^r}.$$

To solve this problem numerically using a spectral element method, the equation must be discretised in space and time. Initially the PDE is expressed in the weak Galerkin form,

$$\left(v, \frac{\partial u}{\partial t}\right) = \sum_r \lambda_r \left(v, \mathcal{L}_r u\right)$$

for a function, $v \in \mathcal{V}$, the test function space. For the Galerkin formulation of the method of weighted residuals, the test space and trial spaces are the same subset of L^2 and consequently both u and v are expanded in terms of the same basis $\phi_p(x)$. This gives

$$\left(\sum_j \hat{v}_j\phi_j, \sum_p \frac{\partial \hat{u}_p}{\partial t}\phi_p\right) = \sum_r \lambda_r \left(\sum_j \hat{v}_j\phi_j, \sum_p \hat{u}_p\mathcal{L}_r\phi_p\right)$$
$$\sum_p\sum_j \hat{v}_j \left(\phi_p, \phi_j\right) \frac{\partial \hat{u}_p}{\partial t} = \sum_r\sum_p\sum_j \lambda_r\hat{v}_j \left(\phi_j, \mathcal{L}_r\phi_p\right) \hat{u}_p.$$

This gives rise to the matrix system

$$\boldsymbol{v_g}^\top \boldsymbol{M_g} \frac{\partial \hat{\boldsymbol{u}}_{\boldsymbol{g}}}{\partial t} = \sum_r \lambda_r \boldsymbol{v_g}^\top \boldsymbol{L_g^{(r)}} \hat{\boldsymbol{u}}_{\boldsymbol{g}}$$

or, more concisely,

$$\begin{aligned} \frac{\partial \hat{\boldsymbol{u}}_{\boldsymbol{g}}}{\partial t} &= \boldsymbol{F_g} \hat{\boldsymbol{u}}_{\boldsymbol{g}} \\ \boldsymbol{F_g} &= \boldsymbol{M_g}^{-1} \sum_r \lambda_r \boldsymbol{L_g^{(r)}}. \end{aligned}$$

The effect of the choice of time discretisation on the stability of the numerical scheme is well known. Notably, explicit schemes are associated with severe time-step restrictions. To this end, multi-step time-discretisation schemes are considered. The generalised S-step scheme can be applied to the linear PDE as follows

$$\frac{\gamma_0 \hat{\boldsymbol{u}}_{\boldsymbol{g}}^{n+1} - \sum_{s=0}^{S-1} \alpha_s \hat{\boldsymbol{u}}_{\boldsymbol{g}}^{n-s}}{\Delta t} = \boldsymbol{F_g} \sum_{s=0}^{S-1} \beta_s \hat{\boldsymbol{u}}_{\boldsymbol{g}}^{n+1-s}. \tag{3.5}$$

From this we can identify four popular choices.

- Explicit Euler: $\gamma_0 = 1$, $\alpha_0 = 1$, $\alpha_{s\neq 0} = 0$, $\beta_1 = 1$, $\beta_{s\neq 1} = 0$.
- Implicit Euler: $\gamma_0 = 1$, $\alpha_0 = 1$, $\alpha_{s\neq 0} = 0$, $\beta_0 = 1$, $\beta_{s\neq 0} = 0$.
- Crank-Nicolson: $\gamma_0 = 1$,$\alpha_0 = 1$, $\alpha_{s\neq 0} = 0$, $\beta_0 = 1/2$, $\beta_1 = 1/2$, $\beta_{s\neq 0} = 0$.
- Second-order Adams-Bashforth: $\gamma_0 = 1$, $\alpha_0 = 1$, $\alpha_{s\neq 0} = 0$, $\beta_1 = 3/2$, $\beta_2 = -1/2$ else $\beta_s = 0$.

The explicit case introduces a time-step restriction, while the implicit scheme is not so restrictive and works well for diffusive and forcing terms. Advective terms are more susceptible to instability and so a higher order multi-step method should be used.

We will finally consider how to apply boundary conditions in our spectral element formulation. To apply Dirichlet boundary conditions in a spectral element method, the

most common procedure is to *lift* those modes which are non-zero at the boundary out of the system. The (known) contributions of these boundary modes are then accounted for in a reduced linear system. Thus, given the implicit system $\boldsymbol{A_g}\hat{\boldsymbol{u}}_{\boldsymbol{g}}^{n+1} = \hat{\boldsymbol{u}}_{\boldsymbol{g}}^{n}$ of P_g equations, the application of the boundary conditions is given by the reduced system of $P_g - 2$ equations

$$\tilde{\boldsymbol{A}}_{\boldsymbol{g}}\tilde{\hat{\boldsymbol{u}}}_{\boldsymbol{g}}^{n+1} = \tilde{\hat{\boldsymbol{u}}}_{\boldsymbol{g}}^{n} - \left(\tilde{\hat{\boldsymbol{u}}}_{\boldsymbol{g}}^{n+1}[0]\right)\boldsymbol{\alpha} - \left(\tilde{\hat{\boldsymbol{u}}}_{\boldsymbol{g}}^{n+1}[P_g - 3]\right)\boldsymbol{\beta}$$

where $\boldsymbol{u_g}[i]$ denote the ith entry of the vector $\boldsymbol{u}$ and $\boldsymbol{\alpha}$ and $\boldsymbol{\beta}$ are the first and last column of $\boldsymbol{A}$ as shown below.

$$\boldsymbol{A_g} = \begin{pmatrix} \boldsymbol{A}_{\boldsymbol{g}}^{0,0} & \cdots & \boldsymbol{A}_{\boldsymbol{g}}^{0,P_g-1} \\ \boldsymbol{\alpha}^0 & & \boldsymbol{\beta}^0 \\ \vdots & \tilde{\boldsymbol{A}}_{\boldsymbol{g}} & \vdots \\ \boldsymbol{\alpha}^{P_g-3} & & \boldsymbol{\beta}^{P_g-3} \\ \boldsymbol{A}_{\boldsymbol{g}}^{P_g-1,0} & \cdots & \boldsymbol{A}_{\boldsymbol{g}}^{P_g-1,P_g-1} \end{pmatrix}.$$

A description of the implementation of the 1D heat equation is given in App. B.

3.3 Formulation in 2-Dimensions

A spectral element method for two-dimensional domains can be formulated in a similar manner to the one-dimensional case. However, there are some extra complications introduced by the additional spatial dimension, which shall be addressed first. Such complications are primarily concerned with the ordering of the nodes and modes within the local and global context.

A two-dimensional mesh of elements gives rise to further geometric freedom in the positioning of nodes and the arrangement of elements in a conformal or non-conformal manner. A conformal mesh is one in which each element edge is shared

with only one other element which results in typically regular grids of elements. A non-conformal mesh is one in which an element may share one edge with multiple elements and is relevant when implementing an elemental h-refinement algorithm. This technique is commonly used to improve the accuracy of localised high-gradient solutions, such as turbulence simulations (Henderson and Karniadakis [1995]), without requiring a high resolution across the entire domain. The non-conformal method uses a general patching technique which connects the solution on multiple subdomains separated by interfaces (called *patches*) and placing no restrictions on the connectivity of the elements. The ability to dynamically refine elements during the lifetime of a simulation is not essential for the low to moderate Reynolds numbers considered in this thesis, and so we will restrict the remaining discussion to the simpler conformal case.

3.3.1 Global Assembly

The synergy of polynomial expansions and elemental decomposition requires efficient management of a solution on the domain. It is essential to define an orientation for each element and a unique ordering for the various element components, such as quadrature points and modes, both on a local and global scale. This requirement is of greater importance in more complex higher dimensional formulations and so we now add rigour to the brief description given in the one-dimensional case. We will describe the global numbering of quadrature points only, since the elemental modes may be numbered in an identical way.

Definition (Element orientation) An element, e, defined by four nodes $e_0, \ldots, e_3$ has an orientation as inferred by the primary coordinate direction, $e_0 \rightarrow e_1$, and the secondary coordinate direction, $e_0 \rightarrow e_3$.

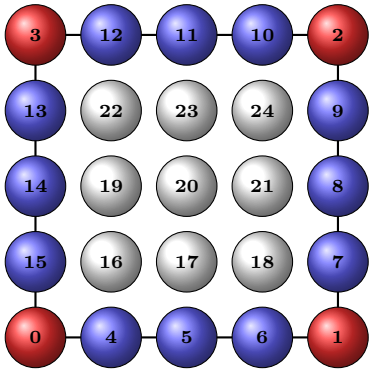

Figure 3.3: Quadrature point ordering for a 2D element. Points are ordered as corners, edges and then interior points.

Definition (Elemental ordering) Given an element, e, with fixed orientation, the local elemental quadrature points are ordered as follows (see Fig. 3.3):

- $e_0, \ldots, e_3$ (corner nodes);
- quadrature points $e_{i,1}, \ldots, e_{i,Q-2}$ on edge i defined by nodes e_i and e_{i+1};
- interior quadrature points with the fastest index being that of the primary coordinate (see Fig. 3.3).

The assembly of two or more elements gives rise to a five-partition global classification of points/modes, with the extra categories being a consequence of the distinction between elemental boundary points on the domain boundary and those interior to the domain which are common to two adjacent elements.

Definition In the same manner as for a single element the global ordering of elemental quadrature points is defined as:

- surface corner points - element corner nodes on the boundary of the domain;
- surface edge points - element edge points on the boundary of the domain;

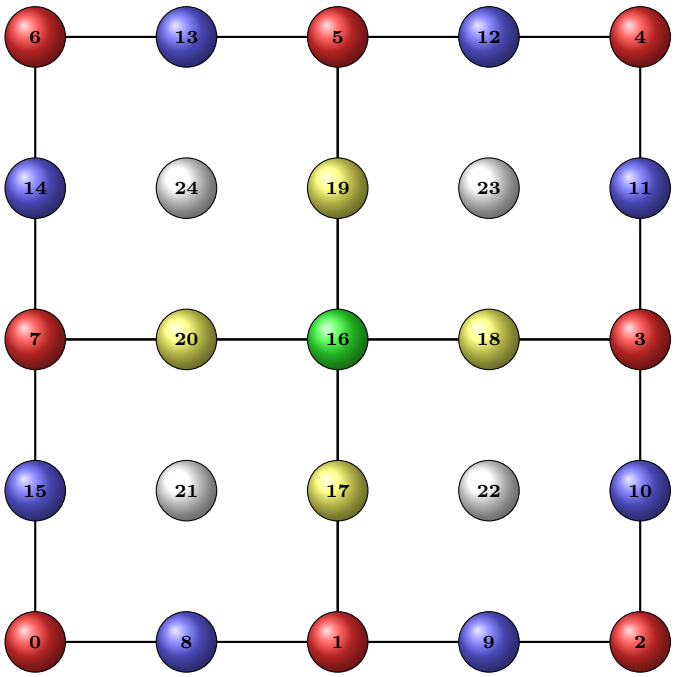

Figure 3.4: Global ordering for a two-dimensional element. This shows the ordering of quadrature points on a simplified mesh of four elements.

- interior corner points - element corner nodes interior to the domain;
- interior edge points - element edge points interior to the domain;
- element-interior points - all points interior to elements.

This choice of ordering brings several benefits to the efficiency of the two-dimensional formulation. Primarily, it separates those nodes on which boundary conditions are imposed from those purely governed by the PDE. This is achieved by the *lifting* technique described earlier. The global ordering is demonstrated graphically in Fig. 3.4.

Another benefit is in the computationally efficient construction of the numerical system for time-stepping the PDE. The choice of global ordering produces a matrix

system with the following structure.

$$\left(\begin{array}{c|c|c} \boldsymbol{M_B} & \overline{\boldsymbol{M_{BC}}} & \overline{\boldsymbol{M_{BI}}} \\ \hline \boldsymbol{M_{BC}} & \boldsymbol{M_C} & \overline{\boldsymbol{M_{CI}}} \\ \hline \boldsymbol{M_{BI}} & \boldsymbol{M_{CI}} & \boldsymbol{M_I} \end{array}\right)$$

Only the domain-interior nodes need to be determined at each time step, and the structure of $\mathbf{M_I}$ is block diagonal due to the pairwise orthogonality of each set of element-interior modes. This gives the potential to apply further numerical optimisation.

Finally, an assembly matrix is defined to translate between the local and global formulations. Such a matrix in full would be very large and sparse and thus, for storage and computational efficiency, this matrix is typically stored as a mapping array - specifying a global node/mode number for each local node/mode of each element, subject to the local and global orderings outlined above. An algorithm for global assembly is given in App. A.5.

3.3.2 Two-dimensional Quadrature Points and Modes

Before formulating the operators required for implementing a two-dimensional spectral element solver we briefly clarify the notation for the two-dimensional quadrature points and modes on the standard element. There are two coordinates (ξ_1, ξ_2) and a point is denoted by the multi-index $\boldsymbol{q}$, $\xi_{\boldsymbol{q}=\boldsymbol{q}(q_1,q_2)} = (\xi_{q_1}, \xi_{q_2})$, and the modes, indexed by the multi-index $\boldsymbol{p}$, are formed as a tensor product of two sets of one-dimensional modes, $\phi_{\boldsymbol{p}=\boldsymbol{p}(p_1,p_2)} = \phi_{p_1}\phi_{p_2}$.

3.3.3 Integration and Differentiation in 2D

Integration in two dimensions has the same basic construction as the one-dimensional formulation, with the exception that the summation indexes over two coordinates and therefore there are two weightings, each one associated with the 1-D mode in the two coordinates.

$$\int_{\bar{\Omega}} u(\xi)\mathrm{d}\xi = \sum_{\boldsymbol{q}} w_{q_1} w_{q_2} u(\xi_{q_1}, \xi_{q_2}),$$
$$w_q = \int_{\bar{\Omega}} \phi_q(\xi)\mathrm{d}\xi.$$

The construction of matrices to perform differentiation is complicated by the move to two dimensions since a separate derivative matrix is required to differentiate in each direction. The matrices $\boldsymbol{D}_1$ and $\boldsymbol{D}_2$ store the derivative of each Lagrange interpolation function, $h_{\boldsymbol{r}}$, (through the quadrature points) at each of the quadrature points, $\boldsymbol{q}$, on the standard element. The matrix $\boldsymbol{D}_1$ and $\boldsymbol{D}_2$ are constructed as

$$\boldsymbol{D}_1[\boldsymbol{q}(q_1,q_2)][\boldsymbol{r}(r_1,r_2)] = \left.\frac{dh_{r_1}(\xi)}{d\xi_1}\right|_{\xi_{q_1}} h_{r_2}(\xi_{q_2}),$$
$$\boldsymbol{D}_2[\boldsymbol{q}(q_1,q_2)][\boldsymbol{r}(r_1,r_2)] = h_{r_1}(\xi_{q_1}) \left.\frac{dh_{r_2}(\xi)}{d\xi_2}\right|_{\xi_{q_2}}.$$

3.3.4 Spectral Transforms and Operators in Two Dimensions

As with the one-dimensional formulation, two fundamental matrices are needed to allow the transform to and from spectral space, in addition to the ability to perform numerical integration. Assuming these operators are constructed in the self-consistent way described below, a full spectral element time-stepping system can be constructed in exactly the same way as before.

The elements of the basis matrix $\boldsymbol{B}[\boldsymbol{p}][\boldsymbol{q}]$ are the evaluation of each of the basis polynomials $\phi_{\boldsymbol{p}}$ at the point $\boldsymbol{q}$. This matrix is of size $P^2 \times Q^2$. The P^2 modes and Q^2

nodes are ordered as per the global mode and node orderings, respectively.

$$\boldsymbol{B}[\boldsymbol{p}][\boldsymbol{q}] = \phi_{p_1}(\xi_{q_1})\phi_{p_2}(\xi_{q_2})$$

The procedure to integrate in two dimensions is virtually identical to that in one dimension. The elemental mapping for a two-dimensional element is, however, slightly less trivial than that for a one-dimensional element. The Gaussian quadrature weights are multiplied by the Jacobian determinant of the elemental mapping. Therefore,

$$\boldsymbol{W}[\boldsymbol{q}][\boldsymbol{r}] = \boldsymbol{W}[q_1][q_1] \cdot \boldsymbol{W}[q_2][q_2] \cdot J(\xi_{q_1}, \xi_{q_2})\delta_{\boldsymbol{qr}}.$$

The weights are ordered using the same nodal ordering to correspond to $\boldsymbol{B}$.

3.3.5 Derivative Operators

The Laplacian operator seen previously can be expressed in the form of 2D local coordinates as

$$(\nabla u, \nabla v) = \left(\frac{\partial v}{\partial \xi_1}, \frac{\partial u}{\partial \xi_1}\right) + \left(\frac{\partial v}{\partial \xi_2}, \frac{\partial u}{\partial \xi_2}\right).$$

The operators $\frac{\partial}{\partial \xi_1}$ and $\frac{\partial}{\partial \xi_2}$ will be represented by the matrices $\boldsymbol{D}_1$ and $\boldsymbol{D}_2$ respectively. These operate on a solution in physical space, so to differentiate a function represented in spectral space, we would use $\boldsymbol{D}_1\boldsymbol{B}$ and $\boldsymbol{D}_2\boldsymbol{B}$. These can be used to construct, for example, the Laplacian operator,

$$\boldsymbol{L}^{(\mathbf{2})} = (\boldsymbol{D}_1\boldsymbol{B})^\top \boldsymbol{W}(\boldsymbol{D}_1\boldsymbol{B}) + (\boldsymbol{D}_2\boldsymbol{B})^\top \boldsymbol{W}(\boldsymbol{D}_2\boldsymbol{B})$$

on the standard element, which differentiates in both coordinate directions.

Derivative Operators on Arbitrary elements

Now consider applying the chain rule to the gradient operator

$$\nabla = \begin{bmatrix} \frac{\partial}{\partial x_1} \\ \frac{\partial}{\partial x_2} \end{bmatrix} = \begin{bmatrix} \frac{\partial \xi_1}{\partial x_1}\frac{\partial}{\partial \xi_1} + \frac{\partial \xi_2}{\partial x_1}\frac{\partial}{\partial \xi_2} \\ \frac{\partial \xi_1}{\partial x_2}\frac{\partial}{\partial \xi_1} + \frac{\partial \xi_2}{\partial x_2}\frac{\partial}{\partial \xi_2} \end{bmatrix} = \begin{bmatrix} \frac{\partial \xi_1}{\partial x_1} & \frac{\partial \xi_2}{\partial x_1} \\ \frac{\partial \xi_1}{\partial x_2} & \frac{\partial \xi_2}{\partial x_2} \end{bmatrix} \begin{bmatrix} \frac{\partial}{\partial \xi_1} \\ \frac{\partial}{\partial \xi_2} \end{bmatrix}.$$

The Laplacian operator on an arbitrary element can be expressed as

$$(\nabla u, \nabla v) = \left(\frac{\partial v}{\partial x_1}, \frac{\partial u}{\partial x_1}\right) + \left(\frac{\partial v}{\partial x_2}, \frac{\partial u}{\partial x_2}\right).$$

The chain rule is used to translate the differentiation operators constructed for the standard element onto an arbitrary element, giving

$$\begin{aligned}(\nabla u, \nabla v) = &\left(\frac{\partial \xi_1}{\partial x_1}\frac{\partial v}{\partial \xi_1} + \frac{\partial \xi_2}{\partial x_1}\frac{\partial v}{\partial \xi_2}, \frac{\partial \xi_1}{\partial x_1}\frac{\partial u}{\partial \xi_1} + \frac{\partial \xi_2}{\partial x_1}\frac{\partial u}{\partial \xi_2}\right) \\ &+ \left(\frac{\partial \xi_1}{\partial x_2}\frac{\partial v}{\partial \xi_1} + \frac{\partial \xi_2}{\partial x_2}\frac{\partial v}{\partial \xi_2}, \frac{\partial \xi_1}{\partial x_2}\frac{\partial u}{\partial \xi_1} + \frac{\partial \xi_2}{\partial x_2}\frac{\partial u}{\partial \xi_2}\right).\end{aligned}$$

Computationally, this means that the derivative matrices $\boldsymbol{D}_1$ and $\boldsymbol{D}_2$ are pre-multiplied by diagonal matrices of the form $\boldsymbol{\Lambda}\left(\frac{\partial \xi_k}{\partial x_l}\right)$. These represent a diagonal matrix of a derivative of the element map, evaluated at the quadrature point (ξ_{q_1}, ξ_{q_2}) and take the form

$$\boldsymbol{\Lambda}^e_{k,l}[\boldsymbol{q}][\boldsymbol{r}] = \boldsymbol{\Lambda}^e\left(\frac{\mathrm{d}\xi_k}{\mathrm{d}x_l}\right)[\boldsymbol{q}][\boldsymbol{r}] = \left.\frac{\mathrm{d}\xi_k}{\mathrm{d}x_l}\right|_{(\xi_{q_1}, \xi_{q_2})} \delta_{bmqr}.$$

This gives rise to the matrix form of the Laplacian,

$$\begin{aligned}\boldsymbol{L}^e = &\left[\left(\boldsymbol{\Lambda}^e_{1,1}\boldsymbol{D}^{\boldsymbol{e}}_{\boldsymbol{1}} + \boldsymbol{\Lambda}^e_{2,1}\boldsymbol{D}^{\boldsymbol{e}}_{\boldsymbol{2}}\right)\boldsymbol{B}^e\right]^\top \boldsymbol{W}^e \left[\boldsymbol{\Lambda}^e_{1,1}\boldsymbol{D}^{\boldsymbol{e}}_{\boldsymbol{1}} + \boldsymbol{\Lambda}^e_{2,1}\boldsymbol{D}^{\boldsymbol{e}}_{\boldsymbol{2}}\right]\boldsymbol{B}^e \\ &+ \left[\left(\boldsymbol{\Lambda}^e_{1,2}\boldsymbol{D}^{\boldsymbol{e}}_{\boldsymbol{1}} + \boldsymbol{\Lambda}^e_{2,2}\boldsymbol{D}^{\boldsymbol{e}}_{\boldsymbol{2}}\right)\boldsymbol{B}^e\right]^\top \boldsymbol{W}^e \left[\boldsymbol{\Lambda}^e_{1,2}\boldsymbol{D}^{\boldsymbol{e}}_{\boldsymbol{1}} + \boldsymbol{\Lambda}^e_{2,2}\boldsymbol{D}^{\boldsymbol{e}}_{\boldsymbol{2}}\right]\boldsymbol{B}^e. \qquad (3.7)\end{aligned}$$

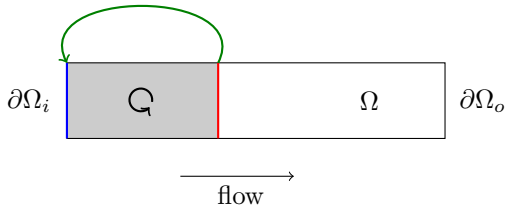

Figure 3.5: Diagram of the *copy boundary condition*. The inlet boundary $\partial\Omega_i$ is assigned the field values from a cross section of the domain downstream of the inflow, enforcing a periodic section at the start of the domain.

3.4 Copy Boundary Condition

The generation of turbulence by direct numerical simulation in a shear flow requires significant simulation time to allow the flow to transition from a laminar initial condition to the turbulent regime. This can be achieved relatively inexpensively in a domain with periodic boundaries, but much less so in one with in-flow and out-flow boundaries. This is because in these circumstances a long inflow is required prior to the region of interest to allow a steady inflow velocity profile to transition to a fully turbulent state. This drastic increase in domain size is costly in terms of the computational requirements.

To facilitate the simulation of turbulent flows in arbitrary geometries, we implement a new boundary condition to the existing numerical code base to generate a time-dependent turbulent velocity field at the inlet. The source of the inflow boundary data should in principle be the outflow of a separate periodic domain in which a turbulent flow is maintained. Equivalently, the boundary data can replicate a slice through the domain at a position downstream of the inlet, with the enclosed region being initialised with a fully-developed turbulent flow (see Fig. 3.5). The result is a pseudo-periodic section in which turbulent flow is maintained while simultaneously driving the flow in the downstream part of the domain. The entire flow is driven by either a constant body force per unit mass, or a method of flowrate control if available.

```
<BCS>
    1    C    4
             <C> u = (1,4,10,2)(21,4,30,2)(41,4,50,2)(61,4,70,2) </C>
             <C> v = (1,4,10,2)(21,4,30,2)(41,4,50,2)(61,4,70,2) </C>
             <C> w = (1,4,10,2)(21,4,30,2)(41,4,50,2)(61,4,70,2) </C>
             <C> p = (1,4,10,2)(21,4,30,2)(41,4,50,2)(61,4,70,2) </C>
    ...
</BCS>
```

Figure 3.6: Example of a *copy boundary condition* session file entry. This indicates that all four fields on the domain surfaces belonging to group c have their boundary values imposed by downstream data. In this example, the inlet is side 4 of elements 1, 21, 41 and 61, and the values are copied from side 2 of elements 10, 30, 50 and 70.

3.4.1 Implementation

Implementation is achieved through the creation of an additional boundary condition and, due to the modular nature of the existing software, it is easily integrated into the code base. Unlike the other types of boundary conditions which impose a single boundary value or analytic function, the *copy boundary condition* requires an element-side mapping as a parameter. Specifying element-side mappings ensures the velocity data can be extracted directly from the solution fields without needing computationally expensive data interpolation at every time step. Furthermore, unlike the other existing boundary conditions, the *copy boundary condition* requires access to the full field data.

A *copy boundary condition* is specified using a sequence of quartets (e_d, s_d, e_s, s_s) mapping side s_s of element e_s to side s_d of element e_d. Figure 3.6 shows an example session file entry. We now present the implementation of the boundary condition itself. The `EssentialCopy` class is derived from the base `Condition` class and applies a boundary condition in the context of a single element edge.

Locating the source data

A code excerpt for computing the location within the data field of the source data is given in Fig. 3.7. This is an auxiliary routine for the code given in Fig. 3.8. The applicable mapping information (`src_id, src_side`), in the context of side `S` of element `E`, is first retrieved from the list of mappings, `_mappings`, before the start point and stride are computed based on the source element ID and source edge. The mapping information is set in the class constructor prior to time stepping.

Retrieving the boundary data

The boundary is time dependent and evaluated at every time step. The routine for retrieving the boundary data from the solution of the previous timestep and placing into external storage is shown in Fig. 3.8. A further optimisation is made here by allowing boundary conditions to be either evaluated in physical space (such as standard Dirichlet/Neumann conditions) or in Fourier space (denoted with the suffix `F` in the routine shown). Since the majority of the time stepping is performed in spectral space, this eliminates the need to transform the data fields to physical space prior to evaluating this boundary condition. Other boundary conditions, which must be evaluated in physical space, are applied to the external storage area first. This is then transformed before the *copy boundary condition* is applied.

Applying the boundary data

The boundary data in external storage is applied to the domain during the final Helmholtz solve of the multi-step scheme using the routine in Fig. 3.9. The `Veclib::scatr` routine distributes the values in external storage, `src`, to the field storage using the boundary map, `bmap`.

```
void EssentialCopy::computeOffset( const int_t np,
                                   const Element* E,
                                   const int_t S,
                                   int_t& src_offset,
                                   int_t& src_skip ) const
{
  const char routine[] = "EssentialCopy::computeOffset";

  int_t dst_id = E->ID();
  int_t src_id = -1;
  int_t src_side = -1;
  for (unsigned int i = 0; i < _mappings.size(); ++i) {
    if (_mappings[i].mBCElmt->ID() == dst_id
          && _mappings[i].mBCSide == S) {
        src_id = _mappings[i].mSrcElmt->ID();
        src_side = _mappings[i].mSrcSide;
        break;
    }
  }
  if (src_id == -1)
    message (routine, "can't find element to copy from", ERROR);

  src_offset = (src_id)*np*np;
  src_skip = 1;

  switch (src_side) {
  case 0: src_offset += 0;               src_skip = 1;  break;
  case 1: src_offset += np - 1;          src_skip = np; break;
  case 2: src_offset += np * (np - 1);   src_skip = 1;  break;
  case 3: src_offset += 0;               src_skip = np; break;
  default:
    char err[256];
    sprintf (err, "cannot construct edge %1d", src_side);
    message (routine, err, ERROR);
  }
}
```

Figure 3.7: Code excerpt of the source data location routine. This computes the position of the source data for the target element boundary associated with this instance of the class.

```
void EssentialCopy::evaluateF (const int_t    np   ,
               const int_t    id   ,
               const int_t    nz   ,
               const Element* E    ,
               const int_t    S,
               const int_t    step,
               const real_t*  nx   ,
               const real_t*  ny   ,
               real_t*        tgt  ,
               const real_t*  data,
               char           name ) const
{
  const char routine[] = "EssentialCopy::evaluate";

  int_t src_offset = 0;
  int_t src_skip = 1;
  int_t dst_skip = 1;

  computeOffset(np, E, S, src_offset, src_skip);

  const int_t nplane    = Geometry::planeSize();
  const real_t *src     = data + src_offset + nz*nplane;

  // Reverse order if target is the 3rd or 4th side.
  if (side > 1) dst_skip = -1;

  Veclib::copy (np, src, src_skip, tgt, dst_skip);
}
```

Figure 3.8: Code excerpt of the source data retrieval routine. This extracts the boundary data from the field and places it into the external boundary storage. The `Veclib::copy` routine performs a strided memory copy, but also accounts for the orientation of the destination and source elements.

```
void EssentialCopy::set (const int_t   S,
                         const int_t*  bmap,
                         const real_t* src ,
                         real_t*       tgt ) const
{
  const int_t  nm    = Geometry::nP() - 1;
  const int_t* start = bmap;

  switch (S) {
  case 1: start += nm;           break;
  case 2: start += nm + nm;      break;
  case 3: start += nm + nm + nm; break;
  default: break;
  }

  Veclib::scatr (nm, src, start, tgt);
  if   (side == 3) tgt[bmap [ 0]] = src[nm];
  else             tgt[start[nm]] = src[nm];
}
```

Figure 3.9: Code excerpt of the routine to apply the boundary condition. This applies the boundary data in external storage to the global data field boundaries using the global boundary map.

3.4.2 Example

As an example to demonstrate the use of the *copy boundary condition* we apply it to a non-periodic pipe of length $L = 30D$. In this example the left boundary (inflow) uses the new boundary condition to duplicate the velocity and excess pressure fields at the location 5D downstream of the inlet. The right boundary (outflow) is a standard stress-free outflow boundary condition. The flow field in the 5D periodic section is initialised from a turbulent flow (generated using a 5D periodic pipe) and a constant body force is applied to drive the flow. Figure 3.10 shows transverse velocity magnitude

$$q(x, r) = \sqrt{u_r^2 + u_\theta^2} \tag{3.8}$$

at four time instances. These images show clearly the effect of the *copy boundary condition*, with the periodicity being lost downstream. This will be used in Chapter 6.

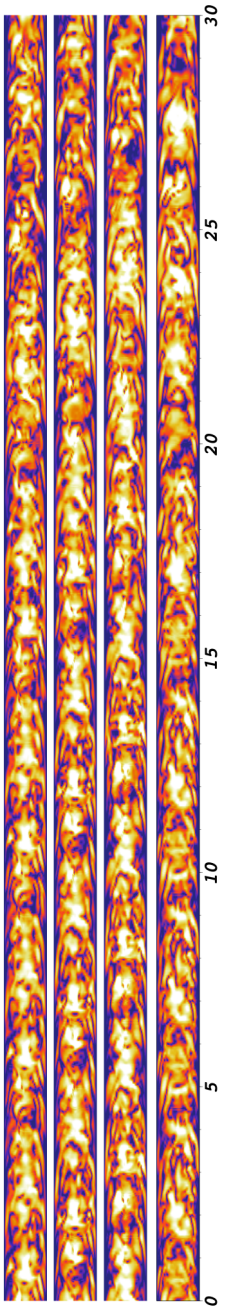

Figure 3.10: Example flow using the *copy boundary condition*. Transverse velocity magnitude of four snapshots of flow through a periodic pipe of length $L = 30D$ at Re=3000 is shown. It employs the *copy boundary condition* around the first 5D upstream. Upstream the flow is strongly periodic, but 20D downstream it has lost this periodicity.

3.5 Numerical Schemes for the Incompressible Navier-Stokes Equations

The unsteady incompressible Navier-Stokes equations enforce the fundamental laws of conservation of mass and conservation of momentum on a fluid. While there have been many numerical algorithms devised for time-stepping the Navier-Stokes equations, we choose to focus on the stiffly-stable multi-step formulation described in Orszag et al. [1986] and Karniadakis et al. [1991]. The stiffly-stable aspect of such a scheme is essential to ensure the stability of the algorithm when using higher-order integration. This is also the formulation employed by the code-base used for the numerical results presented throughout this thesis.

3.5.1 Derivation

In general, split-step methods break up the action of a single time-step operation into a series of sub-steps. Specifically, these are for the non-linear advection, pressure and viscous terms, each requiring a correct choice of boundary conditions. Furthermore, the final velocity field at the end of the time step should satisfy the divergence-free condition. The scheme we follow is termed a *pressure correction* scheme as the pressure is chosen in such a way so as to ensure the velocity field satisfies the divergence-free condition at the end of the time-step.

We begin with the unsteady incompressible Navier-Stokes equations from Eqns. (1.1) which we restate here for convenience.

$$\partial \boldsymbol{u}_t + (\boldsymbol{u} \cdot \nabla)\boldsymbol{u} = -\frac{1}{\rho}\nabla p + Re^{-1}\nabla^2 \boldsymbol{u},$$

$$\nabla \cdot \boldsymbol{u} = 0.$$

Integrating in time over a single time step results in the semi-discrete form

$$\boldsymbol{u}^{n+1} - \boldsymbol{u}^n = -\int_{t_n}^{t_{n+1}} \nabla p \; dt + Re^{-1} \int_{t_n}^{t_{n+1}} \nabla^2 \boldsymbol{u} \; dt - \int_{t_n}^{t_{n+1}} (\boldsymbol{u} \cdot \nabla)\boldsymbol{u} \; dt$$

from which we formulate the three sub-steps to evaluate the three integrals on the RHS.

An explicit-implicit scheme is used. The non-linear term $(\boldsymbol{u}\cdot\nabla)\boldsymbol{u}$ is approximated using an explicit scheme which, while imposing a time-step restriction to satisfy stability requirements, reduces the computational cost when compared to an implicit formulation. The scheme typically used is one from the Adams-Bashforth family of a prescribed order N_e. This gives a discretisation of the non-linear term as

$$\int_{t_n}^{t_{n+1}} (\boldsymbol{u} \cdot \nabla)\boldsymbol{u} \; \mathrm{d}t = \Delta t \sum_{i=0}^{N_e-1} \beta_i (\boldsymbol{u}^{n-i} \cdot \nabla)\boldsymbol{u}^{n-i}$$

where the β_i's are the appropriate weights for the chosen order (see Gear [1971]).

The linear viscous term can be handled using an implicit scheme, namely one from the Adams-Moulton family of order N_i,

$$\int_{t_n}^{t_{n+1}} \nabla^2 \boldsymbol{u} \; \mathrm{d}t = \Delta t \sum_{i=0}^{N_i-1} \gamma_i \nabla^2 \boldsymbol{u}^{\boldsymbol{n-i}}.$$

Finally, the pressure term can be expressed as:

$$\int_{t_n}^{t_{n+1}} \nabla p \; \mathrm{d}t = \Delta t \nabla \bar{p}^{n+1}$$

where $\bar{p}^{n+1}$ is a pressure field computed such that the velocity field is satisfies the incompressibility constraint. Combining these approximations gives a full splitting scheme for time-stepping the incompressible Navier-Stokes equations on a domain Ω.

$$\begin{aligned}
\frac{\hat{\boldsymbol{u}} - \boldsymbol{u}^n}{\Delta t} &= -\sum_{j=0}^{N_e-1} \beta_j (\boldsymbol{u}^{n-j} \cdot \nabla)\boldsymbol{u}^{n-j} \\
\frac{\hat{\hat{\boldsymbol{u}}} - \hat{\boldsymbol{u}}}{\Delta t} &= -\nabla \bar{p}^{n+1} \\
\frac{\boldsymbol{u}^{n+1} - \hat{\hat{\boldsymbol{u}}}}{\Delta t} &= Re^{-1} \sum_{j=0}^{N_i-1} \gamma_j \nabla^2 \boldsymbol{u}^{n+1-j}
\end{aligned}$$

with Dirichlet boundary condition

$$\boldsymbol{u}^{n+1}\big|_{\partial\Omega} = \boldsymbol{u}^{0}\big|_{\partial\Omega}$$

and satisfying $\nabla\cdot\hat{\hat{\boldsymbol{u}}} = 0$. The above discretisation, in principle, gives high-order accuracy. However, the nature of the Navier-Stokes equations leads to two problems with using this classical scheme:

- poor stability at high order;
- specifying the boundary condition for the pressure substep.

3.5.2 Stiff Stability

Stiff stability has its origins in chemical kinetics and other systems of equations which are characterised by greatly differing timescales (Gear [1971]). For example consider a system of equations such as

$$\partial_t \boldsymbol{u} = \boldsymbol{M}\boldsymbol{u}$$

which has solutions $\boldsymbol{u}_i = \boldsymbol{c}_i e^{\lambda_i t}$ for eigenvalues λ_i. If the choice of $\boldsymbol{M}$ is such that the λ_i are all negative and cover a range of magnitudes, the different components of the solution will decay at vastly differing rates. Those which decay fast will control the stability of the solution. After a short time, those components will have decayed to insignificant values, but force a short time step to be taken, even though they contribute no significant information to the system.

Stiffly-stable schemes are typically achieved through discretisation using backward differentiation. A stable discretisation of the Navier-Stokes equations is given in Karniadakis et al. [1991] as:

$$\frac{\gamma_0\boldsymbol{u}^{n+1} - \sum_{j=0}^{N_i-j}\alpha_j\boldsymbol{u}^{n-j}}{\Delta t} = -\nabla\bar{p}^{n+1} - \sum_{j=0}^{N_e-1}\beta_j(\boldsymbol{u}^{n-j}\cdot\nabla)\boldsymbol{u}^{n-j} + Re^{-1}\nabla^2\boldsymbol{u}^{n+1}.$$

Note that the β_j's differ from those explicit coefficients used earlier. This results in the multi-step scheme

$$\begin{aligned}
\frac{\boldsymbol{u}^{n+1} - \sum_{j=0}^{N_i-1} \alpha_j \boldsymbol{u}^{n-j}}{\Delta t} &= -\sum_{j=0}^{N_e-1} \beta_j (\boldsymbol{u}^{n-j} \cdot \nabla)\boldsymbol{u}^{n-j} \\
\frac{\hat{\hat{\boldsymbol{u}}} - \hat{\boldsymbol{u}}}{\Delta t} &= -\nabla \bar{p}^{n+1} \\
\frac{\gamma_0 \boldsymbol{u}^{n+1} - \hat{\hat{\boldsymbol{u}}}}{\Delta t} &= Re^{-1} \nabla^2 \boldsymbol{u}^{n+1}
\end{aligned}$$

3.5.3 Pressure Correction Substep

Early approaches made assumptions about intermediate velocity field $\hat{\hat{\boldsymbol{u}}}$, assuming that

- it is incompressible: $\nabla \cdot \hat{\hat{\boldsymbol{u}}} = 0$;
- and that it satisfies the Dirichlet boundary condition: $\hat{\hat{\boldsymbol{u}}} \cdot \boldsymbol{n} = \boldsymbol{u}^0 \cdot \boldsymbol{n}$.

Consequently, the pressure term $\bar{p}^{n+1}$ can be found by taking the divergence in the second step.

$$\begin{aligned}
\nabla \cdot \left(\frac{\hat{\boldsymbol{u}}}{\Delta t} \right) &= \nabla^2 \bar{p}^{n+1} && \text{in } \Omega \\
\frac{\partial \bar{p}^{n+1}}{\partial \boldsymbol{n}} &= -\frac{\boldsymbol{u}^0 \cdot \boldsymbol{n} - \hat{\boldsymbol{u}} \cdot \boldsymbol{n}}{\Delta t} && \text{on } \partial\Omega
\end{aligned}$$

However, the second condition is not exactly true. The correct term for the pressure boundary, derived from the splitting scheme, is:

$$\frac{\partial \bar{p}^{n+1}}{\partial \boldsymbol{n}} = \boldsymbol{n} \cdot \left[\sum_{i=0}^{N_e-1} \beta_i (\boldsymbol{u}^{n-i} \cdot \nabla)\boldsymbol{u}^{n-i} + \sum_{i=0}^{N_i-1} \gamma_i \nabla^2 \boldsymbol{u}^{n-i} \right]$$

While this now correctly evaluates the pressure on the boundary, it is implicit and consequently couples the equations. Furthermore, it can not be replaced with an explicit scheme as this is numerically unstable.

The solution is to use the high-order pressure boundary condition described in Orszag et al. [1986] and Karniadakis et al. [1991] which proceeds by splitting the implicit linear viscous term into an irrotational part and a solenoidal part.

$$\frac{\partial \bar{p}^{n+1}}{\partial n} = \boldsymbol{n} \cdot \left[\sum_{i=0}^{N_e-1} \beta_i (\boldsymbol{u}^n \cdot \nabla)\boldsymbol{u}^n + \underbrace{\nu \sum_{i=0}^{N_i-1} \gamma_i \nabla Q^{n+1-q}}_{\text{Irrotational part}} + \underbrace{\nu \sum_{i=0}^{N_e-1} \beta_i \left(-\nabla \times \left(\nabla \times \boldsymbol{u}^{n-i} \right) \right)}_{\text{Solenoidal Part}} \right]$$

The solenoidal part is treated explicitly, and the irrotational part implicitly. However, the incompressibility condition makes $Q^{n+1} = 0$, decoupling the equations. This boundary condition is applicable to both schemes above with the coefficients β_i matching those in the chosen scheme.

3.5.4 Flowrate control

An ideal fluid is governed by laws which conserve both mass and momentum. The scalar pressure, p, describes the force exerted on a small unit of fluid by the surrounding fluid. At its most fundamental level the movement of fluid particles occurs due to a pressure gradient, ∇p, which drives fluid from the areas of high pressure to those of lower pressure. When time stepping the Navier-Stokes equations, this gradient is computed so as to make the pressure field match the velocity boundary conditions, particularly those applied to the inflow. This causes complications when a periodic boundary condition is required in the streamwise direction.

3.5.5 Streamwise Periodic Boundaries

In this circumstance, there is no condition to impose fluid flow in the domain (such as the fixed Dirichlet inflow in a non-periodic domain). Consequently, a zero flow will remain at rest, and a flow initially in motion will quickly lose momentum due to viscosity and lack of a pressure gradient. There are in general two methods to handle this problem:

- Enforce a pressure gradient. This essentially involves setting a non-zero forcing term, $\boldsymbol{f}$, in the Navier-Stokes momentum equation,

$$\partial \boldsymbol{u}_t + (\boldsymbol{u} \cdot \nabla)\boldsymbol{u} = -\nabla p + \nu \nabla^2 \boldsymbol{u} + \boldsymbol{f};$$

- Fix the flowrate, through the linear superposition of a Greens, $\boldsymbol{u_g}$, function with the solution,

$$\partial \boldsymbol{u}_t + (\boldsymbol{u} \cdot \nabla)\boldsymbol{u} = -\nabla p + \nu \nabla^2 \boldsymbol{u} + \alpha \boldsymbol{u_g}.$$

The choice of which method to use depends on the flow regime. For an elementary laminar pipe flow, a pressure gradient is the most effective solution. The forcing term is computed as $32/Re$. However, in the turbulent regime the pressure is necessarily higher and may fluctuate making a fixed gradient insufficient and it is necessary to use dynamic flowrate control.

The flowrate, $Q(\boldsymbol{u})$, is defined as the flux of fluid through a cross-sectional slice, $\partial\Omega$, and is given by

$$Q(\boldsymbol{u}) = \int_{\partial\Omega} u_x \, \mathrm{d}\Omega.$$

To control the flowrate at each timestep, the principle of superposition is exploited to compensate for any deviation of the flowrate from the target, $\overline{Q}$. This is a Green's function (typically the Stokes flow), which is precomputed at the beginning of the

computation. For a Stokes flow the non-linear term of the Navier-Stokes momentum equation is zero, leaving the linear equation

$$\frac{\partial \boldsymbol{u}_g}{\partial t} = -\nabla p + \nu \nabla^2 \boldsymbol{u}_g$$

and so for any solution, $\boldsymbol{u}$, to the Navier-Stokes equations, $\boldsymbol{u} + \boldsymbol{u}_g$ is also a solution.

The Stokes flow, $\boldsymbol{u}_g$, is used at the end of each timestep to augment the true flow field and achieve the target flowrate, such that

$$Q(\hat{\hat{\boldsymbol{u}}} + \alpha(t)\boldsymbol{u}_g) = \overline{Q}.$$

This necessitates the computation of $\alpha(t)$ at each time step as

$$\alpha(t) = \frac{\overline{Q} - Q(\hat{u})}{Q(\boldsymbol{u}_g)}.$$

3.6 Eigenvalue Computation

In this section we present an overview of the method used for determining eigenvalues. Throughout the history of computational linear algebra many computationally efficient algorithms have been devised which can exploit various properties of the matrix to which they are applied. In this thesis we concentrate on iterative power methods. The reasons for this are three-fold:

- The dense matrix corresponding to our typical operator, $\mathcal{A}$, lacks structure and usually has $\mathcal{O}(10^5)$ degrees of freedom, which makes computing the full spectrum particularly challenging.
- A full matrix corresponding to $\mathcal{A}$ is not directly available in the time-stepping code (due to the multi-step methodology).
- We are only interested in the most dominant eigenvalue/eigenvector pairs.

Iterative power methods overcome these issues by not requiring an explicit matrix to work on, but merely knowledge of the "effect" of the action of the matrix. The specific algorithm employed for computing eigenvalues is based on the Arnoldi method (Arnoldi [1951]). This is a generalisation of the Lanczos method for symmetric matrices, but will allow us to solve both the symmetric transient growth problems and the unsymmetric global stability problems with the same code.

For a matrix $\boldsymbol{M}$ (which may be a discretisation of $\mathcal{A}(\tau)$ or $\mathcal{A}^*(\tau)\mathcal{A}(\tau)$), the Arnoldi algorithm extracts the most dominant behaviour of the operator from a sequence of vectors obtained by repeated application of the target operator to a starting vector. This sequence spans a Krylov subspace and the algorithm essentially performs a partial Hessenberg reduction of $\boldsymbol{M}$ to allow the efficient calculation of the leading eigenvalue/eigenvector pairs.

Definition (Krylov Subspace) Given $\boldsymbol{M} \in \mathbb{R}^{n\times n}$ and a vector $\boldsymbol{u} \in \mathbb{R}^n$, the Krylov k-subspace $\mathcal{K}_n(\boldsymbol{M}, \boldsymbol{u}, k)$ generated by $\boldsymbol{M}$ is

$$\mathcal{K}_n(\boldsymbol{M}, \boldsymbol{u}, k) = span\{\boldsymbol{u}, \boldsymbol{M}\boldsymbol{u}, \boldsymbol{M}^2\boldsymbol{u}, \ldots, \boldsymbol{M}^{k-1}\boldsymbol{u}\}.$$

Using this Krylov sequence, the operator $\boldsymbol{M}$ can be approximated by a low-rank Hessenberg matrix according to the following theorem.

Theorem 3.6.1. *Given a matrix $\boldsymbol{M} \in \mathbb{R}^{n\times n}$, there exists an orthogonal matrix $\boldsymbol{Q} \in \mathbb{R}^{n\times n}$ and a matrix $\boldsymbol{H}$ in Hessenberg form such that*

$$\boldsymbol{M} = \boldsymbol{Q}\boldsymbol{H}\boldsymbol{Q}^T.$$

Proof. A proof and suitable algorithm is given in Golub and Van Loan [1996]. □

As a corollary to this theorem, we find the eigenvalues of $\boldsymbol{H}$ are equal to those of $\boldsymbol{M}$.

Corollary 3.6.2. *$\boldsymbol{M}$ and $\boldsymbol{H}$ are similar matrices and their eigenvalues are the same.*

Proof. Clearly, $\boldsymbol{Q}$ has full column rank since its columns form a basis. Thus, by definition of similar matrices $\boldsymbol{M}$ and $\boldsymbol{H}$ must be similar. From Theorem 3.6.1,

$$\boldsymbol{MQ} = \boldsymbol{QH} \Rightarrow \lambda(\boldsymbol{M}) = \lambda(\boldsymbol{H}). \qquad \square$$

Of course in practice, we would not wish to compute $\boldsymbol{H}$ to the same rank as $\boldsymbol{M}$. Instead, the principle of the Arnoldi method is to construct the matrix $\boldsymbol{Q}$ column-by-column until the eigenvalues of $\boldsymbol{H}_k = \boldsymbol{Q}_k \boldsymbol{M} \boldsymbol{Q}_k^\top$ approximate those of $\boldsymbol{M}$. In the kth iteration $\mathbf{Q}_k \in \mathbb{R}^{n \times k}$, $\mathbf{H}_k \in \mathbb{R}^{k \times k}$ and

$$\boldsymbol{MQ}_k = \boldsymbol{Q}_k \boldsymbol{H}_k + r_k \mathbf{e}_k^\top.$$

The value of r_k characterises how far the matrix $\boldsymbol{M}$ lies from the invariant space of $\boldsymbol{H}$. If $r_k = 0$ then

$$\lambda(\boldsymbol{H}) \subseteq \lambda(\boldsymbol{M}).$$

Invariably, $r_k < \epsilon$ for some tolerance ϵ and consequently the eigenvalues of $\boldsymbol{H}$ are an approximation of the leading eigenvalues of $\boldsymbol{M}$.

We now detail the algorithm used to perform the Hessenberg reduction and extract the most dangerous eigenvalues to linear stability. To achieve this in practice, we consider our Krylov sequence as a matrix with columns $\boldsymbol{u}_0, \ldots, \boldsymbol{u}_{k-1}$.

$$\boldsymbol{T}_k = [\boldsymbol{u}_0, \boldsymbol{u}_1, \ldots, \boldsymbol{u}_{k-1}]$$

where each normalised entry is computed as $\boldsymbol{u}_i = \boldsymbol{M}\boldsymbol{u}_{i-1}/||\boldsymbol{M}\boldsymbol{u}_{i-1}||$. We now follow the methodology of Barkley et al. [2008] and manipulate the governing equation which defines a Krylov sequence,

$$\boldsymbol{MT}_k = \boldsymbol{T}_{k+1}\boldsymbol{D},$$

where $\boldsymbol{D} \in \mathbb{R}^{(k+1)\times k}$ having all entries zero except for suitable normalisation factors on the first sub-diagonal, and keeps all but the first column of $\boldsymbol{T}_{k+1}$. After replacing the $\boldsymbol{T}$ matrices with their QR factorisation, $\boldsymbol{M}$ can be expressed as

$$\boldsymbol{M} = \boldsymbol{Q}_{k+1}\boldsymbol{R}_{k+1}\boldsymbol{D}\boldsymbol{R}_k^{-1}\boldsymbol{Q}_k^{-1},$$

and we define $\boldsymbol{G} \in \mathbb{R}^{(k+1)\times k}$ as $\boldsymbol{G} = \boldsymbol{R}_{k+1}\boldsymbol{D}\boldsymbol{R}_k$. The last row of $\boldsymbol{G}$ contains exactly one non-zero entry, $g_{k,k-1}$, which can be separated from the system to leave $\boldsymbol{H} = \boldsymbol{G}[0 : k-1, :] \in \mathbb{R}^{k\times k}$, an upper Hessenberg matrix containing all but the last row of $\boldsymbol{G}$. The expression for $\boldsymbol{M}$ then becomes

$$\boldsymbol{M} = \boldsymbol{Q}_k\boldsymbol{H}_k\boldsymbol{Q}_k^{-1} + g_{k+1,k}\boldsymbol{q}_k$$

This is the Hessenberg decomposition required and its structure is ensured by the combination of the upper triangular $\boldsymbol{R}_{k+1}$ and the lower diagonal $\boldsymbol{D}$. The residual term, $g_{k,k}$, provides a measure of the accuracy of the action of the Hessenberg matrix to the action of the original matrix, $\boldsymbol{M}$. In fact the terms of the matrix $\boldsymbol{H}$ can be computed explicitly using the expression

$$h_{i,j} = \frac{1}{r_{j,j}}\left(\alpha_{j+1}r_{i,j+1} - \sum_{l=0}^{j-1} h_{i,l}r_{l,j}\right),$$

from the QR factorisation and scaling factors α_j (see Barkley et al. [2008] for details). The eigenvalues of the matrix $\boldsymbol{H}$ approximate the leading eigenvalues of $\boldsymbol{M}$. Since $\boldsymbol{H}$ is of comparatively very low rank, these eigenvalues can be computed trivially. Approximations to the full eigenvectors, $\boldsymbol{V}$, can then be obtained from the low-rank eigenvectors, Ψ, using $\boldsymbol{V}_i = \boldsymbol{Q}_k\Psi_i$ for those Ψ_i whose residuals have fallen below a set tolerance.

The Krylov sequence at the k-th iteration, $\boldsymbol{T}_k$, consists of the initial condition along with $k-1$ applications of the operator $\boldsymbol{M}$. In practice, we keep only a limited number of vectors from the sequence, discarding the oldest vector each time when

this limit is reached. This is synonymous with using a restarting technique, since the Hessenberg matrix is computed in full after each iteration.

This algorithm to compute the eigenvalues is particularly efficient with the bulk of the computational effort lying in the evaluation of the operator to create the Krylov sequence. The Arnoldi algorithm is, however, particularly susceptible to the choice of initial condition (Golub and Van Loan [1996]) as initial conditions which lie orthogonal, or almost orthogonal, to the most dominant eigenvectors will result in a sequence poorly portraying the action of the operator. This is improved by discarding old vectors and limiting the size of the sequence, since numerical noise alone will eventually allow the sequence to effectively represent the most important characteristics of the operator.

3.6.1 Eigenvalue Deflation

We now turn our attention to the process of finding the sub-dominant eigenvalues of an operator. The algorithm outlined above will converge onto the leading eigenvalue without great difficulty. However, it may struggle to converge further eigenvalues of the system due to the effective resolution of the algorithm. This is especially true if the separation of the dominant eigenvalues is small, whereby the leading eigenvalues are difficult to distinguish from each other. Increasing the size of the Krylov subspace may provide a limited improvement, but the additional information regarding the action of $\boldsymbol{M}$ will still be overwhelmed by the most dominant eigenvectors. A solution is to filter out the eigenvectors already computed to expose the next most dominant eigenvectors.

Eigenvalue deflation is a procedure which allows the extraction of sub-dominant eigenvalue/eigenvector pairs in an iterative procedure by filtering out the contribution of the dominant (previously computed) eigenvectors from the system. We will first provide an overview of the algorithm followed by further details on the implementation.

We determine the contribution of each computed eigenvector to each of the vectors in the Krylov sequence by projecting the columns of $\boldsymbol{T}_k$ onto each eigenvector in turn. With this information, we then project the Krylov space onto a space orthogonal to that spanned by the computed eigenvectors. The iterative process will then continue to converge onto the next most dominant eigenvalue, that is, the most dominant eigenvalue in the orthogonal space, until the required N eigen-pairs have been computed.

Consider the Krylov sequence $\boldsymbol{T}_k = [\boldsymbol{u}_0, \ldots, \boldsymbol{u}_{k-1}]$ and the sequence of previously computed eigenvectors $\boldsymbol{V}_m = [\boldsymbol{v}_0, \ldots, \boldsymbol{v}_{m-1}]$. Define $\boldsymbol{W} \in \mathbb{R}^{k \times m}$ as $\boldsymbol{W}_{i,j} = \langle \boldsymbol{u}_i, \boldsymbol{v}_j \rangle$. These factors describe the magnitude of the contribution of each eigenvector to the vectors in the Krylov sequence.

On each iteration of the power method above, prior to computing the Hessenberg matrix $\boldsymbol{H}$, the factor matrix $\boldsymbol{W}$ is computed and the eigenvalue deflation is then performed using the operation

$$\boldsymbol{T}_k = \boldsymbol{T}_k - \boldsymbol{V}_m \boldsymbol{W}.$$

The Arnoldi process then continues to estimate λ_{m+1} and $\boldsymbol{v}_{m+1}$. Upon convergence of a new eigenvector, it is appended as an additional column to the matrix $\boldsymbol{V}$ for use in future iterations and the process continues while $m < N$.

Eventually numerical errors in the application of $\boldsymbol{M}$ will introduce noise which will sufficiently excite the filtered eigenvectors so as to reduce the effectiveness of the procedure. However, for the particular problems under consideration, it should be possible to attain at least a dozen of the dominant eigenvalues to sufficient accuracy before this becomes an issue.

```
static void EV_project(real_t* vec, real_t* evec, ostream& runinfo) {
    const int_t ND = Geometry::nPert();
    const int_t NP = Geometry::planeSize();
    const int_t NZ = Geometry::nZ();
    const int_t ntot = ND*NP*NZ;
    const int_t npnp  = Geometry::nTotElmt();
    int_t i = 0;

    // Set of domain elements
    vector<Element*> elmt = domain->elmt;

    // Iterate over elements and sum up L2 inner product contribution
    // from each one.
    real_t* f = evec;
    real_t* g = vec;
    real_t factor = 0.0;
    real_t q1 = 0.0;
    for (i = 0; i < elmt.size(); ++i, f += npnp, g += npnp) {
        factor += elmt[i] -> innerProd(f,g);
        q1 += elmt[i] -> innerProd(f,f);
    }

    // subtract off projected quantity of original eigenvector
    Blas::axpy (ntot, -factor/q1, evec, 1, vec, 1);
}
```

Figure 3.11: Code excerpt to perform eigenvalue projection. The code first computes the projection of the vector `vec` onto a second vector `evec`. The result is then subtracted from `vec`. In deflation terms, it computes the magnitude, $\langle \boldsymbol{u}_i, \boldsymbol{v}_i \rangle$, of the contribution of an eigenvector, $\boldsymbol{v}_i$, to a vector from the Krylov sequence, $\boldsymbol{u}_i$.

Implementation

Implementation of the eigenvalue deflation algorithm requires relatively trivial modifications to the outer level eigenvalue code which make use of an additional routine to perform the removal of an eigenvalues contribution to a vector (see Fig. 3.11). For each vector appended to the Krylov sequence, this routine is used to remove the contributions of the previously computed eigenvalues:

```
    for (j = 0; j < outvecs; j++) {
        EV_project(Kseq[kdim], Oseq[j], runinfo);
    }
```

Upon convergence of an eigenvector, a similar code fragment is used to project out the contribution of the newly computed eigenvector from all the vectors in the Krylov

sequence.

```
for (j = 0; j <= min(i,kdim); ++j) {
    EV_project(Kseq[j], Sseq[0], runinfo);
}
```

After the required number of eigenvectors have been computed, the algorithm terminates, as per the original algorithm. Note that in the deflation algorithm there is no requirement that the size of the Krylov sequence matches or exceeds the number of eigenvectors required since the algorithm is, in essence, only computing one eigenvector at any one time.

This concludes our review of numerical techniques which, along with the stability formulations described in Chapter 2, to the first of two problems - flow through a sudden axisymmetric expansion.

Chapter 4

Transient Growth Analysis of Flow through a Sudden Expansion in a Circular Pipe

4.1 Introduction

The dynamics of flow through abrupt geometrical expansions is of both practical importance and fundamental interest. The axisymmetric expansion (Back and Roschke [1972]; Furuichi et al. [2003]; Hammad et al. [1999]; Latornell and Pollard [1986]; Mullin et al. [2009]; Teyssandier and Wilson [1974]), in particular, is a primitive geometry occurring in numerous engineering and industrial settings. It is also relevant to bio-medical applications as a model of flow through arterial stenoses (Blackburn et al. [2008b]; Sherwin and Blackburn [2005]; Blackburn and Sherwin [2007]; Bertolotti et al. [2001]; Griffith et al. [2008]). At a fundamental level this geometry, together with the closely related planar expansion (Acrivos and Schrader [1982]; Durst et al. [1993]; Fearn et al. [1990]) and

backward-facing step (Kaiktsis et al. [1991, 1996]; Barkley et al. [2002]; Beaudoin et al. [2004]; Blackburn et al. [2008a]), serve as prototypes for understanding the dynamics of flow separation. Over the past four decades studies of these flows have addressed issues such as reattachment lengths (Back and Roschke [1972]), symmetry breaking (Mullin et al. [2009]), and time-dependence (Sreenivasan and Strykowski [1983]).

The focus of this paper is the transient linear dynamics of the 1 to 2 axisymmetric expansion. We show that for values of the Reynolds numbers well below any linear instability, the flow strongly amplifies infinitesimal inlet perturbations. We argue that transient linear amplification is a potentially more important effect in this flow than linear instability.

Much of the previous research on the axisymmetric expansion has concentrated on the steady, laminar flow regime and the accurate determination of the separation and subsequent reattachment. Both experimental (Macagno and Hung [1967]; Back and Roschke [1972]; Sreenivasan and Strykowski [1983]; Latornell and Pollard [1986]; Hammad et al. [1999]; Furuichi et al. [2003]; Mullin et al. [2009]) and computational (Macagno and Hung [1967]; Pollard [1981]; Badekas and Knight [1992]) studies find that the reattachment length varies linearly with Reynolds number in the steady regime, with the proportionality depending on whether the inlet flow is a flat profile or a fully developed Hagen–Poiseuille profile (Roschke and Back [1976]). Separation and reattachment in the turbulent regime has also been studied (Acrivos and Schrader [1982]; Tinney et al. [2006]).

Recent and carefully controlled experiments by Mullin et al. [2009] on the 1 to 2 expanding pipe flow with a fully developed inlet profile report a steady-state breaking of axisymmetry at $Re = 1139 \pm 10$. The Reynolds number is defined in terms of the inlet diameter and bulk velocity. This symmetry breaking is the rotational analog

of the symmetry breaking observed in the symmetric planar expansion (Fearn et al. [1990]; Durst et al. [1993]; Drikakis [1997]). However, in the planar case there is now general agreement between computation and experiment on the bifurcation, while in the axisymmetric case, linear stability computations by Cliffe et al. [To be published] (also verified in the present study) find that there is no bifurcation of the perfectly symmetric problem at Reynolds numbers comparable to those reported in the experiments (Mullin et al. [2009]).

Many experimental studies report unsteadiness and oscillations in the expanding-pipe flow (Back and Roschke [1972]; Iribarne et al. [1972]; Feuerstein et al. [1975]; Sreenivasan and Strykowski [1983]; Mullin et al. [2009]). There is, however, no agreement as to the Reynolds number at which oscillations first arise. The explanation for the discrepancy has been attributed to the sensitivity of the expansion to the inlet profile (Roschke and Back [1976]; Pollard [1981]; Latornell and Pollard [1986]).

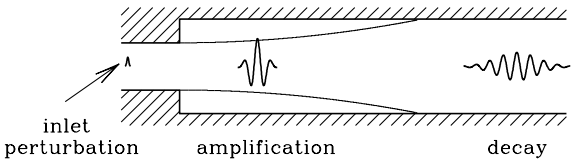

Figure 4.1: Sketch illustrating the evolution of a perturbation through an expanding pipe. Small inlet perturbations are amplified in the region of the separated axisymmetric shear layer, but eventurally decay downstream. Hence, even though the flow is linearly stable, it supports very strong transient growth of perturbations.

The aim of this paper is to quantify and highlight the importance of transient growth of infinitesimal perturbations in expanding pipe flow. Fig. 4.1 illustrates the essential idea. Small disturbances in the inlet upstream of the expansion are amplified in the region containing the separated axisymmetric shear layer following the expansion. The amplified disturbances are then advected into the downstream pipe where they in-

evitably decay. This leads to a situation in which the flow may be highly sensitive to incoming perturbations, but only transiently. Hence, even though the flow is linearly stable, in that all perturbations eventually decay and likewise all eigenvalues are negative, the flow may be highly susceptible to small perturbations. From a local perspective one would attribute the transient dynamics to a localized region of convective instability within the flow resulting from an inflectional velocity profile (Huerre and Monkewitz [1990]; Cossu and Chomaz [1997]; Chomaz [2005]). In the context of a direct numerical study where one does not resort to local parallel approximations but instead fully resolves all aspects of the flow, one understands and analyzes the transient dynamics as a transient growth problem or equivalently as a singular value problem. For example, recent studies have highlighted the importance of transient dynamics due to localized regions of convective instability for the backward-facing step (Blackburn et al. [2008a]), curved channel flow (Marquet et al. [2008b]) and steady and pulsatile stenotic flow (Blackburn et al. [2008b]). This is the approach taken in the present work.

4.2 Methodology

4.2.1 Governing Equations and Flow Geometry

The flow is governed by the incompressible Navier–Stokes equations

$$\partial_t \boldsymbol{u} + (\boldsymbol{u} \cdot \nabla)\boldsymbol{u} = -\nabla p + Re^{-1}\nabla^2 \boldsymbol{u}, \tag{4.1a}$$

$$\nabla \cdot \boldsymbol{u} = 0, \tag{4.1b}$$

where $\boldsymbol{u}$ is the fluid velocity and p is the modified or kinematic static pressure. The equations are written in dimensionless form with the velocity normalized by $\bar{U}$, the bulk velocity of the incoming flow, and lengths normalized by the diameter of the inlet pipe

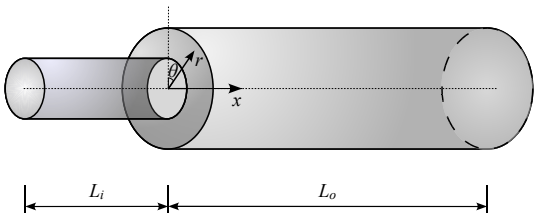

Figure 4.2: Geometry of the expanding pipe. The computational flow domain Ω is illustrated with the cylindrical coordinate system and the inlet and outlet lengths indicated (not to scale).

D. Thus the Reynolds number is the bulk Reynolds number of the inlet pipe flow given by $Re = \bar{U}D/\nu$, where ν the fluid's kinematic viscosity.

To avoid possible confusion when reading the following material it is useful to emphasize here the approach taken to non-dimensionalization. Except where indicated otherwise, all quantities reported employ the normalization used above in defining the Reynolds number. In particular this means that lengths are presented in terms of the inlet pipe diameter, D. The exception we make to this rule is in recording downstream reattachment points, where step height $h = D/2$ is also used as a measure of length. This exception is made to facilitate comparison to previous works. Throughout the paper, times are in units of $D/\bar{U}$.

The pipe geometry naturally lends itself to using cylindrical coordinates which are denoted (x, r, θ). Here x is used for the axial coordinate since this corresponds to the streamwise direction, with $x = 0$ at the expansion location. The fluid velocity in these cylindrical coordinates is thus written $\boldsymbol{u} = (u_x, u_r, u_\theta)$.

Ideally the flow geometry would be infinite in the streamwise direction. In practice, the computational flow domain Ω consists of a finite inflow region of length L_i upstream of the expansion and a finite outflow region of length L_o downstream of the expansion as in Fig. 4.2. For sufficiently large L_i and L_o, as used in this study, results

are independent of these lengths and the flow approximates the infinite case.

We impose a fully developed Hagen–Poiseuille incoming profile, which in non-dimensional form is given by $\boldsymbol{u} = 2(1-4r^2)\boldsymbol{e}_x$. We use no-slip boundary conditions on all walls of the pipe and impose a stress-free outflow boundary condition at the downstream end of the pipe. Thus the boundary conditions for the flow problem are

$$\boldsymbol{u}(\partial\Omega_i, t) = 2(1-4r^2)\boldsymbol{e}_x, \tag{4.2a}$$

$$\boldsymbol{u}(\partial\Omega_w, t) = \boldsymbol{0}, \tag{4.2b}$$

$$\boldsymbol{e}_x \cdot \nabla\boldsymbol{u}(\partial\Omega_o, t) = \boldsymbol{0}, \quad p(\partial\Omega_o, t) = 0, \tag{4.2c}$$

where $\partial\Omega_i$ is the inlet boundary at $x = -L_i$, $\partial\Omega_w$ is the boundary corresponding to the rigid walls of the inlet pipe, outlet pipe and expansion, and $\partial\Omega_o$ is the outlet boundary at $x = L_o$. Variations on these boundary conditions will appear in the stability and transient growth problems as well as for studies of noisy inflow and will be discussed at the appropriate place.

4.2.2 Linear Stability and Transient Growth Problems

We briefly summarize the main aspects of the linear stability and transient growth problems. Some further details for the particular problem are given in Sec. 4.2.3. General accounts of the time-stepper approach used here may be found elsewhere (Tuckerman and Barkley [2000]; Barkley et al. [2008]).

The first step in the analysis is to obtain base flows $\boldsymbol{U}$. In this study these are steady, two-dimensional, axisymmetric solutions to Eqns. (4.1) of the form $\boldsymbol{U} = (U_x(x,r), U_r(x,r), 0)$. For the range of Re considered in this paper, these solutions are unique functions of Re.

The next step is to consider the evolution of infinitesimal disturbances $\boldsymbol{u}'$ to the

base flow. These are governed by the linearized Navier–Stokes equations

$$\partial_t \boldsymbol{u}' + \boldsymbol{DN} \cdot \boldsymbol{u}' = -\nabla p' + Re^{-1}\nabla^2 \boldsymbol{u}', \tag{4.3a}$$

$$\nabla \cdot \boldsymbol{u}' = 0, \tag{4.3b}$$

where

$$\boldsymbol{DN} \cdot \boldsymbol{u}' \equiv (\boldsymbol{U} \cdot \nabla)\boldsymbol{u}' + (\boldsymbol{u}' \cdot \nabla)\boldsymbol{U} \tag{4.4}$$

The boundary conditions for Eqns. (4.3) will be addressed at the end of Sec. 4.2.3.

The linear evolution of a perturbation from $t = 0$ to a later time t under Eqns. (4.3) can be expressed eloquently as the action of a linear state transition operator $\mathcal{A}(t)$ on the initial perturbation $\boldsymbol{u}'(0)$ as

$$\boldsymbol{u}'(t) = \mathcal{A}(t)\boldsymbol{u}'(0). \tag{4.5}$$

We then perform an analysis, either of stability or of transient growth, for this linear evolution operator.

For linear stability, we seek normal mode solutions of the form $\boldsymbol{u}'(x, r, \theta, t) = \exp(\sigma_j t)\tilde{\boldsymbol{u}}_j(x, r, \theta) + \text{c.c.}$, where the $\tilde{\boldsymbol{u}}_j$ are eigenmodes and the σ_j are eigenvalues. For any fixed arbitrary time T (typically T is of order unity under the scaling we have used) the eigenmodes are solutions of

$$\mathcal{A}(T)\tilde{\boldsymbol{u}}_j = \mu_j \tilde{\boldsymbol{u}}_j \tag{4.6}$$

where the eigenvalues μ_j and σ_j are related by $\mu_j = \exp(\sigma_j T)$. The eigenvalues μ_j of largest modulus are found iteratively by actions of the operator $\mathcal{A}(T)$ as discussed in Sec. 4.2.3. If there exist any solutions of Eqn. (4.6) with $|\mu_j| > 1$, corresponding to σ_j with positive real part, then the base flow $\boldsymbol{U}$ is linearly unstable.

The transient growth computations consist of determining the greatest possible energy growth, G, over all initial perturbations for a given finite time horizon τ. Because

the evolution is linear, it is sufficient to consider initial perturbations with unit norm in the standard L_2 inner product $(\cdot,\cdot)$ over the flow domain Ω. Then the energy of such a perturbation after time τ, relative to the initial energy, is

$$\frac{E(\tau)}{E(0)} = ||\boldsymbol{u}'(\tau)||^2 = \left(\boldsymbol{u}'(\tau), \boldsymbol{u}'(\tau)\right),$$

where $||\boldsymbol{u}'(0)|| = 1$. Using the evolution operator $\mathcal{A}(\tau)$ and its adjoint $\mathcal{A}^*(\tau)$ this can be written as

$$\begin{aligned}\frac{E(\tau)}{E(0)} &= \left(\mathcal{A}(\tau)\boldsymbol{u}'(0), \mathcal{A}(\tau)\boldsymbol{u}'(0)\right) \\ &= \left(\boldsymbol{u}'(0), \mathcal{A}^*(\tau)\mathcal{A}(\tau)\boldsymbol{u}'(0)\right).\end{aligned}$$

Let λ_j and $\boldsymbol{v}_j$ denote eigenvalues and normalized eigenmodes of $\mathcal{A}^*(\tau)\mathcal{A}(\tau)$:

$$\mathcal{A}^*(\tau)\mathcal{A}(\tau)\boldsymbol{v}_j = \lambda_j \boldsymbol{v}_j, \qquad ||\boldsymbol{v}_j|| = 1. \tag{4.7}$$

Then the maximum growth obtainable at time τ, denoted $G(\tau)$, is

$$G(\tau) \equiv \max_{||\boldsymbol{u}'(0)||=1} \frac{E(\tau)}{E(0)} = \max_j \lambda_j. \tag{4.8}$$

Thus the maximum growth is obtained by computing the dominant eigenvalue, and corresponding eigenmode, of $\mathcal{A}^*(\tau)\mathcal{A}(\tau)$. This is again done iteratively through actions of $\mathcal{A}^*(\tau)\mathcal{A}(\tau)$ as discussed in Sec. 4.2.3.

Finding the dominant eigenvalues of $\mathcal{A}^*(\tau)\mathcal{A}(\tau)$ is equivalent to finding the largest singular values of $\mathcal{A}(\tau)$. The eigenmode $\boldsymbol{v}_j$ in Eqn. (4.7) provides an initial perturbation $\boldsymbol{u}'(0)$ which generates a growth λ_j over time τ. Referring to Fig. 4.1, this is the inlet perturbation. Potentially, one is also interested in the evolution of perturbations from $t = 0$ to some large value of t where the perturbation washes out of the system. The evolved perturbation at time τ has a particular meaning however.

Defining $\boldsymbol{u}_j$ to be the normalized perturbation at time τ evolved from initial condition $\boldsymbol{u}'(0) = \boldsymbol{v}_j$, we have

$$\mathcal{A}(\tau)\boldsymbol{v}_j = \sigma_j \boldsymbol{u}_j, \qquad ||\boldsymbol{v}_j|| = ||\boldsymbol{u}_j|| = 1, \tag{4.9}$$

where $\sigma_j = ||\boldsymbol{u}'(\tau)||$. This is nothing other than the leading part for the singular value decomposition of $\mathcal{A}(\tau)$.

When solving the eigenvalue problem, the time horizon, denoted T in this case, is set by practical considerations; the eigenvalues λ_j are independent of T. For the transient growth problem, the eigenvalues of $\mathcal{A}^*(\tau)\mathcal{A}(\tau)$, singular values of $\mathcal{A}(\tau)$, depend on the time horizon, here denoted τ, and this value is a parameter of study — each new τ requires a new solution to Eqn. (4.7). As is the case for linear stability, in the transient growth problem one is primarily interested in the optimal energy growth given by the dominant eigenvalue of $\mathcal{A}^*(\tau)\mathcal{A}(\tau)$ as these describe the 'most dangerous' cases. However, as we show in Sec. 4.3.3 the first few sub-dominant eigenvalues can also be of interest.

The final general point is that the eigenmodes of $\mathcal{A}(\tau)$ and $\mathcal{A}^*(\tau)\mathcal{A}(\tau)$ are trigonometric in the azimuthal direction, of the form $\exp(\mathrm{i}m\theta) + \text{c.c.}$, for integer m. Moreover, eigenmodes with different azimuthal mode numbers m decouple. As a result, m effectively becomes a specified input parameter to the stability or transient growth problem. (See Sec. 4.2.3). Specifically then, the optimal energy growth is a function not only of the time horizon τ as indicated in Eqn. (4.8), but also the control parameter, Re, and the azimuthal mode number m, i.e. $G = G(\tau, Re, m)$. For clarity, the notation used later in this paper will be restricted to only those dependencies relevant to the context.

4.2.3 Further Details

For completeness we present further details of the numerical computations used in this study. We employ a time-stepper approach (Barkley et al. [2008]) in which all problems are solved with the same code base: a spectral/hp element–Fourier discretization of the Navier–Stokes equations (Blackburn and Sherwin [2004]).

A representative computational mesh is shown in Fig. 4.3. The axial–radial plane, (x, r), is discretized using a spectral-element mesh as in Fig. 4.3(a). All meshes used in this study have the same inflow length $L_i = 5$ and the same refinement structure in the vicinity of the expansion. This mesh has been used in previous studies of the planar backward-facing step (Blackburn et al. [2008b]). The outflow length requirements depend on τ and vary from $L_0 = 25$ (as in Fig. 4.3) at small τ up to $L_0 = 75$ at τ=130, the largest considered in this study. The longer meshes differ from that shown only by the continuation of regular downstream elements. The requirements for the inflow and outflow lengths are set by the boundary conditions on the transient growth computations discussed shortly.

Velocity components and the pressure are expanded in a tensor product of order-N polynomials within each element. In the azimuthal direction a Fourier representation with complex modes is used to produce the full three-dimensional physical geometry illustrated in Fig. 4.3(b). A Fourier-mode-dependent set of boundary conditions is imposed at $r = 0$, the centerline of the pipe, as detailed elsewhere (Blackburn and Sherwin [2004]). For linear analyses, azimuthal Fourier modes can be dealt with independently, whereas in direct nonlinear simulations of three-dimensional states, Fourier modes must be dealt with concurrently.

The choice of polynomial order for the spectral-element expansion is dictated by the need to resolve the separated shear layer of the base flow. This can be best

Table 4.1: Streamwise position of base flow reattachment point (in units of step height, h) at Re=1000, as a function of spectral-element polynomial order N. The outflow length is $L_o = 75 = 150h$.

Order, N	x_r/h
3	89.3312
4	89.2565
5	89.2655
6	89.2630
7	89.2623
8	89.2620

assessed by analysis of the reattachment of the separating streamline, since its location depends sensitively on the resolution of the separated shear layer, particularly near the separation point. Table 4.1 shows the dependence of the flow reattachment point, x_r, on polynomial order at Re=1000. A value of $N = 6$ is sufficient to resolve the flow accurately and this value is used for all computations in this study.

Nonlinear solutions consist of two types. First, there are steady, axisymmetric base flows $\boldsymbol{U} = (U_x(x,r), U_r(x,r))$. These are computed by time evolving the two-dimensional (axisymmetric) Navier–Stokes equations with boundary conditions given by Eqns. (4.2) until a steady state is reached. The final flow field is then stored for use with the linear stability analysis and growth computations.

The other types of nonlinear solutions presented are fully three-dimensional, time-dependent flows resulting from small disturbances added to the parabolic inflow. Specifically, the transverse velocity components of the inflow are perturbed by a small amount of Gaussian white noise. The boundary conditions, Eqn. (4.2a), are replaced by

$$\boldsymbol{u}(\partial\Omega_i, t) = 2(1 - 4r^2)\boldsymbol{e}_x + \eta_r \boldsymbol{e}_r + \eta_\theta \boldsymbol{e}_\theta \tag{4.10}$$

where η_r, η_θ are random variables drawn from a Gaussian distribution with zero mean

and standard deviation γ. In most cases we use $\gamma = 10^{-2}$, but also use $\gamma = 2.5 \times 10^{-3}$.

The linear computations (eigenvalues and optimal growth) are based on the time-stepper approach in which the actions of the linear operators $\mathcal{A}$ and $\mathcal{A}^*$ are effected by evolving perturbations in time using a modified version of the same simulation code. This is coupled with standard linear algebra algorithms to obtain the desired eigenvalues and eigenmodes.

Since we work in cylindrical coordinates and the base flows are axisymmetric, the linearized advection operator in Eqns. (4.3)–(4.4) has the following explicit form

$$\boldsymbol{DN} \cdot \boldsymbol{u}' = \left[\begin{pmatrix} \boldsymbol{U} \cdot \nabla & 0 & 0 \\ 0 & \boldsymbol{U} \cdot \nabla & 0 \\ 0 & 0 & \boldsymbol{U} \cdot \nabla \end{pmatrix} + \begin{pmatrix} \partial_x U_x & \partial_r U_x & 0 \\ \partial_x U_r & \partial_r U_r & 0 \\ 0 & 0 & U_r/r \end{pmatrix} \right] \begin{pmatrix} \tilde{u}_x \\ \tilde{u}_r \\ u'_\theta \end{pmatrix}$$

where $\boldsymbol{U} \cdot \nabla = U_x \partial_x + U_r \partial_r$. Thus the only non-zero term resulting from cylindrical coordinates is $U_r u'_\theta / r$. All other terms vanish for the base flows we consider or have Cartesian analogs.

Computing the action of $\mathcal{A}^*(\tau)$, necessary for computing the action of $\mathcal{A}^*(\tau)\mathcal{A}(\tau)$, requires evolving perturbations by equations that are adjoint to Eqns. (4.3). Using integration by parts these adjoint equations are

$$-\partial_t \boldsymbol{u}^* + \boldsymbol{DN}^* \cdot \boldsymbol{u}^* = -\nabla p^* + Re^{-1} \nabla^2 \boldsymbol{u}^* \tag{4.11a}$$

$$\nabla \cdot \boldsymbol{u}^* = 0 \tag{4.11b}$$

where $\boldsymbol{u}^*$ and p^* are the adjoint velocity and pressure fields, respectively. The adjoint

advection terms are

$$\boldsymbol{DN}^* \cdot \boldsymbol{u}^* = \left[\begin{pmatrix} -\boldsymbol{U}\cdot\nabla & 0 & 0 \\ 0 & -\boldsymbol{U}\cdot\nabla & 0 \\ 0 & 0 & -\boldsymbol{U}\cdot\nabla \end{pmatrix} + \begin{pmatrix} \partial_x U_x & \partial_x U_r & 0 \\ \partial_r U_x & \partial_r U_r & 0 \\ 0 & 0 & U_r/r \end{pmatrix} \right] \begin{pmatrix} u_x^* \\ u_r^* \\ u_\theta^* \end{pmatrix}$$

The change of sign from $(\boldsymbol{U}\cdot\nabla)\boldsymbol{u}'$ to $-(\boldsymbol{U}\cdot\nabla)\boldsymbol{u}^*$ follows from one integration by parts, together with the divergence-free condition. The second term is equivalent to a standard matrix transpose. The action of $\mathcal{A}^*(\tau)\mathcal{A}(\tau)$ on a perturbation is obtained by evolving the perturbation forward τ time units under Eqns. (4.3), followed by evolving the perturbation backward τ time units under Eqns. (4.11). This is easy to implement when using the time-stepper approach.

For axisymmetric base flows, the linear operators $\mathcal{A}$ and $\mathcal{A}^*$ are homogeneous in the azimuthal direction and different azimuthal modes decouple. Equations. (4.3) and (4.11) then have invariant subspaces of the form

$$\tilde{u}_x(x,r,\theta,t) = \hat{u}_x^m(x,r,t)\cos(m\theta)$$
$$\tilde{u}_r(x,r,\theta,t) = \hat{u}_r^m(x,r,t)\cos(m\theta)$$
$$u'_\theta(x,r,\theta,t) = \hat{u}_\theta^m(x,r,t)\sin(m\theta)$$
$$p'(x,r,\theta,t) = \hat{p}^m(x,r,t)\cos(m\theta)$$

or similar with any rotation in θ, where m is integer. The time stepping code thus evolves the three velocity components $(\tilde{u}_x, \tilde{u}_r, u'_\theta)$, on a strictly two-dimensional (x,r) spectral-element mesh. The mode number m is an input parameter.

For computing the eigenvalues of $\mathcal{A}(T)$, the inflow boundary condition is homogeneous Dirichlet, and all other boundary conditions are as in Eqns. (4.2). For computing eigenvalues of $\mathcal{A}^*(\tau)\mathcal{A}(\tau)$ we use homogeneous Dirichlet boundary conditions on all boundaries both for the operator $\mathcal{A}(\tau)$ and $\mathcal{A}^*(\tau)$. As discussed elsewhere (Barkley et al. [2008]), for transient growth problems it is essential that the boundaries be sufficiently far upstream and downstream that perturbations do not reach them during the computation of $\mathcal{A}^*(\tau)\mathcal{A}(\tau)$. This requirement dictates the values of L_i and L_o used in this study. We find $L_i = 5$ is sufficient for all cases considered in this study. We vary L_o but verify that it is far downstream of computed perturbations.

Eigenvalues are computed using a modified Arnoldi iteration method (Barkley et al. [2008]). In brief, repeated application of the relevant evolution operator, $\mathcal{A}(T)$ or $\mathcal{A}^*(\tau)\mathcal{A}(\tau)$, to a random starting vector $\boldsymbol{u_0}$ generates a Krylov sequence and subsequently an upper Hessenberg matrix, $\boldsymbol{H}$, which spans a subspace of the image of the operator. After relatively few iterations, the dominant eigenvalues of $\boldsymbol{H}$ converge to the dominant eigenvalues of $\mathcal{A}(T)$ or $\mathcal{A}^*(\tau)\mathcal{A}(\tau)$, thus allowing the important eigenvalues and eigenvectors to be computed at low computational cost and memory requirements.

4.3 Results

4.3.1 Base Flows

We begin with a brief discussion of the steady, axisymmetric base flows. Figure 4.4 shows the streamfunction for a typical case, at Re=600. Streamlines of the high-speed core flow are drawn as dotted lines, while the separation streamline emanating from the expansion edge and the recirculation streamlines are drawn as solid lines. Contour level intervals for the streamfunction in the recirculation region and in the core region are

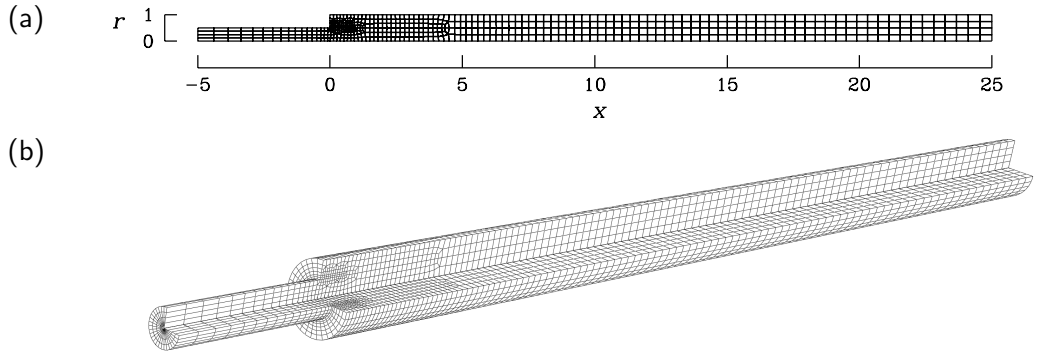

Figure 4.3: A spectral element mesh used in this study. For the case illustrated there are 563 elements, an inflow length of $L_i = 5$ and an outflow length of $L_o = 25$. When required, meshes with more elements and outflow lengths up to $L_o = 75$ have been used. The two-dimensional mesh (a) used for linear analysis is extended to three dimensions (b) for non-linear analysis (DNS) where Fourier expansions are used in azimuth.

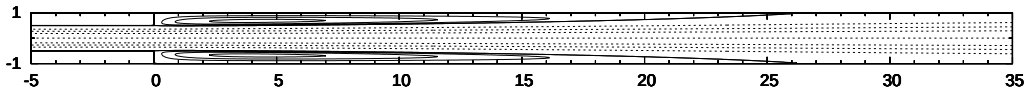

Figure 4.4: Contour plot of the base-flow streamfunction at $Re = 600$, showing the separation and reattachment of the flow, and the recirculation region behind the expansion. Contours are drawn at intervals of 0.125 in the core of the flow, and at intervals of 0.02 in the recirculation region.

distinctly different in order to better illustrate flow structure.

The base flows at all other Reynolds numbers in our study are qualitatively similar, differing primarily in length of the recirculation region. Figure 4.5 shows the relationship between the recirculation length, that is the downstream reattachment point denoted x_r, and Reynolds number for the base flows up to Re=1400. The recirculation length increases linearly with Re according to $x_r/h = 0.0876\,Re$. We believe this to be the most accurate study yet reported of recirculation length for the 1 to 2 expanding pipe. The constant of proportionality we obtain is slightly lower than that of Latornell and Pollard [1986] and Iribarne et al. [1972], who report a linear relationship with a

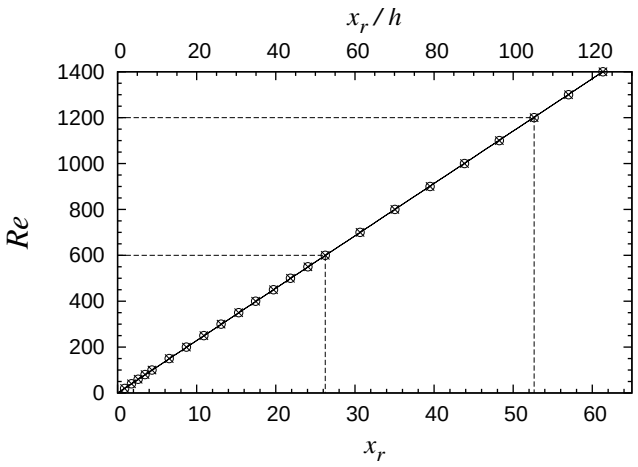

Figure 4.5: Relationship between downstream reattachment point x_r and Reynolds number for base flows with a fully-developed inlet profile up to Re=1400. Points are the computed value of x_r and the solid line shows the best-fit proportionality given by $x_r/h = 0.0876\,Re$. The dotted lines indicate reattachment lengths for the base flows at Re=600 (corresponding to Fig. 4.4) and Re=1200.

proportionality of 0.096 for a fully-developed inlet profile. However, our value matches the more recent experimental observations of Hammad et al. [1999] who reported a value of 0.088.

4.3.2 Linear Stability

For completeness we report in Table 4.2 the leading eigenvalues (those with largest real part) obtained from a linear stability analysis up to Re=1400. At least for Re from 600 to 1400 the leading eigenvalues all correspond to azimuthal modes with m=1 and only these eigenvalues are reported. The eigenvalues reported in Table 4.2 agree with those of Cliffe et al. [To be published] to within 0.3%. In all cases the leading eigenvalues are real and negative, and hence as stated at the outset, the axisymmetric base flow is linearly stable up to Re=1400. In fact Cliffe et al. [To be published] determine that there are no positive eigenvalues to considerably higher Re.

Table 4.2: Leading eigenvalues for linear stability of flows in the 1 to 2 axisymmetric expansion for Reynolds numbers indicated. All values correspond to azimuthal mode number m=1. All are real and negative and hence the axisymmetric base flow is linearly stable up to at least $Re = 1400$.

Re	σ
600	-6.2388×10^{-3}
1000	-2.6827×10^{-3}
1200	-1.9391×10^{-3}
1400	-1.4571×10^{-3}

4.3.3 Transient Energy Growth

Having established that the flow is linearly stable up to at least Re=1400, we turn to the determination of the most dangerous, that is energetic, transient dynamics. Recall that such a study involves not only the Reynolds number, but also the time horizon τ and the azimuthal mode number m. We begin by presenting results as a function of τ and m for a fixed value of Re and subsequently we consider the dependence on Re.

Dependence on azimuthal mode number

Figure 4.6 shows optimal growth envelopes $G(\tau)$ for perturbations in the axisymmetric (m=0) and first six non-axisymmetric modes (m=1 to 6) over a range of time horizons at a fixed Reynolds number of Re=600. In general, the greatest increase in energy is seen in the first azimuthal mode, m=1, which at this Reynolds number peaks at $\tau \simeq 50$, just at the right edge of the figure, and decreases for larger τ. The higher mode numbers exhibit less growth and peak at considerably smaller values of τ. For example, the m=2 growth envelope peaks at $\tau \simeq 19.5$ where the optimal growth there is an order of magnitude less than for the m=1 mode at the same value of τ and 1.5 orders of magnitude less than for the m=1 mode where it obtains its maximum.

There is generally a monotonic decrease in growth with increase in mode number, with two exceptions. The first is that the m=0, axisymmetric, mode growth envelope is qualitatively different from the others and in particular the growth peaks at a much earlier time horizon and has a much smaller value in comparison to any of the low-order, non-axisymmetric modes. The other exception to the dominance of m=1 is at small time horizons. Below $\tau \simeq 3$ the m=2 mode exhibits larger optimal growth than the m=1 mode, and below $\tau \simeq 2$ the m=3 mode exhibits larger optimal growth than the m=2 mode. This can be clearly seen in Fig. 4.6(b). We have not attempted to resolve the details and mode ordering at yet smaller values of τ. This modal behavior, where the m=1 mode dominates except for short time horizons, has also been reported for flows in parallel (Bergström [1993]; Schmid and Henningson [1994]) and constricted (Blackburn et al. [2008b]) pipes.

The dominance of the energy growth for the m=1 mode is observed at all other Reynolds numbers in our study. Hence, for the remainder of the chapter we shall mainly focus on the m=1 case. Some results will also be presented for the m=0 case since it is qualitatively different from the others and because it represents the strictly two-dimensional problem.

Reynolds number and time horizon

The dependence of the optimal growth on Reynolds number and time horizon is well summarized by contour plots of $G(\tau, Re)$. Figures 4.7(a) and (b) show such contour plots for m=1 and m=0 modes, respectively. Only contours with $G \geq 1$ are plotted and the no-growth contours, corresponding to $G = 1$, are emphasized by the thicker black curves. To the right of the no-growth contours G is less than unity, meaning that the energy of any perturbation will be less than its initial energy at these values of τ.

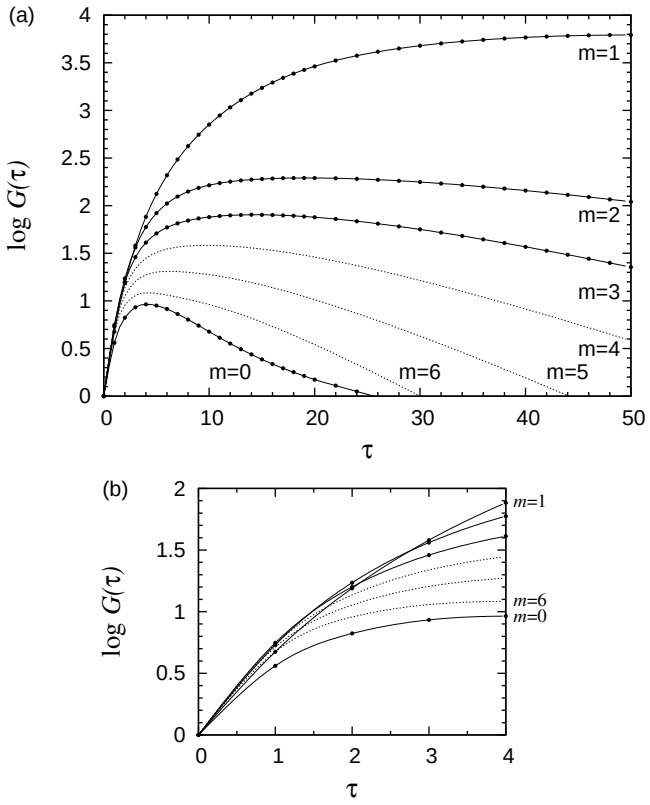

Figure 4.6: (a) Energy growth envelopes at Re=600 for azimuthal mode numbers (as indicated) up to m=6. (b) Enlargement of (a) for small τ. Curves for $m = 1$ through $m = 6$ are in decreasing monotonic order on the right-hand side.

Table 4.3: Table of critical Reynolds numbers, Re_m^c, maximum growth values $G_m^{\max}$ and corresponding time horizons for maximum growth, $\tau_m^{\max}$ (for Re=600 and Re=1200 as indicated) for each of the first four azimuthal modes, m.

m	Re_m^c	$G_m^{\max}(600)$	$\tau_m^{\max}(600)$	$G_m^{\max}(1200)$	$\tau_m^{\max}(1200)$
0	64	9.20×10^0	4.4	2.32×10^1	6.2
1	26	6.23×10^3	50.1	3.77×10^6	106
2	38	1.95×10^2	19.5	7.59×10^2	34.1
3	54	8.05×10^1	14.6	3.17×10^2	28.3

The intersection of the no-growth contour with the Reynolds number axis is a saddle-point of the growth function in the $\tau - Re$ plane and indicates a critical Reynolds number, Re^c, above which energy growth is possible. This critical value depends on mode number m and so we define Re_m^c as the value of Re for which

$$\left.\frac{\partial G(\tau, Re_m^c)}{\partial \tau}\right|_{\tau=0} = 0.$$

For $Re > Re_m^c$, the growth envelope $G(\tau)$ for mode number m has positive slope at τ=0 and so $G(\tau) > 1$ for a least some values of τ. The smallest critical value occurs for m=1 with $Re_1^c = 26$. Values of Re_m^c for other m are also quite low and given in the second column of Table 4.3.

As the Reynolds number increases perturbations with m=1 azimuthal structure can be amplified by large factors. Specifically, one can see in Fig. 4.7(a) that at Re=1200, perturbations are amplified by factors of over 10^6. Thus, even though the flow is linearly stable at Re=1200, it is capable of amplifying small perturbations to appreciable levels through strictly linear growth. In contrast to the m=1 modes, axisymmetric modes of Fig. 4.7(b) experience very limited growth and are confined to much shorter time horizons for all Re studied.

(a)

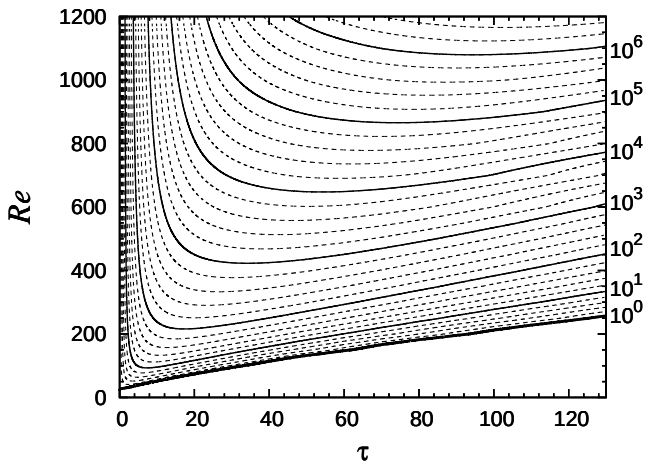

(b)

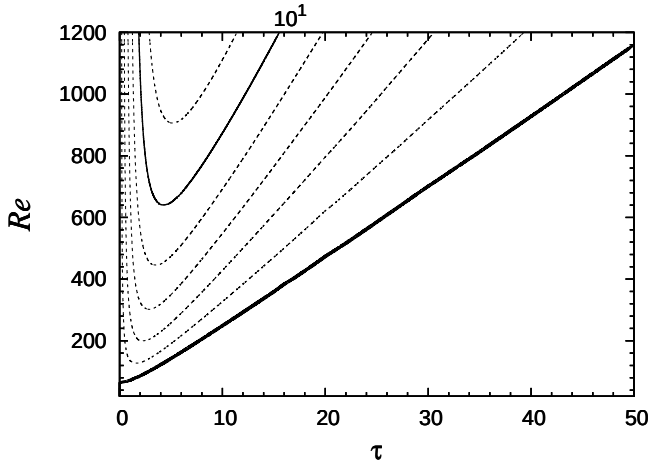

Figure 4.7: Contours of optimal transient energy growth as a function of time horizon, τ, and Reynolds number for (a) azimuthal mode number m=1 and (b) azimuthal mode number m=0.

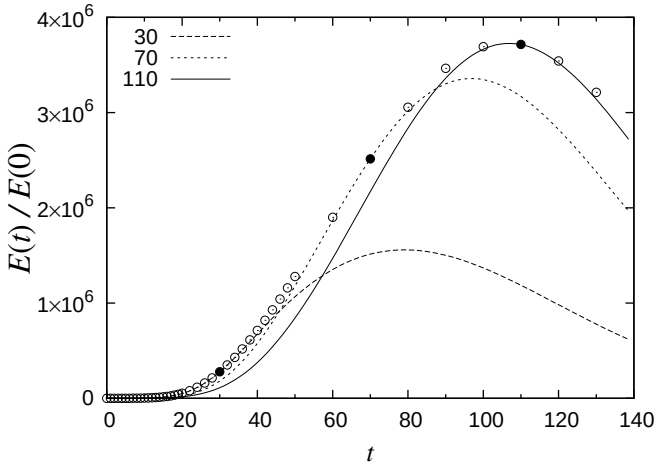

Figure 4.8: Energy growth under linear evolution at Re=1200, m=1 for three different initial conditions corresponding to optimal perturbations at τ=30, 70 and 110. Circles denote the optimal growth envelope. Each linear evolution curve touches the envelope at its respective τ value, as indicated by a filled circle.

Time evolution of optimal perturbations

We now consider the time evolution of some optimal perturbations at Re=1200. Figure 4.8 shows the optimal growth envelope for Re=1200 and m=1, along with the transient energy evolution under the linearized Navier–Stokes equations from three different initial conditions. The initial perturbations are the computed optimal perturbations for three different values of τ as indicated. The case τ=110 is very nearly the initial condition giving the maximal energy growth at Re=1200. As is necessarily the case, each of these transient evolution curves touches the optimal growth envelope at its corresponding τ value, but otherwise they lie entirely below the envelope.

Figure 4.9 depicts the perturbation field evolving from the optimal initial condition for τ=110, (Re=1200, m=1). This evolution corresponds to the transient energy trajectory drawn with a solid line in Fig. 4.8. Owing to the small magnitude of the initial perturbation relative to its evolved state, we visualize the perturbation at early times

differently from later times. Initially the perturbation is shown via a contour plot of the azimuthal velocity component u_θ in a planar cut through the geometry. Subsequent fields are visualized in terms of three-dimensional isosurfaces of azimuthal velocity. The evolving perturbation is plotted on a relatively small section of the computational domain every four time units until time 28. The perturbation is also plotted when it attains its maximum energy, at t=110. At this time the perturbation is well downstream of the expansion: the centroid of the perturbation energy lies at $x_c = 47.1$.

Unsurprisingly, the optimal initial perturbation is concentrated near the flow separation at the expansion from where it is subsequently advected by the base flow into the separated shear layer. In passing over the shear layer, chevron structures emerge in a packet, initially of very limited streamwise extent. After an initial rapid growth phase, the structure stabilizes as it approaches the time of peak growth after which the vortices at the rear of the structure begin to decay. The anti-symmetric appearance of the perturbation is a direct consequence of the m=1 azimuthal structure. Note that there is a characteristic axial wavelength of the disturbance that is approximately preserved through the transient growth.

Transient behaviour of the optimal perturbation in m=0 at Re=1200 is illustrated through isosurfaces of radial velocity in Fig. 4.10. The initial disturbance is again concentrated around the step edge. Shortly afterwards it evolves into a set of toroidal rolls of alternating sign which advect downstream, first growing in energy up to $t \approx 6$, then decaying. Again note that the axial wavelength of the disturbance is preserved through this transient behaviour.

The physical nature of the perturbed shear layer for Re=1200, m=1 is illustrated in Fig. 4.11. The optimal perturbation at time of maximum energy growth is linearly combined with the base flow at a relative energy level of 5%. This combined state is

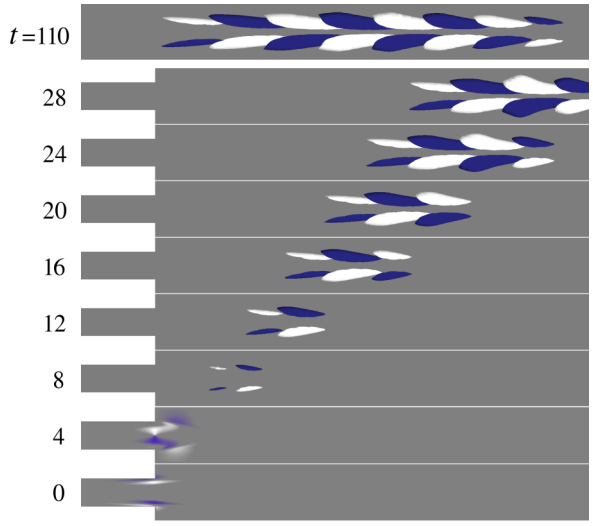

Figure 4.9: Evolution of optimal initial disturbance in the m=1 mode visualized through contours/isosurfaces of azimuthal velocity at Re=1200 from $t = 0$ (bottom) in time intervals of four units in the spatial range $-2.5 \leq x \leq 15$. The top figure shows the evolved disturbance at its maximum growth. The spatial range is $36.5 \leq x \leq 54$ and the isosurface levels two orders of magnitude larger than in the lower part of the figure.

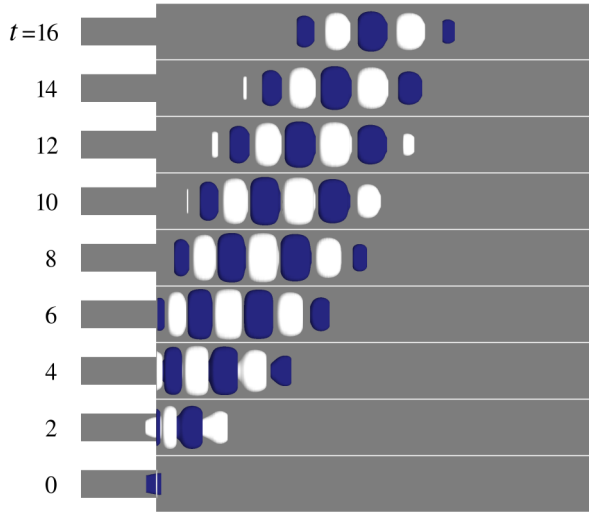

Figure 4.10: Evolution of optimal initial disturbance in the m=0 mode visualized through isosurfaces of radial velocity at Re=1200 from $t = 0$ (bottom) in time intervals of two units in the spatial range $x \in [-2.5, 15]$.

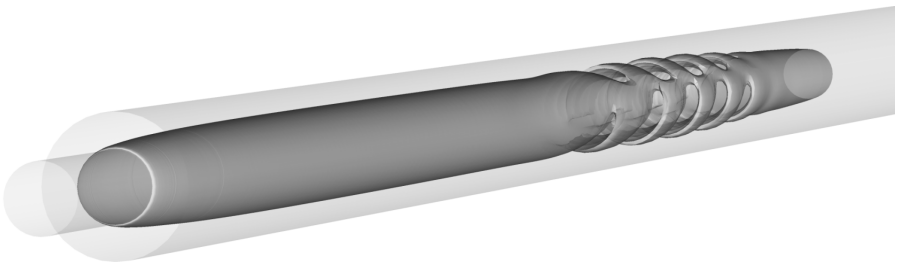

Figure 4.11: Physical interpretation of the maximal disturbance at Re=1200. Shown is a linear superposition of the base flow with the optimal m=1 disturbance at the time of maximum growth, t=110. The disturbance has a relative energy magnitude of 5% compared to the base flow. The visualization is a semi-transparent isosurface of azimuthal vorticity at a level highlighting the separated shear layer.

visualized via an isosurface of azimuthal vorticity. The image suggests that the optimal perturbation manifests as a sinuous oscillation of the shear layer, as was also observed in the optimal growth analysis of flow in a stenotic pipe (Blackburn et al. [2008b]). Note that the azimuthal orientation is arbitrary, due to rotational symmetry of the flow, and has been chosen here so as to emphasize the structure of the surface.

Growth maxima

At a given Reynolds number, and for a specified azimuthal mode number m, the maximum of G over all time horizons τ is an important quantity. We thus define the maximum growth and the corresponding time horizon as

$$G_m^{\max}(Re) = \max_{\tau} G(\tau, Re, m),$$

$$\tau_m^{\max}(Re) = \arg\max_{\tau} G(\tau, Re, m).$$

Table 4.3 includes the maximum growth and corresponding time horizons at representative Reynolds numbers of 600 and 1200.

The growth maxima are plotted in Fig. 4.12 as a function of Re for several values

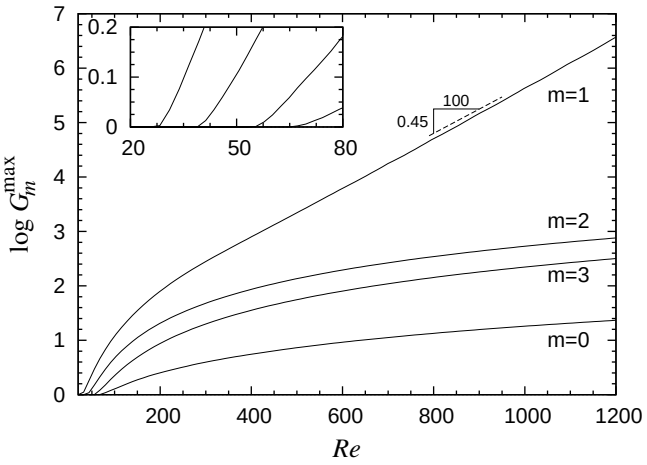

Figure 4.12: Optimal energy growth, $G_m^{\max}$, as a function of Re for each of the first four azimuthal modes. Above $Re \approx 300$, $G_1^{\max}$ increases exponentially with Reynolds number at a rate of 0.45 orders of magnitude for each increase of 100 in Re. Inset shows detail at small Re. Curves intersect $\log G_m^{\max} = 0$ at the critical Reynolds number Re_m^c of each mode m.

of m. Each curve emerges at the corresponding critical value Re_m^c. The figure highlights the significantly different magnitude of growth obtainable for m=1 perturbations compared with perturbations in other azimuthal mode numbers, particularly axisymmetric perturbations.

Beyond approximately Re=300, $\log G_1^{\max}(Re)$ is seen to be linear with Re indicating an exponential dependence of maximal growth on Reynolds number. This may also ultimately be true of the other broken symmetry perturbations at Reynolds numbers higher than those studied here. Similar exponential growth with Reynolds number has been observed for two other separated flows: flow over a backward-facing step (Blackburn et al. [2008a]) and steady flow in a stenotic pipe (Blackburn et al. [2008b]). This exponential dependence is significantly different from the classic parallel flows, planar Couette flow (Reddy and Henningson [1993]) and straight pipe flow (Bergström [1993]; Reddy and Henningson [1993]), for which the maximum transient growth increases only with the square of Reynolds number.

The form of evolved optimal perturbations at the time of maximal growth, $\tau_m^{\max}$, are expected to provide a good indication of what might be observed in a flow subject to small perturbations. See for example the perturbation at $t = 110$ in Fig. 4.9 and the combined state shown in Fig. 4.11. We shall address this in Sec. 4.3.4 where we consider nonlinear simulations. Here we list in Table 4.4 some pertinent characteristics of the optimal perturbation fields at the point of maximum growth for the case of m=1. For each Re, $\tau_m^{\max}$ is given, along with the centroid location (x_c, r_c) of the energy of the evolved perturbation, as well as the local axial wavelength λ_x and temporal frequency *St* of the perturbation. The wavelength of the evolved perturbation decreases slightly with Reynolds number, while the temporal frequency is essentially independent of Reynolds number. The non-zero radial location r_c is a consequence of the fact that the centroid is calculated from a Fourier mode, in the meridional semi-plane, and it represents the radial location where the disturbance is largest (if the energy centroid were calculated in physical space then r_c would be zero).

Fig. 4.13 shows x_c, the axial location of the perturbation energy centroid at maximal growth, together with the reattachment point of the base flow previously plotted in Fig. 4.5. One sees clearly that for $Re \gtrsim 500$ the optimal disturbance at its peak energy growth lies consistently about five diameters (10 step heights) upstream of the reattachment point of the base flow. This provides strong evidence that the separated shear layer is driving the growth of perturbations.

Suboptimal growth

The optimal perturbations considered thus far are those which provide the maximum transient energy growth under linear evolution. However suboptimal perturbations can attain comparable energy, with the first sub-dominant perturbations in particular demon-

Table 4.4: Characteristics of the optimal perturbations at the time of maximum growth, $\tau^{\max}$, for m=1 modes at Reynolds numbers indicated. Along with $\tau^{\max}$ the centroid location (x_c, r_c) of the evolved perturbation energy, as well as the local axial wavelength λ_x and temporal frequency St of the perturbation.

Re	$\tau^{\max}$	x_c	r_c	λ_x	St
600	50.1	21.3	0.40	3.79	0.175
800	69.0	29.9	0.40	3.62	0.165
1000	87.6	38.5	0.40	3.62	0.155
1200	106	47.1	0.40	3.68	0.158

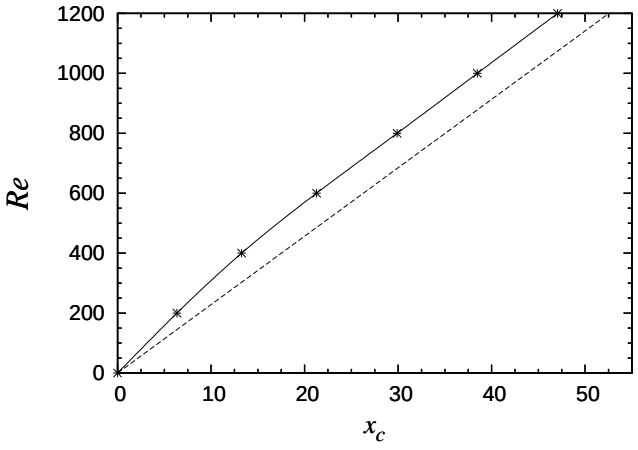

Figure 4.13: Location of the centroid of the disturbance at its maximum growth (points connect by solid lines), compared with the location of the reattachment point (dashed line). The disturbance reaches its maximum approximately 5 diameters upstream of reattachment point.

strating growth on the same order of magnitude as the optimal perturbations. We have calculated suboptimal perturbations, and corresponding energy growth factors, by computing the subdominant eigenvalues and eigenmode of $\mathcal{A}^*(\tau)\mathcal{A}(\tau)$ in Eqn. (4.7) by the Arnoldi method as described in Sec. 4.2.3

In Fig. 4.14 we show growth envelopes for the optimal and first three suboptimal perturbations at Re=600. A few additional suboptimal growth factors are plotted at $\tau = 50$. It is apparent that the growth envelopes are grouped in pairs. The first subdominant curve is very similar to the optimal envelope – it attains its growth maximum at nearly the same value of τ and with 80% the energy amplification of the optimal. Each of the second pair of suboptimal growth envelopes peaks at an earlier time horizon than for the first pair suggesting the eigenmodes undergo slightly different dynamics. These modes obtain about 30% of the optimal energy growth. The first eight leading eigenmodes at $\tau = 50$ indicates further pairing of modes. We have not resolved details of suboptimal dynamics further into the spectrum.

The perturbation fields themselves provide valuable insight into the pairing of growth envelopes. The azimuthal velocity of the four leading modes at $\tau = 50$ are visualized in Fig. 4.14. These fields have been obtained by evolving each (sub)optimal initial condition, each with the same energy norm, to time $t = 50$. Referring to Eqn. (4.9), these are the first four left singular vectors of $\mathcal{A}(50)$ multiplied by the corresponding singular value. The isosurface levels are the same for all four modes.

The pairing of the eigenvalues is immediately apparent: the corresponding optimal modes come in pairs that are primarily related by a phase shift of $\pi/2$ relative to one another. This has been previously observed and discussed in the context of the planar backward-facing step (Blackburn et al. [2008a]). For a truly streamwise invariant flow, such as for a straight pipe, the optimal modes necessarily come in pairs exactly related

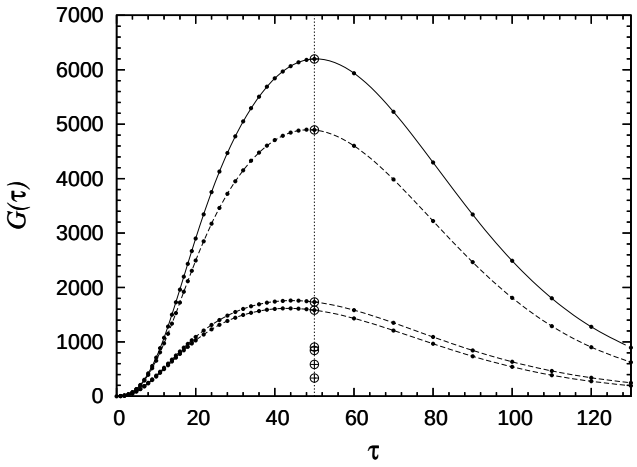

Figure 4.14: Leading four growth envelopes for the optimal and suboptimal perturbations for the m=1 mode at Re=600. The circles on the dotted line at τ=50 show the first eight leading eigenvalues at the point of the peak optimal growth.

by a $\pi/2$ phase shift since the modes are trigonometric in the streamwise direction (sine and cosine pairs). Essentially, the expansion can be viewed as a breaking of streamwise translation symmetry of the flow. The breaking is very significant for the base flow since it gives rise to the separated shear layer which dominates the flow in the expanding pipe. However, the optimal perturbations see a flow with only a relatively weak broken streamwise symmetry and hence come in pairs with only slightly different dynamics and growth rates.

4.3.4 Response to Noise

To demonstrate the relevance of the linear growth computations to a real flow in the presence of small inlet noise, we have performed a limited number of full, three-dimensional direct numerical simulations with weak noise imposed on the inflow as described in Sec. 4.2.3. For each simulation, the initial state is the steady laminar flow at the given Reynolds number. Starting at time zero, noisy inflow boundary conditions are imposed.

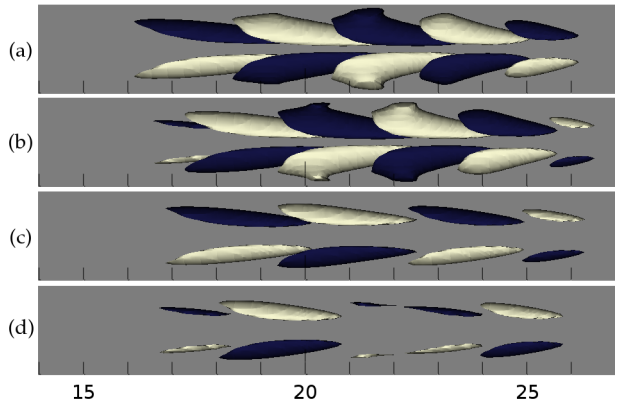

Figure 4.15: Iso-surfaces of azimuthal velocity for the four leading perturbations at Re=600, m=1 evolved to time $t = 50$. (a) and (b) are the optimal and first sub-optimal modes. (c) and (d) are the next pair of sub-optimal modes. (See Fig. 4.14.)

In the first instance, we analyze the dynamics of the flow in terms of the modal energies over the full domain defined by

$$E_m(t) = \frac{1}{2}\int_\Omega ||\hat{\boldsymbol{u}}^m(t)||^2 \tag{4.12}$$

where $\hat{\boldsymbol{u}}^m$ is the m^{th} component of the azimuthal Fourier transformed velocity field. Figure 4.16 shows the evolution of modal energies at three values of Re. The axisymmetric component of the energy, E_0, is larger than all others and is off the scale of the figure. It starts at, and remains essentially unchanged from, the energy of the steady base flow.

In all cases, the energy of the m=1 mode grows within a short time as the effect of the noisy inflow condition propagates through the domain. For Re=600, the m=1 modal energy saturates above the noise floor of all other modes. It is nevertheless quite small. At Re=900, the m=1 modal energy saturates at 500 times the level of the noise floor. The m=2 modal energy is just barely distinguishable above the higher modes. At Re=1200, the first three modes are clearly visible with the m=1 modal energy more than four orders of magnitude above the noise floor and approximately one

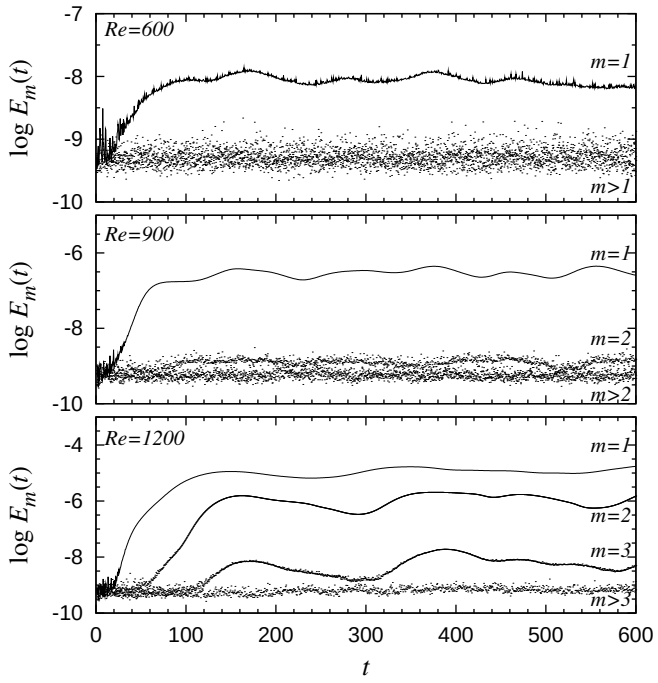

Figure 4.16: Modal energy in a noisy inflow DNS of the expanding pipe flow at (a) Re=600, (b) Re=900, and (c) Re=1200. Modal energies visible above the noise floor of 10^{-9} are labeled. Initially the flow is the steady axisymmetric base flow. The axisymmetric energy E_0 is off the scale of the figure.

order of magnitude above the m=2 mode. Some long period ($T \simeq 200$) dynamics may be present in the noise-driven flow at Re=1200, but we have not investigated these as they are outside the focus of our study.

The modal energies shown in Fig. 4.16 clearly confirm the dominant response of the m=1 mode as determined by the optimal growth analysis. Moreover, for the Reynolds numbers examined, the saturation value of the m=1 energy E_1 is consistent with exponential dependence on Re with half an order of magnitude for each Re increase of 100. This compares very favorably with the dependence of G_1^{max} on Re in Fig. 4.12.

Having established that a weak noisy inflow does in fact preferentially excite the m=1 mode, we proceed to examine the nature of the resulting flow. Figure 4.17 shows

the optimal linear mode at Re=900 [Fig. 4.17(a)] and Re=1200 [Fig. 4.17(b)], together with instantaneous snapshots of the noise-driven flow at the corresponding Reynolds numbers. Specifically, the top half of each sub-figure shows the optimal perturbation, corresponding to m=1, at the optimal time τ^{max}. Energy of the perturbation field is visualized. The bottom half of each sub-figure shows the three-dimensional flow at a representative time instant. The time is arbitrary except that it is chosen so that the phase of the nonlinear flow aligns with the phase of the optimal mode. For the nonlinear flow the axisymmetric modal energy (which dominates the flow) is removed and the energy in the remaining three-dimensional field is visualized in a semi-meridional plane (lower half of the pipe). Figure 4.18 further highlights the structure of nonlinear flow seen in Fig. 4.17(b) with contour plots of the three velocity components.

The most striking feature of the noise-driven nonlinear flow is that it exhibits precisely the same chevron structures as predicted by the transient growth analysis. The wavelengths of the fully nonlinear flow and the optimal perturbation are almost exactly the same. Moreover, while the structures in the noise-driven flow occupy a greater streamwise extent than the optimal perturbation, the location of the maximum in the nonlinear flow is well aligned with the location of the optimal. As the Reynolds number increases and the location of the optimum moves downstream, so does the location of the nonlinear maximum. There is one final interesting feature of the nonlinear state. Due to the rotational symmetry of the geometry, the m=1 structures may have any orientation in θ. Thus in the noise-driven flow the orientation of the chevron structures is not fixed but can, and does, vary in both space (seen in Fig. 4.18) and time.

The noise-driven nonlinear flow is time varying and depends on the noise level imposed at the inflow. We address these aspects briefly in Fig. 4.19. In Figs. 4.19(a)-(c) we capture the instantaneous state of the nonlinear flow at Re=900 at three times

Figure 4.17: Visualisation of noise-driven flow and optimal perturbation at (a) Re=900, and (b) Re=1200, in the range $10 < x < 65$. The upper half of each pipe shows the m=1 optimal perturbation at the respective Reynolds number, evolved to the point of maximum growth. The lower half shows a snapshot of the noise-driven flow for comparison.

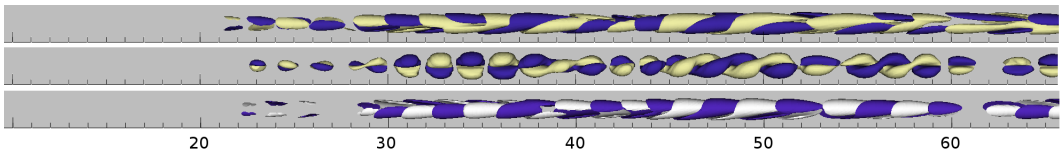

Figure 4.18: Isosurfaces of streamwise (top), radial (middle) and azimuthal (bottom) velocity components for the noise-driven flow showing the downstream disturbance induced by the stochastic forcing at the same time instant as Fig. 4.17(b).

separated by 50 time units. The first plot, Fig. 4.19(a), is at the same time instant as Fig. 4.17(a). In this figure we plot kinetic energy as a function of x sampled along two rays down the length of the pipe. Both rays are at $r = 0.8$. One (solid) is at $\theta = 0$ and the other (dashed) is at $\theta = \pi/2$. Since the flow at Re=900 is dominated by m=1, it is sufficient to use only these two rays to sample the azimuthal structure of the flow. These kinetic energy profiles give a good representation of the instantaneous flow structures. Occasionally the nonlinear flow is relatively quiescent [as in Fig. 4.19(b)] and as can be seen in comparing Fig. 4.19(a) with Fig. 4.19(c), when structures are visible, their strength and location within the pipe vary to some extent.

For the same inlet noise, the structures occupy a much larger streamwise extent at Re=1200, Fig. 4.19(d), and they tend to be located further downstream. By reducing the noise level of the input at Re=1200, the nonlinear state becomes more purely m=1 and the nonlinear structures tend to be more localized and shown in Fig. 4.19(e).

A profile comparison of the standard deviation of velocity components from

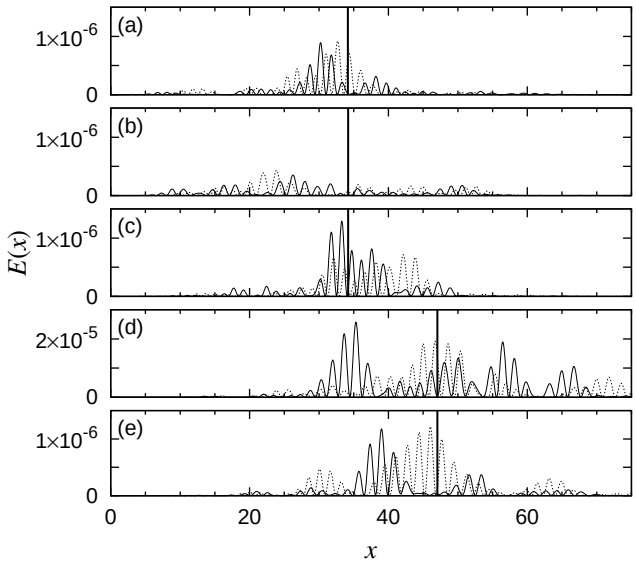

Figure 4.19: Energy of noise-driven flow through the line $r = 0.8$ for the $\theta = 0$ (solid lines) and $\theta = \pi/2$ (dotted lines). (a)-(c) Re=900, (d) Re=1200, (e) Re=1200 at $1/4$ the noise level of (d). Vertical lines indicate x_c, the centroid of the optimal linear perturbation at the corresponding value of Re.

the linear analysis and the noisy simulation is given in Fig. 4.20. The profiles for the noise-driven flow were obtained through temporal-azimuthal averaging of the flow and extracted through a radial line at x=100.0, while the linear profiles were attained through a streamwise averaging of the disturbance profile at its maximal evolution. The streamwise and radial profiles correlate to a high degree. The broader shape of the azimuthal profile from the noise-driven flow is probably due to the contribution of other modes in the system.

Finally, we have extracted important statistical properties of the flow with stochastic forcing. The frequency of the noise-driven flows are $St \approx 0.16$, in agreement with the optimal perturbations in Table. 4.4, but cannot be determined to better than two digits of accuracy. There are similar limitations on the wavelengths of the noise-driven flow and our opinion is that the visual comparison in Fig. 4.17 is probably more reliable. The

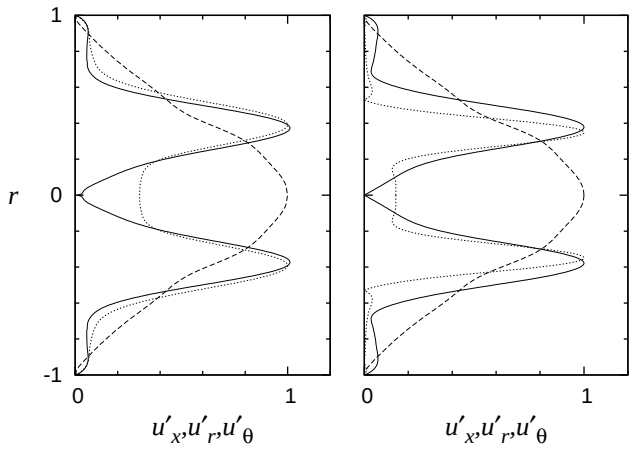

Figure 4.20: Radial profiles of velocity component standard deviations comparing the noise-driven simulation (left) with the linear analysis (right). The three velocity components, each normalized to their peak value, are shown: streamwise (solid line), radial velocity (dashed line) and azimuthal velocity (dotted line).

centroids of the turbulent kinetic energy match those of the optimal perturbations to a reasonable degree in the streamwise direction, while matching almost exactly in cross-stream position. Note that when comparing the centroid of the linear Fourier mode to that of the present noise-driven simulations, we use the centroid of a two-dimensional azimuthal-average of the turbulent kinetic energy.

4.4 Summary and Discussion

We have presented a numerical study of transient dynamics in an axisymmetric expanding pipe. As an important aside, we have first independently confirmed that the steady axisymmetric flow is indeed linearly stable up to Re=1400. We find that nevertheless at linear order perturbations are very strongly amplified in the region of the separated shear layer that extends downstream of the expansion. For example, at Re=1200 the energy of perturbations can be amplified by a factor of over 10^6. The initial disturbances

giving maximal transient growth are localized in the vicinity of the pipe expansion and have azimuthal mode number m=1. Under linear evolution, these disturbances quickly evolve into packets of waves characterized by a chevron structure corresponding to a sinuous oscillation of the shear layer. These disturbances gain energy through an inflectional instability mechanism as they pass along the shear layer, reaching energetic maxima just upstream of the reattachment point of the flow. Thereafter, disturbances advect downstream where they ultimately decay in the stable downstream pipe. Through direct numerical simulations we have established that the linear results do capture, quantitatively, most features seen in a fully three-dimensional nonlinear flow subjected to small Gaussian inlet noise. Thus we have not only quantified in detail the transient response of this flow but we have also demonstrated the importance of this type of linear analysis to flows that would commonly be described as convectively unstable, and thus noise amplifiers.

The expanding pipe flow shares many properties with other documented geometries, although there are also some important differences. The most similar example to the present one is found in a recent study of transient growth of disturbances to steady and pulsatile flows in a pipe with a smooth axisymmetric constriction (Blackburn et al. [2008b]). Such flows have been the subject of extensive research (Griffith et al. [2008]; Vétel et al. [2008]; Varghese et al. [2007]; Sherwin and Blackburn [2005]; Bertolotti et al. [2001]) owing to the importance of the associated flows through arterial stenoses. The two other closely related flows are the planar backward-facing step(Kaiktsis et al. [1996]; Blackburn et al. [2008a]) and the curved channel flow (Marquet et al. [2008b]).

Probably the most significant similarity amongst all these separated flows is the dependence of growth rate on Reynolds number. In all cases, beyond some value of Re, the maximal growth $G^{\max}$ depends exponentially on Re. This exponential dependence

is in stark contrast to parallel shear flows, such as straight pipes and channels, in which the maximum growth typically scales only as the square of Reynolds number (Bergström [1993]; Schmid and Henningson [1994]; Reddy and Henningson [1993]). This highlights the very important difference between the transient growth studied here and that discussed extensively in parallel shear flows (Schmid and Henningson [2001]). Here the transient growth is closely linked to the variation of the flow in the streamwise direction, as illustrated in Fig. 4.1. Physically, perturbations grow rapidly in the region of the shear layer driven by the inflectional velocity profile, but this growth is only transient because perturbations advect past the reattachment point and thereafter decay. Chomaz refers to convective non-normality (Chomaz [2005]) to distinguish these cases from the lift-up non-normality driving transient growth in parallel shear flows. See also Marquet et al. [2008a].

The exponents for different separated flows can be compared. In the present study, Fig. 4.12, $G^{\max}$ for the m=1 azimuthal mode increase at a rate of 0.45 orders of magnitude for each increase of 100 in Re. For convience in this discussion we denote this rate as $\alpha = 0.45/100$. In the study of stenotic flow (Blackburn et al. [2008b]) the rate is not explicitly reported but is obtainable from the available data. The rate is $\alpha = 1.23/100$. However, for the stenotic flow Re is based on the flow upstream of the stenosis. For comparison with the present work, the stenotic flow Re should be corrected upwards by a factor of 2 to account for the local Re at the stenosis. This gives a rate of increase of $G^{\max}$, again for the m=1 azimuthal mode, of $\alpha = 0.61/100$, quite close to that of the sudden axisymmetric expansion. In the study of the planar backward-facing step (Blackburn et al. [2008a]) the rate is stated explicitly giving $\alpha = 1.18/100$. This is the growth rate for strictly two-dimensional modes, but for the planar case three-dimensional effects are not very important. The Re for the backward-facing step is based

on the centerline velocity. Correcting this downwards by a factor of $2/3$ to convert to bulk velocity, $G^{\max}$ for the backward-facing step increases at a rate of $\alpha = 1.77/100$. This is faster than for the axisymmetric flows, but it is not altogether different.

Another point of comparison between the different separated flows is the downstream location of the optimal perturbation when it reaches its maximum growth. In all reported cases this downstream location grows linearly with Re. In the present study we find this location to be consistently 5 inlet diameters upstream of the reattachment point. In the steady stenotic case the location is consistently slightly downstream of the reattachment point, although not far from it. These findings are all consistent with the picture of a shear layer driven instability. Interestingly, this is very different from the case of the planar backward-facing step in which the optimal perturbation is well downstream of all separation and reattachment points when it reaches its maximum growth. However, in the curved channel (Marquet et al. [2008b]), the perturbation is located in the vicinity of the reattachment point at its growth maximum.

One can also consider the form of the optimal perturbations in different cases. Again, not surprisingly, the optimal modes found in the sudden expansion studied here are very similar to the optimal modes in the steady stenotic flow. In both cases the optimal perturbations have m=1 azimuthal structure and visually are nearly the same. (Compare Fig. 4.10 with Fig. 5 of Blackburn et al. [2008b].) On a more quantitative level one can compare the wavelengths in the two cases. From Table 4.4, at Re=800 the wavelength of the optimal disturbance at its maximal location is $\lambda = 3.79$. For the stenotic flow (in terms of equivalent Reynolds numbers and length scales) the wavelength is $\lambda = 3.7$. Taking into account the variation of wavelengths with Re and the fact that the conversion from the stenotic Reynolds number to the present one is not exact, these values are quite close. In any case, these wavelengths are significantly longer than

those observed in the planar backward-facing step (Blackburn et al. [2008a]) and curved channel flow (Marquet et al. [2008b]), in which the optimal modes have a roll structure whose wavelength is typically twice the outflow channel height.

One can likewise consider the Strouhal frequencies observed in various cases. Instead of attempting a detailed comparison, we take a slightly different approach following closely the discussion by Marquet et al. [2008b]. Noting that the perturbations are essentially packets of traveling waves, one can invoke the kinematic relationship $c = \lambda St$, equivalently $St = c/\lambda$, between the speed of a packet c, the wavelength, and the frequency. In the present study the bulk velocity in downstream pipe is $1/4$ due to the 1 to 4 increase in cross-sectional area. Perturbations traveling at the bulk speed with typical wavelength, $\lambda = 3.6$ say at Re=1000, would be expected to have frequency $St = c/\lambda = 0.25/3.6 = 0.07$. With an upper bound set by the bulk velocity in the upstream pipe, we have $0.07 \leq St \leq 0.3$, which encompasses the observed frequencies. Marquet et al. [2008b] argue the same holds for the planar backward-facing step and the curved channel. In all cases the Strouhal frequencies are of comparable magnitude $St \sim 10^{-1}$; differences between the velocity scales in the different configurations hinders a more precise comparison.

Given that the dominant mechanism driving the growth of perturbations is surely inflectional instability of the shear layer, one could attempt to determine the frequency of growing perturbations from a local analysis of the numerically computed shear layer. This has been attempted for the backward-facing step and is further discussed by Marquet et al. [2008b]. Basically the difficulty is that, even ignoring that the flow is not parallel, the frequency determined from a local analysis depends on the station at which the analysis is done and only the order of magnitude of the frequency is reliably determined. In reality the flow is far from parallel in the vicinity of the separation point and likewise

the dynamics of perturbations is initially quite complex. See for example Fig. 4.9 at time $t = 4$.

We conclude with a brief discussion of related experiments. Our measurements of recirculation length give a linear dependence on Re according to $x_r/h = 0.0876\,Re$. This can be considered to be a perfect match to the proportionality 0.088 reported in experiments by Hammad et al. [1999]. The connection between our computations and experiments with regard to the shear-layer oscillations is less satisfying at present. While there are several mentions of shear-layer oscillations in the experimental literature on the 1 to 2 expanding pipe, quantitative details are lacking. Typically oscillations are associated with the breakdown of the linear scaling of the recirculation length with Reynolds number (Back and Roschke [1972]; Iribarne et al. [1972]; Feuerstein et al. [1975]) and there is no agreed value of the Reynolds number at which this occurs (Latornell and Pollard [1986]). We believe that this is due to the fact that there is no linear instability to define such a threshold for oscillation and the onset of oscillations detectable in experiment will depend on factors such as the level of noise in the experiment. Oscillations observed in some experiments, for example by Sreenivasan and Strykowski [1983] and Mullin et al. [2009], are clearly of a very different character than the waves examined here. The oscillations found in these experiments have a much lower frequency, by more than an order of magnitude, than ours and are observed at Re above 1500.

There are two possible points of contact between calculations presented here and published experiments. The first is the work of Latornell and Pollard [1986] on the expanding pipe. They report small sinusoidal waves appearing in the shear layer. At Re=750 these are observed to start at approximately 20 inlet diameters downstream of the expansion, which is consistent with our optimal growth results from Table 4.4. The other is the work of Griffith et al. [2008] on flow in a stenotic geometry. They

report shear-layer oscillations and in fact associate these with convective instability. Moreover, for a blockage of 0.75 (corresponding to a 1 to 2 expansion following the stenosis), they measure nondimensional oscillation periods roughly in the range of 0.2 to 0.3 for Reynolds numbers in the range 400 to 800. Converting to expanding pipe units, this gives Strouhal frequencies in the range 0.4 to 0.6 for Re between 800 and 1600. Although larger, these frequencies are of the same magnitude as those we obtain. Differences between the geometries could account for the discrepancy.

We hope that the detailed results presented here will motivate experimentalists to look quantitatively at these transient dynamics in the future.

Chapter 5

Global Approach to Convective Instability in Flow past a Circular Cylinder

5.1 Introduction

Incompressible fluid flow past a uniform circular cylinder has been widely studied, both for its relevance to numerous engineering applications and its use as a fundamental benchmark for computer simulations and their ability to resolve flow separation behind bluff bodies. There is a wide range of numerical and experimental literature analysing the stability aspects of this flow. As such, this flow provides a simple geometry on which to explore local stability concepts, such as the onset of convective instability, using global techniques. The flow is non-parallel and difficult to analyse in a local context, emphasising the benefits of the global approach in exploring its transient dynamics.

Transient growth describes the increase, and the subsequent decrease in energy

of a perturbation to a globally stable flow as it advects downstream. This is due to the presence of a region of convective instability as established through local stability theory. This mechanism is known to produce growth of many orders of magnitude in separated flows with the axisymmetric sudden expansion (see Sec. 4), backward-facing step (Blackburn et al. [2008a]) and stenosis (Blackburn et al. [2008b]) providing effective examples.

The cylinder wake has appeared extensively in the literature. Both two-dimensional and three-dimensional global stability analyses have been performed (Noack and Eckelmann [1994], Mutschke et al. [1997], Barkley and Henderson [1996]). The first two-dimensional Hopf bifurcation occurs at $Re_c \approx 47$, based on the cylinder diameter and the free-stream velocity. Several local stability analyses of the cylinder wake have been conducted by Monkewitz [1988], Yang and Zebib [1989], Pier [2002] and Giannetti and Luchini [2007]. These studies determine the appearance of an absolutely unstable region at $Re_{abs} \approx 25$ but that the flow remains globally stable until the primary instability at $Re_c \approx 47$. The onset of convective instability appears to have proved more elusive to these asymptotic techniques due to the non-parallel nature of the flow immediately behind the cylinder. Monkewitz [1988] reports a value of $Re_{con} \approx 5$. The onset of convective instability appears in conjunction with the appearance of two separation points behind the cylinder as identified by Noack and Eckelmann [1994].

More recently there has been interest in how local modifications to the underlying base flow may affect the stability properties of the flow. Giannetti and Luchini [2007] have conducted a sensitivity analysis in the linearly unstable regime and determined those spatial regions with highest receptivity to mass and momentum forcing. Their analysis shows that the greatest receptivity is located in the near-wake of the cylinder in the region of absolute instability known as the wave maker, where the direct and adjoint

modes overlap. This provides a source of self-sustained oscillations in the flow. Marquet et al. [2008c] have also examined the sensitivity of the eigenvalues to modifications of the base flow in the unstable regime. In particular, they discuss the control of the flow through the addition of a secondary control cylinder which modifies the base flow so as to stabilise it.

There have been a number of experimental studies of the cylinder wake in the stable and marginally unstable regime, including Provansal et al. [1987], Zhang et al. [1995] and Le Gal and Croquette [2000]. Le Gal and Croquette [2000] studied the impulse response of the cylinder wake at subcritical Reynolds numbers, by inducing an impulse through a small displacement of the cylinder. At $Re = 35$, they observe that a wave packet is generated and subsequently advected downstream. The wave packet increases in amplitude as it advects downstream indicating experimental evidence for the presence of convective instability.

In a numerical context this flow provides an illustrative example of the importance of domain size on the accuracy of linear stability analysis and transient growth calculations. The pertinence of this dependency is increased in light of a recent publication by Abdessemed et al. [2009] on the transient growth of the cylinder wake at supercritical Reynolds numbers. The computational domain, while satisfactory for a linear stability analysis, proves to be more seriously inaccurate in terms of computing optimal growth. Marquet et al. [2008c] compute the direct and adjoint modes of the supercritical flow, for which the adjoint modes are seen to extend far upstream of the cylinder. Consequently, transient growth analysis ought to be significantly influenced by upstream mesh geometry, even though the global stability analysis may be less so. More critically, numerical convergence of the underlying basic flow, the downstream profile of which is strongly affected by the cross-stream mesh size, is found to be of greater

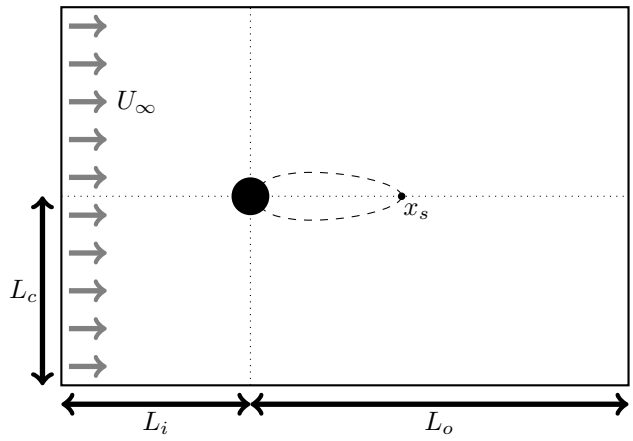

Figure 5.1: Diagram of the cylinder geometry (not to scale), showing the inflow, outflow and cross-stream dimensions referenced later. Also marked are the separation streamlines and the stagnation point, x_s.

importance in performing accurate transient growth analysis.

The purpose of the current study is two-fold. Primarily, it describes quantitatively the global transient dynamics of the flow in the sub-critical regime. Moreover, aims to highlight the importance of ensuring numerical convergence of the geometry when using global techniques.

5.2 Formulation

The geometry under consideration is an open flow past a circular cylinder of infinite length and diameter D. The geometry is homogeneous in the direction of the cylinder axis and the direction of flow is normal to this axis. This is represented by the diagram in Fig. 5.1. The formulation is similar to that described in earlier chapters, but we will summarise it here for clarity.

The fluid is governed by the incompressible Navier-Stokes equations

$$\partial_t \boldsymbol{u} + (\boldsymbol{u} \cdot \nabla)\boldsymbol{u} = -\nabla p + Re^{-1}\nabla^2 \boldsymbol{u}, \tag{5.1a}$$

$$\nabla \cdot \boldsymbol{u} = 0. \tag{5.1b}$$

Here $\boldsymbol{u}$ is the fluid velocity, p is the static pressure and, without loss of generality, we choose the density to be unity. The equations are non-dimensionalised by U_∞, the free-stream velocity, and D, the diameter of the cylinder. The Reynolds number, Re, is therefore defined as

$$Re = \frac{U_\infty D}{\nu}.$$

By considering the flow as a linear superposition of a basic flow, $\boldsymbol{U}$, and an infinitesimal perturbation $\boldsymbol{u}'$, we may express the forward linearised Navier-Stokes equations as

$$\partial_t \boldsymbol{u}' + (\boldsymbol{u}' \cdot \nabla)\boldsymbol{U} + (\boldsymbol{U} \cdot \nabla)\boldsymbol{u}' = -\nabla p' + Re^{-1}\nabla^2 \boldsymbol{u}', \tag{5.2a}$$

$$\nabla \cdot \boldsymbol{u}' = 0. \tag{5.2b}$$

The base flow, $\boldsymbol{U}$, is computed by evolving Eqns. (5.1) until a steady-state is reached. This Reynolds-number dependent solution is symmetric about the streamwise centre-line and is computed for each value of Re considered. These solutions are then stored for use in the linear stability and transient growth calculations.

5.2.1 Linear Stability Analysis

For a linear system,

$$\partial_t \boldsymbol{u}' = \mathcal{L}\boldsymbol{u}',$$

stability is characterised by the location of the eigenvalues of $\mathcal{L}$ in the complex plane, with those having positive real part indicating a globally unstable mode. The evolution

of Eqns. (5.2) may be more compactly represented by the linear operator $\mathcal{A}$ which acts as a state transition operator, advancing an initial state $\boldsymbol{u}'(0)$ to a future state $\boldsymbol{u}'(t)$ as

$$\boldsymbol{u}'(t) = \mathcal{A}(t)\boldsymbol{u}'(0).$$

The leading eigenvalues of this operator are related to those of $\mathcal{L}$, and hence can be used to assess the stability of the basic flow.

5.2.2 Transient Growth

To study the effects of convectively unstable regions of the flow we examine the relative growth in perturbation energy over a range of time horizons. The energy of a flow perturbation is denoted as $E(\boldsymbol{u}') = \langle \boldsymbol{u}', \boldsymbol{u}' \rangle$, where $\langle \cdot, \cdot \rangle$ denotes the L_2 inner-product. The growth of energy over a time τ is then given by

$$\begin{aligned} G(\tau) &= \frac{E(\tau)}{E(0)} \\ &= \frac{\langle \mathcal{A}(\tau)\boldsymbol{u}'(0), \mathcal{A}(\tau)\boldsymbol{u}'(0) \rangle}{\langle \boldsymbol{u}'(0), \boldsymbol{u}'(0) \rangle} \\ &= \max_j \lambda_j(\mathcal{A}^*\mathcal{A}) \end{aligned}$$

which reduces the problem to the computation of the leading eigenvalues of the operator $\mathcal{A}^*\mathcal{A}$. The adjoint linearised Navier-Stokes equations are

$$-\partial_t \boldsymbol{u}^* + \boldsymbol{D}\boldsymbol{N}^* \cdot \boldsymbol{u}^* = -\nabla p^* + Re^{-1}\nabla^2 \boldsymbol{u}^*$$

$$\nabla \cdot \boldsymbol{u}^* = 0$$

and a derivation of this is provided in Sec. 2.4.2.

5.2.3 Numerical Method

Equations (5.1) and (5.2) are solved using Direct Numerical Simulation (DNS) employing a split-step pressure-correction scheme (see Sec. 3.5). This is implemented in a spectral

element code utilising an elemental decomposition of the domain in the plane normal to the cylinder axis and a Fourier expansion in the axial direction for three-dimensional simulations. The choice of mesh size and domain parameters is discussed in Sec. 5.3.

Eigenvalues of a given operator are computed through a modified Arnoldi algorithm. In brief, repeated applications of the operator form a sequence of vectors from which a low-dimensional approximation of the operator can be constructed and consequently encapsulates sufficient information to approximate the leading eigenvalues and eigenvectors of the system. The technique used to apply the operators $\mathcal{A}$ and $\mathcal{A}^*\mathcal{A}$ is that of a time-steppers approach (Barkley et al. [2008]) in which we advance an arbitrary initial solution to a fixed time to perform a single iteration of the Arnoldi process. For further details see Sec. 3.6.

5.3 Influence of Domain Size

We now present a detailed convergence study on how a spatially restricted domain affects the base flow, linear stability and optimal growth calculations. Both the inflow length, L_i, and the cross-stream half-length, L_c, are investigated. The downstream mesh, L_o, must be of sufficient length to accommodate the evolution of a perturbation for the largest τ value under consideration during the transient growth analysis. Therefore, based on U_∞ and the maximum value of τ, we fix the outflow length at $L_o = 125$. All calculations concerning the size of the domain are performed using a polynomial order of 9. The specific choice of polynomial order to use for the transient growth results reported in Sec. 5.4 is decided after the domain size is determined. Throughout this convergence analysis the properties of the flow at three values of Reynolds number ($Re = 5$, $Re = 20$ and $Re = 46$) will be considered, to ensure the mesh is capable of resolving all solutions in the subcritical range.

5.3.1 Base Flow

The accuracy of the base flow is partly assessed through examination of the stagnation point location. Figure 5.2 shows the percentage error in the streamwise position x_s, as shown in Fig. 5.1, with varying mesh dimensions. While x_s is linearly dependent on Reynolds number (Giannetti and Luchini [2007]), the error in the location of this *no-flow* point is predominantly independent of Reynolds number and is generally influenced by the extent of the inflow. At low Reynolds numbers, the effects of cross-stream mesh restrictions has a limited impact on the location of the stagnation point.

Examination of the cross-stream velocity profile at a fixed streamwise station, is found to provide a more representative measure of base-flow distortion. Figure 5.3 shows such velocity profiles at a fixed cross-section of $x = 3$. It is evident that the basic flow in this geometry is particularly sensitive to the size of the computational domain. Contrary to the conclusions drawn from the analysis of the stagnation point, constrictions on the cross-stream size of the mesh at low Reynolds number (Fig. 5.3(b)) lead to an especially inaccurate calculation of the basic flow. A limitation on inflow length (Figs. 5.3(a) and 5.3(c)) is found to have a less significant effect in general.

It is known that no solution exists to Stokes flow around a circular cylinder due to the impossibility of satisfying both the boundary conditions on the cylinder and those at infinity (see Proudman and Pearson [1957]). It transpires that Stokes equations are only valid in close proximity to the cylinder. This raises questions about the accuracy of calculations of basic flows at low Reynolds numbers, especially within a domain of limited geometry.

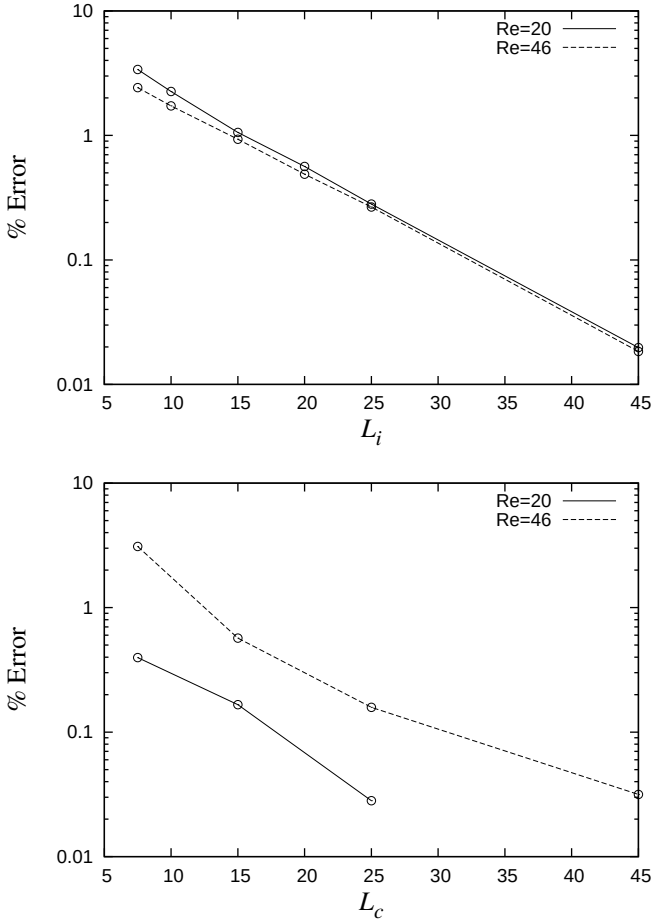

Figure 5.2: Convergence of the base flow stagnation point with mesh size. There is no discernible error in the location of the stagnation point with a cross-stream mesh dimension of $L_c = 45$.

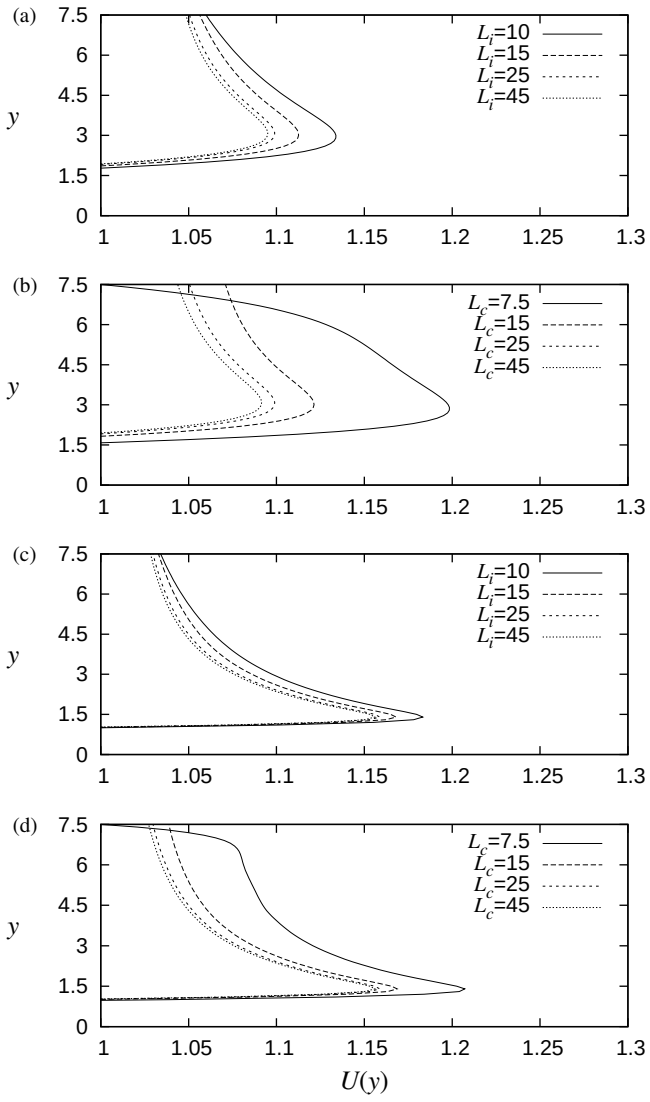

Figure 5.3: Streamwise velocity profiles of base flows at Re=5 ((a) and (b)) and Re=46 ((c) and (d)), showing variation with L_i ((a) and (c)) and L_c ((b) and (d)). For variations in L_i we fix $L_c = 25$. For variations in L_c we fix $L_i = 25$.

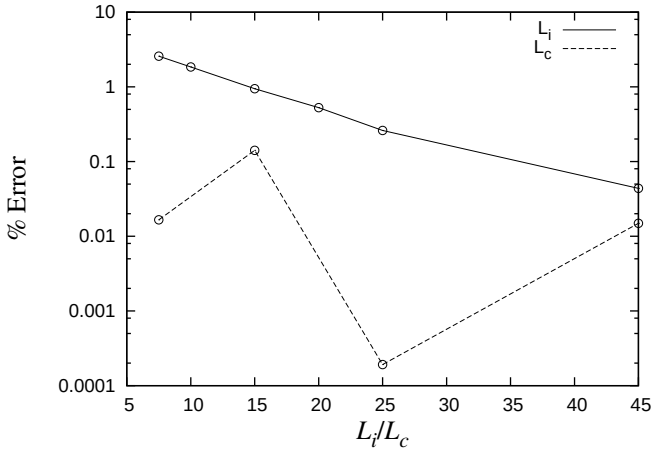

Figure 5.4: Convergence of critical eigenvalue with mesh size.

5.3.2 Linear Stability

Convergence of linear stability calculations is achieved through the determination of the critical Reynolds number. Figure 5.4 shows that the inflow aspect of the domain is the predominant source of inaccuracy, although the reported errors do not exceed 5%.

5.3.3 Transient Growth

The accuracy of transient growth computations is measured through the calculation of the relative energy growth at a fixed time horizon of $\tau = 20$. At this time horizon non-negligible growth is expected across the range of Reynolds numbers under consideration. Figure 5.5 summarises the percentage error introduced through domain size restriction.

Transient growth calculations in this geometry are found to be highly dependent on the cross-stream dimension, especially at low Reynolds numbers. This is strikingly evident from Fig. 5.5(b) where errors of $\approx 65\%$ are observed for the smallest cross-stream mesh. A sufficient computational domain upstream of the cylinder is required to fully resolve the complete structure of the optimal disturbance. The computed optimal

growth on meshes with limited inflow are found to be particularly in error at higher Reynolds numbers.

Remarkably, the percentage error does not scale with Reynolds number, suggesting these results are not shaped by a single factor, but rather by an inter-play of multiple factors. It is important to note that linear stability and transient growth calculations are both directly and indirectly influenced by the size of the computational geometry. In a direct sense, the perturbation velocity fields will be distorted in close proximity to boundaries while indirectly the perturbation is also dependent on the accuracy of the underlying basic flow. This relationship is explored further in Sec. 5.3.5.

Based on this analysis, a computational domain with $L_i = 45$ and $L_c = 45$ is optimal to resolve all aspects of transient growth calculations to within 1% for the range of Reynolds numbers under consideration. A diagram of the mesh is given in Fig. 5.6. We will subsequently refer to this mesh as M_{opt}.

5.3.4 Polynomial Order

The polynomial order is chosen to ensure the necessary global refinement needed to resolve the finer characteristics of the flow at the highest Reynolds number under consideration. This is determined using a convergence study at $Re = 46$, the results of which are summarised in Table 5.1. A polynomial order of 6 was found to be sufficient.

5.3.5 Direct and Indirect Effects of Geometry

The previous results highlight the importance of domain size for accurate calculations of base flows, linear stability and transient growth. We now address the relative contributions of direct and indirect effects of domain constriction to the global stability analysis

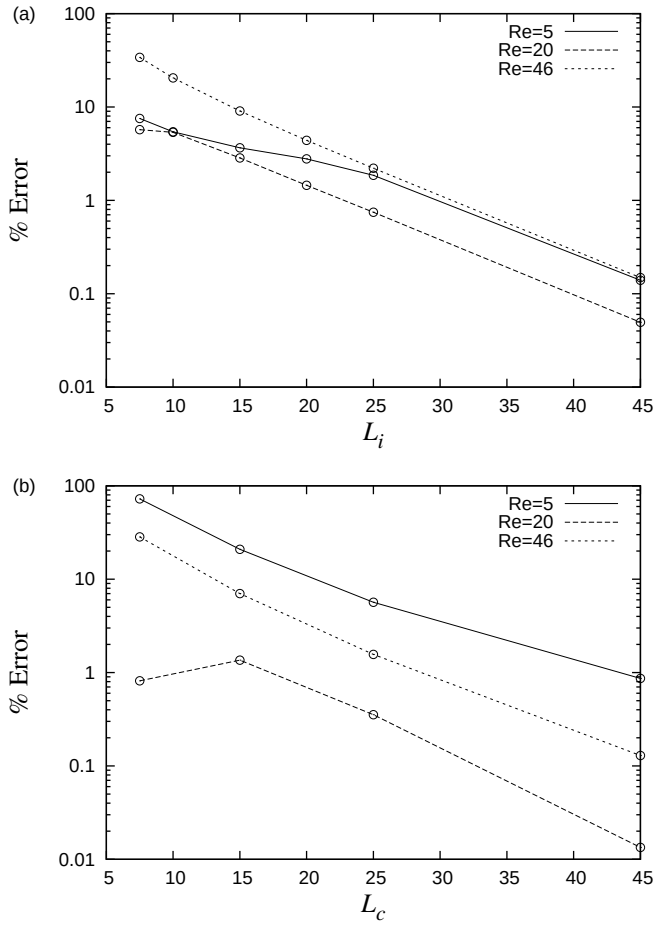

Figure 5.5: Convergence of optimal growth calculation with mesh geometry by (a) inflow length L_i, and (b) cross-stream length L_c. Optimal growth is for a time horizon of $\tau = 20$. Percentage errors are shown relative to the calculation using $L_i = 65$ and $L_c = 65$, respectively.

Order	Re=46
3	138.91
4	108.29
5	156.29
6	156.20
7	156.19
8	156.19

Table 5.1: Convergence of optimal growth with polynomial order on converged mesh ($L_i = 45$, $L_c = 45$, $L_o = 125$), with a time horizon of 20 at $Re = 46$.

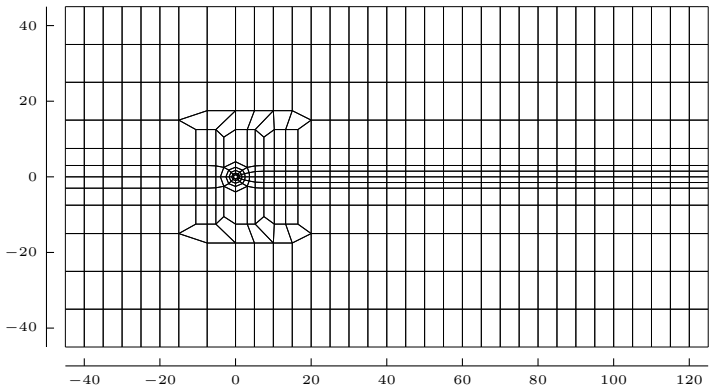

Figure 5.6: Elemental mesh determined necessary to attain an acceptable accuracy for transient growth calculations. Dimensions are $L_i = 45$, $L_c = 45$ and $L_o = 125$ (refer to Fig. 5.1 for definitions).

and transient growth problems. We will proceed through examination of calculations performed on both M_{opt} and a suboptimal mesh, M_{sub}. Specifically, this geometry matches that used in Abdessemed et al. [2009]. It has bounds $-8 \leq x \leq 95$ and $-12.5 \leq y \leq 12.5$.

Global Stability Analysis

The effect on the global stability analysis of domain size is effectively determined through examination of the critical Reynolds number of the first global bifurcation. Stability analysis performed on the M_{sub} mesh yielded a critical value of 45.58. This is lower than the value reported on the M_{opt} mesh of 46.61 (see Sec. 5.4.2), although only by 2%. The global modes are typically downstream of the cylinder and so are predominantly unaffected by the upstream domain directly. The modes take the form of streamwise oscillatory structures with limited cross-stream spatial extent and so, in our study, they are not directly susceptible to cross-stream domain width. In contrast, if the stability calculation is performed on M_{sub}, but using the base flow computed on M_{opt}, the error is an order of magnitude smaller with the critical Reynolds number computed as 46.7.

Transient growth analysis

In assessing the effects of domain size on the transient growth analysis, we will investigate the individual contributions of the base flow and geometry to the error observed in the calculation on M_{sub}. On this mesh we will denote the base flow developed as B_{sub} and the optimal perturbation as P_{sub}. Similarly, the base flow B_{opt} and the perturbation P_{opt} will refer to those solutions computed on M_{opt}. The growth corresponding to the direct evolution of P_{sub} and P_{opt} on their respective meshes is given in Table 5.2. This table also details the evolution of P_{sub} on the optimal mesh and under both base flows.

It is immediately apparent from Table 5.2 that there is a gross difference in the reported transient growth on the two domains. In line with the analysis in Sec. 5.3.3, the error in computing the growth on M_{sub} is 32%. Reassuringly, evolving P_{sub} on M_{opt} (with base flow B_{opt}) gives a significantly smaller growth than that of P_{opt}. This is, of course, to be expected since P_{opt} is, by definition, optimal for this domain.

We now address the direct effects of geometry on the evolution of a perturbation and the effects of a distorted base flow. Using the optimal base flow B_{opt} with both M_{sub} and M_{opt}, we compare the evolution of the perturbation P_{sub} on these domains. For the suboptimal domain, B_{opt} is projected onto M_{sub} to give $B_{\text{opt-sub}}$. The difference in growth is 4.4%. This shows that there is a limited effect on the perturbation from the domain size alone, given an accurate base flow. This is not surprising since the optimal perturbations and their subsequent evolution occupy a narrow cross-stream extent. In contrast, the difference in growth from using B_{sub} and B_{opt} on M_{sub} is 62%. This demonstrates that the predominant factor causing the artificially inflated growth values is due to the effect of the distorted base flow.

Mesh	Base	IC	Growth
M_L	B_L	P_L	2.54×10^3
M_L	B_L	P_S	1.85×10^3
M_S	B_{LS}	P_S	1.77×10^3
M_S	B_S	P_S	3.36×10^3

Table 5.2: Effect of mesh geometry and base flow on the evolution of perturbations. Growth values are for $\tau = 100$ at $Re = 45$. Abdessemed et al. [2009] report a growth of 3.357×10^3 at $\tau = 102$ on their mesh.

5.4 Quantitative Transient Growth Results

We now present results of a transient growth analysis in the subcritical regime.

5.4.1 Base Flows

Streamlines of the basic flow at $Re = 40$ are displayed in Fig 5.7. The flow separates from two points on the rear of the cylinder, forming a pair of recirculation bubbles directly behind the rear surface. The flow reattaches at the stagnation point x_s. The location of this point as a function of Reynolds number has been determined in many previous studies (for example, Giannetti and Luchini [2007]) and the value established in our convergence study matches this literature. Base flows are qualitatively the same at all Reynolds numbers, except for those below $Re \simeq 5$ for which there is only a single point of separation (Noack and Eckelmann [1994]). The stagnation point appears at $Re = 6.27$, shortly after the flow separation point at the rear of the cylinder splits into two. All base flows are symmetric about the streamwise centreline.

5.4.2 Global Stability

The global stability of flow past a cylinder has been reported in numerous studies with recent calculations by Marquet et al. [2008c] and Giannetti and Luchini [2007] quoting values of $Re_c = 46.8$ and $Re_c = 46.7$, respectively. As such it will not be discussed in

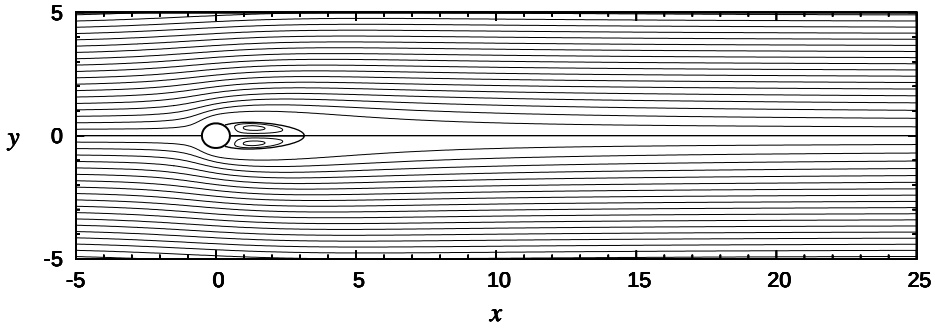

Figure 5.7: Streamlines of the base flow at Re=40. Base flows at other Re are qualitatively similar. The main flow field uses a contour separation of 0.25, while a smaller spacing of 0.01 was used to highlight the recirculation bubble. The entire computational domain is not shown.

depth here. The value of $Re_c = 46.61$ found in the present study is in good agreement with the literature.

5.4.3 Transient Growth

We now discuss the transient dynamics of the strictly two-dimensional case ($\beta = 0$). We seek the optimal initial flow disturbance which, when evolved under Eqns. (5.2) to a time horizon of τ, gives rise to the greatest energy growth. Figure 5.8 shows the optimal growth envelope for a selection of Reynolds numbers in the range of study. The curves show the maximum possible energy growth at each value of τ. Relative growth of over three orders of magnitude are observed at the highest globally stable Re. Each curve is characterised by rapid growth, similar to that observed in other separated flows, as the disturbance passes through the shear layer. The inflectional velocity profile through the recirculation regions leads to the convective instability driving this growth. Once the disturbance has passed the stagnation point, from a local perspective, it is in a stable region of the flow. For subcritical values of Re this is followed by a very gradual decay of energy, associated with the exponential decay of the dominant global modes.

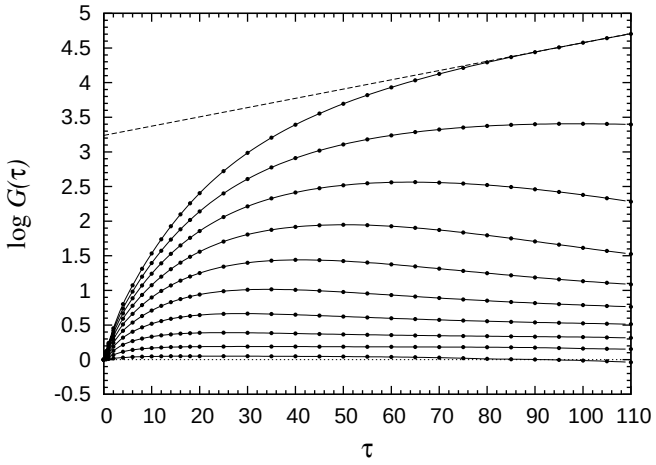

Figure 5.8: Energy growth of perturbations at different Reynolds numbers in steps of $Re = 5$ in the range $Re = 5$ to $Re = 50$. The points indicate the computed values. The dotted line shows the relative energy growth of the leading direct mode at $Re = 50$.

The uppermost line is the growth at $Re = 50$ - that is, above the onset of the first global symmetry-breaking instability. After an initial rapid growth, the energy continues increasing at an exponential rate in line with that of the leading global mode, as depicted by the dotted line in Fig. 5.8.

Figure 5.9 highlights the Reynolds number and τ dependence of the optimal growth. The thick black curve denotes the zero growth contour. For combinations of Re and τ below this curve, any initial perturbation will exhibit no overall growth relative to its initial energy. The contours further highlight the fast initial energy growth and the slow decay for long τ. The interception of the zero-growth curve with the y-axis indicates a critical Reynolds number Re_g above which there is transient growth for at least some τ. We report a value of $Re_g = 2.1$ which is slightly lower than the $Re \approx 5$ computed by Monkewitz [1988] for the onset of a convectively unstable region. The discrepancy could be accounted for by the limitations of the local analysis in the strongly non-parallel region behind the cylinder.

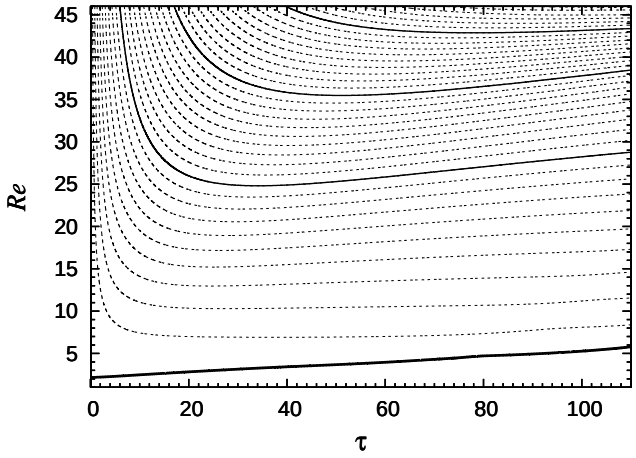

Figure 5.9: Contour plot of perturbation growth. The thicker black line denotes the contour of zero growth.

The evolution of optimal perturbations under Eqns. (5.2) at three values of τ is shown in Fig. 5.10. The circles denote the optimal growth envelope for $Re = 40$ and the three curves touch this envelope at their respective τ values. The curves show most rapid growth as the perturbation passes through the shear layer. The growth peaks as the perturbation reaches the end of this convectively unstable region, which at this Reynolds number roughly corresponds to the stagnation point (Pier [2002]). The energy of the perturbation subsequently decays. The curve for $\tau = 65$ corresponds to the choice of τ promoting the highest growth at this Reynolds number. Notably the evolution of the corresponding perturbation is nearly optimal for all time.

In Fig. 5.11 we consider the maximum growth attainable by a perturbation, not only for all possible initial conditions, but across all time horizons. In particular, this is the growth at a unique $\tau = \tau_{\max}(Re)$. The form of the perturbation evolved to $\tau_{\max}$ is representative of what might be most easily observed in an experimental setup of a perturbed flow. The maximum growth approximately scales with $\exp(Re^2)$ up to the first bifurcation point at $Re_c \approx 47$. In this figure Re_g^2 is the interception of the curve

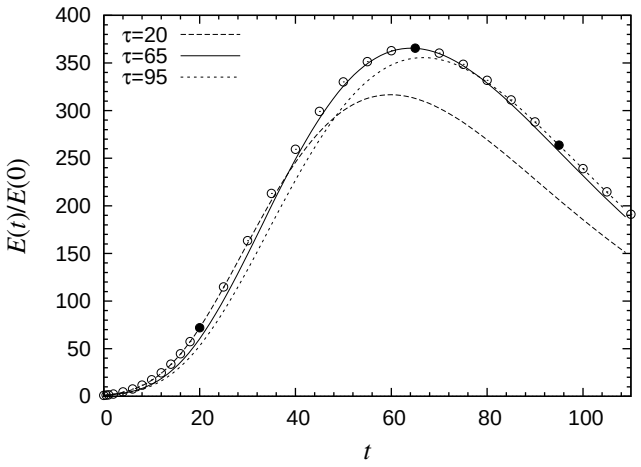

Figure 5.10: Linear evolution of perturbations for three time horizons at Re=40. At $\tau = 65$ the energy growth is nearly optimal for all time.

with the x-axis, although the exact value is not clear from the figure.

Visualisations of the initial optimal perturbation for Reynolds numbers 20 and 40 are shown in Fig. 5.12. It is apparent that the optimal disturbance at $Re = 40$ is confined closer to the cylinder than at low Reynolds numbers. We now linearly evolve these initial disturbances in time to examine their developing structure. Figure 5.13 shows snapshots of this evolution after 100 time units. There is a clear distinction between these two cases. At $Re = 20$, the disturbance is in the form of a single packet which advects steadily downstream. After reaching a peak growth of 4.70 at a time of 28.8, the disturbance gradually decays. This decay rate is almost negligible and these structures are transported for long distances with minimal energy loss, as is apparent in Fig. 5.8.

At $Re = 40$, the structure is characterised by an oscillator driving the flow directly behind the cylinder. This results in a long tail of sinuous oscillations behind the disturbance, which resembles the downstream oscillations reported by Le Gal and Croquette [2000] for $Re = 35$ in their experimental study. Again, there is negligible

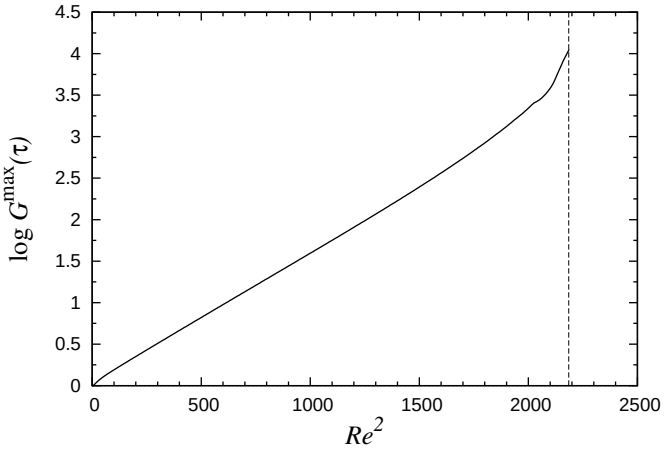

Figure 5.11: Maximum growth over all time horizons as a function of the square of Reynolds number (not quite a straight line). The dotted line signifies the square of the critical Reynolds number.

energy decay and consequently the structure is preserved far downstream. In a local stability context, this is a region of local absolute instability just behind the cylinder which is present at $Re = 40$, but not at $Re = 20$. This would align with the results of Pier [2002] who reports the appearance of a region of absolute instability immediately behind the cylinder at $Re = 25$.

The three-dimensional structure of the flow is now considered by introducing a third variable into the parameter space. Growth over the range of span-wise wavenumbers is now considered and Fig. 5.14 confirms that for large τ, wavenumber zero is the dominant mode for transient growth. However, for small $\tau < 8.0$, the greatest growth is seen in a wavenumber $0.0 < \beta < 1.0$. Figure 5.15 shows growth as a function of β and τ. As in Fig. 5.9, the thicker line denotes the zero-growth contour with positive growth occurring for those values of τ to the left. The intersection of this curve with the β-axis denotes a critical $\beta_g = 4.1 \pm 0.05$ above which all wavenumbers decay. Thus, disturbances in these high spanwise wavenumbers are not susceptible to the convective

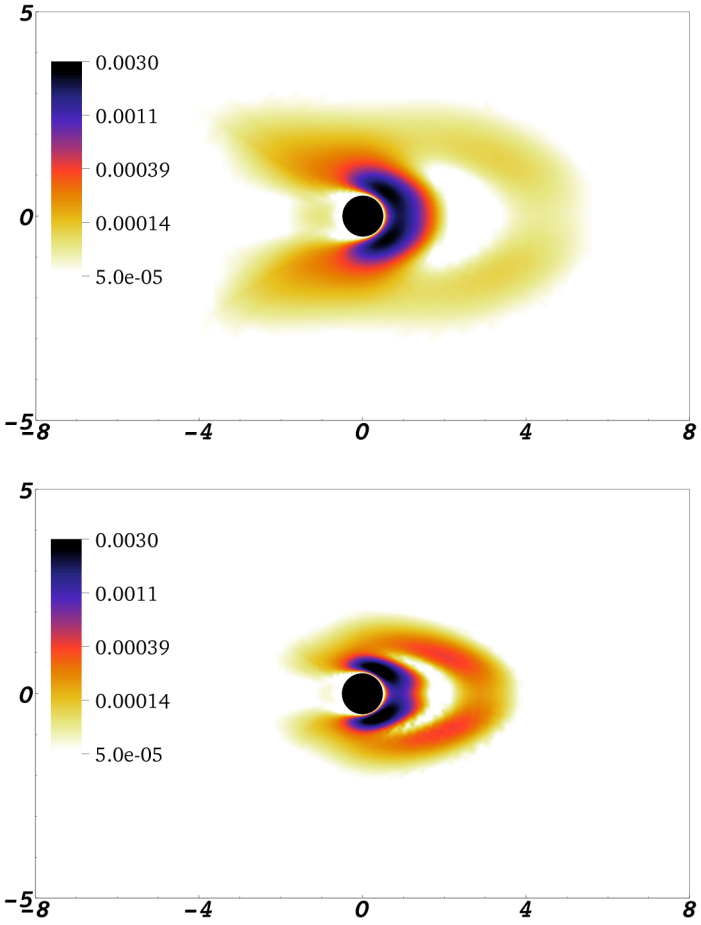

Figure 5.12: Contours of energy showing optimal initial condition at Re=20 (top) and Re=40 (bottom), both for a time horizon of τ=20.

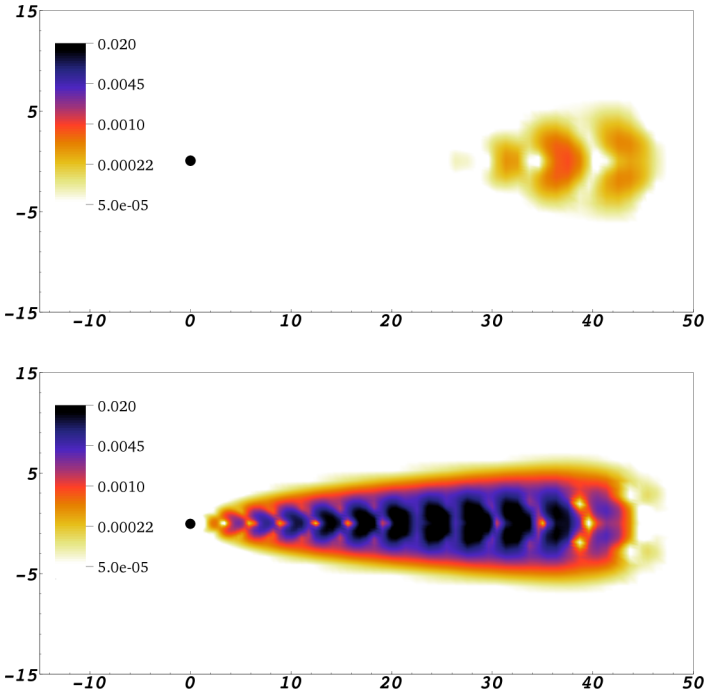

Figure 5.13: Contours of energy showing evolved optimal perturbations at Re=20 (top) and Re=40 (bottom), again for τ=20, linearly evolved to a time of $t = 050$.

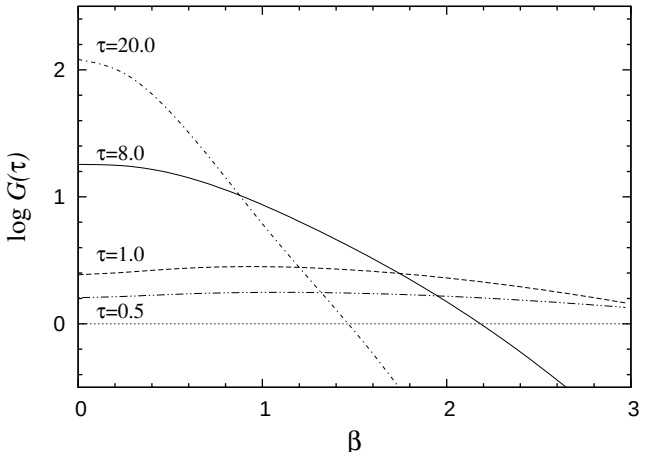

Figure 5.14: Growth of perturbations against wavenumber at Re=40. $\beta = 0$ is dominant for long time horizons, but higher β may provide slightly larger growth at short time horizons.

instabilities. Disturbances in wavenumbers $\beta > 1.0$ also exhibit a much more rapid decay of energy than is observed for $\beta = 0$.

5.5 Discussion

We have accurately determined through global techniques the transient dynamics of flow past a uniform circular cylinder. Global stability results agree with the results available in the literature. Furthermore, our determination of the onset of convective instability agrees well with existing local stability analyses of this geometry. The results give a broad insight into the transient dynamics of this prototype flow. Transient growth on the order of 10^3 is reported which, while considerably large, is comparatively small in relation to highly separated flows in discontinuous geometries such as an axisymmetric sudden expansion (see Chapter 4).

The optimal growth is observed for perturbations originating in the most sensitive regions of the flow in close proximity to the cylinder. As a disturbance passes through the

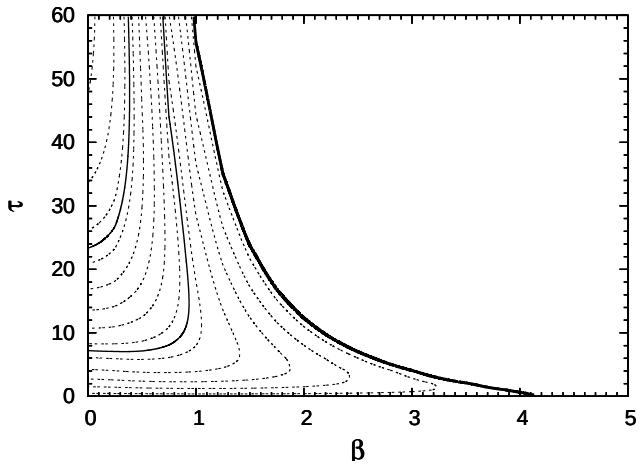

Figure 5.15: Contour plot of growth of perturbations for different spanwise wavelengths of $L = 2 * \pi/\beta$ at Re=40. The thicker black line denotes the contour of zero growth.

recirculation regions immediately behind the cylinder, it rapidly gains energy, reaching a maximum in the vicinity of the stagnation point. The recirculation region creates an inflectional velocity profile which is the source of convective instability. Furthermore, the effects of the onset of absolute instability have been identified through the evolution of optimal perturbations at $Re > 25$.

The evolution of the optimal perturbation for $\tau_{\max}$ at a given Reynolds number is found to be almost optimal for all time. This is typically not the case in other separated flows and may simplify the control of these transient dynamics in the present geometry. The optimal perturbations at different Reynolds numbers are found to differ in terms of spatial extent. Those at low Reynolds numbers typically extend over a larger region around the cylinder.

This study also highlights the importance of ensuring the numerical convergence of the computational domain. Transient growth problems are particularly susceptible to deficiencies in the extent of the mesh. This is true, not only in the downstream region, but in the cross-stream and inflow dimensions too. Enforcing boundary conditions too

close to the spatial support of the perturbation leads to direct distortion of the perturbation field. Additionally, constricted domains lead to deformation of the underlying basic flow. The cylinder wake is a prime example of a flow in which the necessary upstream length is far greater than one might initially expect, since the adjoint modes extend far upstream of the cylinder.

Abdessemed et al. [2009] examine transient dynamics of the cylinder wake above the threshold of instability, but report the growth at Re=45 as an example of the stable regime. This value is significantly larger than the value computed in the present study. In particular, they report $G(102) = 3.357 \times 10^3$, compared with $G(98.5) = 2.547 \times 10^3$, a difference of 32%. The primary difference between the problem formulations is the extent of the computational domain. In light of the results in Sec. 5.3, the mesh used by Abdessemed et al. [2009] incorporates insufficient inflow to fully resolve the optimal initial condition, a problem which will affect both the stable and unstable regimes. The optimal initial conditions close to $Re_c = 46.61$ consist of decaying sinuous oscillations upstream of the cylinder which, while comparatively small in energy, are important to the evolution of the flow and inevitably susceptible to limitations on the upstream extent.

The convergence study suggests that geometrical constraints on the perturbation itself do not wholly account for the discrepancies seen. While the disturbance has a limited cross-stream extent and is thus is not directly affected by a constricted domain, the base flow is heavily distorted by this limitation. The distortion causes an increased velocity around the shear layer which culminates in heightened transport of the disturbance by the base flow and consequently leading to an artificially large growth. In contrast, global stability analyses are affected to a lesser extent by the size of the domain, with distortion of the basic flow being the predominant source of error. Increased transport of the perturbation and consequently a marginal increase in the growth associated with

each eigenmode may account for the lower critical Reynolds number computed on a smaller mesh.

In the next chapter we will examine the generation of turbulent puffs in a gradually expanding pipe geometry.

Chapter 6

Turbulent Puffs in a Gradually Expanding Pipe

6.1 Introduction

Transition to turbulence in a circular pipe has intrigued physicists for over a century, ever since the original observations of Reynolds [1883]. Reynolds noted that below a critical value of a non-dimensional constant (now known as Reynolds number) a flow subjected to any disturbance would recover laminar Hagen-Poiseuille flow, while above this value sinuous oscillations could be seen. This limit was at $Re \approx 2000$ and, even when studied through highly controlled modern experiments, this value is considered particularly accurate. Reynolds also observed that the flow could remain laminar if unperturbed to a much higher $Re \approx 17000$, although this limit has now been increased considerably. He observed that in smaller tubes, the disturbance to steady flow would occur intermittently in patches. These *flashes*, were later classified into *puffs* and *slugs*.

Turbulent puffs and slugs are types of turbulent transitional structures which,

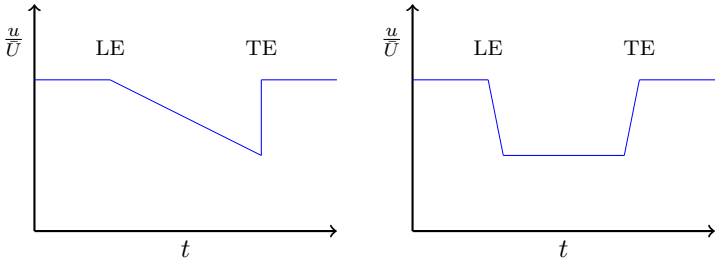

Figure 6.1: Schematic velocity traces for a puff (left) and a slug (right). The puff is characterised by the non-distinctive leading edge (LE) defined by larger-scale structures. The turbulent slug (right) has well defined leading and trailing edges (TE).

while localised in nature, possess fundamental differences in their structure and behaviour. We briefly state the characteristics of the two types. A schematic velocity trace of the two phenomena is shown in Fig. 6.1.

Puffs are typically seen in experiments at low transition Reynolds numbers $2000 < Re < 2700$ (Wygnanski and Champagne [1973]) as the flow becomes conditionally unstable to disturbances, although this is typically an overestimate to that observed in DNS. They are characterised by a distinctive upstream boundary (termed the trailing edge) which advects with the flow at slightly under the mean velocity. The turbulent state near the upstream boundary morphs into larger scale structures and waves before eventually falling to the laminar state at the downstream boundary. This boundary is not well defined. Puffs exhibit slow or negligible growth, since both boundaries advect with similar velocities. In the case that it does not grow, the puff is termed an *equilibrium puff*.

In contrast, a turbulent slug has both well-defined upstream and downstream boundaries. These transitional pockets of turbulence form at higher Reynolds numbers $Re > 3500$ in experiment (Wygnanski and Champagne [1973]). A notable difference to puffs is that the downstream boundary moves faster than the upstream boundary, especially at large Reynolds numbers. Consequently, slugs typically grow in size during

their lifetime. The inner structure of a slug is similar to that of a fully-developed turbulent flow and they contain none of the larger-scale features seen in puffs (Wygnanski and Champagne [1973]).

Much of the existing literature on pipe transition has been predominantly experimental in nature, due to the considerable computational expense of numerically simulating turbulent flows accurately. Experimental studies initially concentrated on determining the upper critical limit for transition. The extensive investigation of Wygnanski and Champagne [1973] focused on the intermittent behaviour around transition, reporting on the characteristics and formation of these turbulent phenomena. Slugs are found to develop at $Re > 3500$ with small magnitude disturbances, while puffs occur in the $2000 < Re < 2700$ range but require a disturbance of an order of magnitude greater. A further study (Wygnanski et al. [1975]) describes the development of equilibrium puffs at $Re = 2200$. These puffs were found to remain indefinitely and while their structure is very different from turbulent pipe flow, their form is found to be independent of the source disturbance.

Experiments by Bandyopadhyay [1986] provide a detailed description of the structure of puffs. The laminar flow enters the slower moving puff at the centre of the pipe and the resulting shear flow leads to a train of vortices near the wall, which defines the upstream boundary. The remainder of the conical puff is filled with vortices decaying in a helical motion. Later experiments by Darbyshire and Mullin [1995] report that these can develop in the broader range $2100 < Re < 2400$. They also speculate that the downstream large-scale structures are decaying remnants of the slower moving upstream boundary, rather than laminarisation caused by the turbulent regions creating a reduction in Reynolds number.

More recent experimental work includes Peixinho and Mullin [2006], Mullin and

Peixinho [2006] and Peixinho and Mullin [2007]. In particular, Peixinho and Mullin [2006] study the destruction of an equilibrium puff in an otherwise laminar flow at $Re = 1900$ through the reduction of Reynolds number. They observe that the puff shrinks in size and that the vigorous motion in the upstream boundary becomes detached from the wall.

Numerical studies have only appeared in the literature during the last decade. Shan et al. [1999] conducted one of the first direct numerical simulations of a puff and a slug using a spectral element code. Their method replicates the experiments and their results correlate well with the experimental data. They analyse the entrainment of fluid establishing that in a puff particles are continuously exchanged with the surrounding laminar flow, in agreement with the observations of Bandyopadhyay [1986]. Furthermore, they find the influence of initial conditions negligible, which is consistent with experiments. Recently, Willis and Kerswell [2007] have numerically established statistics of relaminarisation of turbulence in a pipe. This included confirming an exponential distribution for the probability of a puff relaminarising.

Most experimental and numerical studies typically induce puffs, slugs and turbulent flow through excitement of a laminar flow at a target Reynolds number. Alternatively, one might examine the process of laminarisation of a fully-developed turbulent flow as the Reynolds number is decreased. This is the approach taken here. This study aims to demonstrate a novel method of continuously generating turbulent puffs through an effective drop in Reynolds number, prescribed by a gradual increase in pipe radius. A constant flux is used ensuring the downstream Reynolds number is well-defined.

6.2 Methodology

The flow in the pipe is governed by the incompressible Navier-Stokes equations

$$\partial_t \boldsymbol{u} + (\boldsymbol{u} \cdot \nabla)\boldsymbol{u} = -\nabla p + \nu \nabla^2 \boldsymbol{u}, \tag{6.1a}$$

$$\nabla \cdot \boldsymbol{u} = 0 \tag{6.1b}$$

where $\boldsymbol{u}$ is the fluid velocity, p is the static pressure and we take the density, ρ, to be unity. The characteristic length and velocity scales are taken as the pipe diameter, D, and the bulk velocity, $\bar{U}$. As such the Reynolds number is given by

$$Re = \frac{\bar{U} D}{\nu}. \tag{6.2}$$

6.2.1 Periodic Domain

Before pursuing the expanding pipe geometry, we will first generate a single puff in a periodic pipe to study its structure and allow an effective comparison later. The geometry used is a uniform pipe of length $30D$ with periodicity enforced in the streamwise direction. Experimental techniques typically use a perturbation to an otherwise laminar flow as a mechanism for generating a puff. Here, we will take a different approach and gradually decrease the Reynolds number of a fully turbulent flow in a periodic domain. A sequence of simulations are performed at gradually decreasing Reynolds numbers, each restarted from the result of the previous computation. The Reynolds number needs to be lowered gradually to prevent the flow undergoing a complete transition to a laminar state.

6.2.2 Geometrical Configurations

We propose the use of a gradually expanding axisymmetric pipe for the generation of turbulent puffs. A diagram of such a geometry is shown in Fig. 6.2 (not to scale).

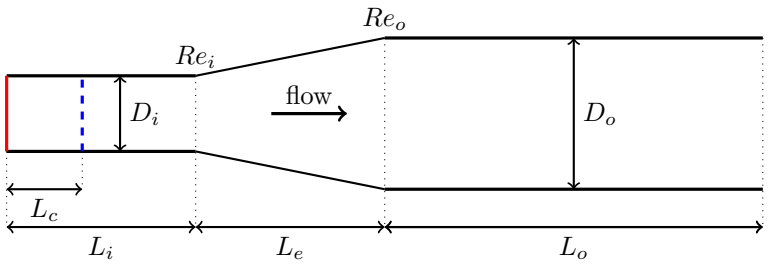

Figure 6.2: Geometry of the puff generator (not to scale).

The pipe has an inlet section of length L_i and diameter D_i. This diameter defines a length scale for the upstream Reynolds number, Re_i. A gradual expansion of length L_e, increases the size of the pipe to a diameter of D_o. This is followed by an outflow of length L_o at this diameter. We define the expansion factor $\eta = D_o/D_i$. The expansion results in a diametral increase by a factor of η and a decrease of velocity by a factor of η^2. The effective Reynolds number of the flow after the expansion is then

$$Re_o = \frac{1}{\eta} Re_i. \tag{6.3}$$

We will report in Sec. 6.3 the generation of puffs using two configurations of the expanding geometry, defined by the expansion factor, η, and the expansion length, L_e.

6.2.3 Numerical Techniques

The axisymmetric nature of the problem lends itself to the use of cylindrical coordinates (see Blackburn and Sherwin [2004]). The axial-radial semi-plane is discretised using a spectral element formulation, while a Fourier expansion is used in the azimuthal coordinate. The number of Fourier modes is typically $N_z = 32$ or $N_z = 64$. The distribution of mesh elements accounts for the spread of points with increasing radius and the necessity to accurately resolve the boundary layer. A section of the mesh is shown in Fig. 6.3. Elements are of equal width in the axial direction and increase in height proportionally

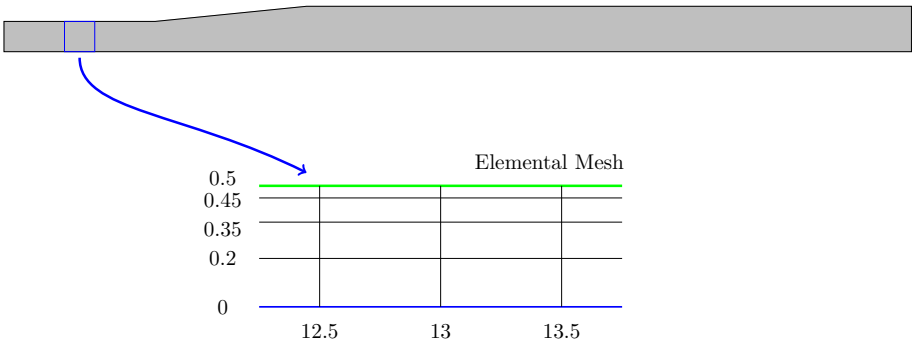

Figure 6.3: Gradual expansion computational mesh. All elements are $0.5D_i$ wide and have heights as shown. The element distribution is scaled in proportion through the expansion. On each element the solution is represented on a grid of quadrature points.

through the expansion.

The fluid is driven using flowrate control (see Sec. 3.5.4). In short, a scaled solution to the Stokes problem is added to the velocity field at each timestep to ensure the mass flux through each cross-section of the pipe remains constant.

6.2.4 Boundary Conditions and Turbulence Generation

Due to the non-periodicity in the streamwise direction, this domain requires a turbulent field to be imposed at the upstream boundary. A *copy boundary condition* is used (see Sec. 3.4) with boundary data being acquired from a cross-section of the pipe a distance of L_c downstream of the inlet, to create a periodic region. This part of the domain is initialised with a pre-computed turbulent field, computed using a periodic pipe of length L_c.

6.3 Results

In this section we present the results of DNS for generating puffs at the laminar-turbulence transition boundary. We first report the generation of a puff in a $30D$

periodic pipe using stepped decreases in Reynolds number and describe its formation and structure. We will then present evidence of puff generation in a gradually expanding pipe.

6.3.1 Puff Structure

Figure 6.4 shows a typical puff, at $Re = 2050$. This is formed through a gradual decrease in Reynolds number of a fully-turbulent flow, initially at $Re = 3000$. Figures 6.4(a) and 6.4(b) show the magnitude of streamwise vorticity and the magnitude of transverse velocity, respectively. Figure 6.4(a) emphasises the strong vorticity in the boundary layer caused by the shearing of the fast core flow with the slower-moving turbulence in the outer layers of the pipe. It is at this trailing edge where the turbulent energy of the puff is constantly replenished. The boundary-layer vortices are shed downstream, dissipating into larger structures before becoming laminar. These shed vortices are drawn into the centre of the pipe by the faster flow and this forms the conical shape characteristic of a puff.

The streamwise velocity trace in Fig. 6.4(c) emphasises the sudden drop in core velocity at the trailing edge of the puff, and the gradual recovery towards the leading edge. The plot matches the typical form reported in the literature (for example, see Willis and Kerswell [2007]). Figure 6.4(d) shows cross-sections of the puff at three-diameter intervals, highlighting the variation with radius of the puff's structure along its length. Puffs at $Re = 2050$ are found to have a length of approximately $20D$.

We now aim to simplify the generation and subsequent study of these transitional structures through the use of a gradually expanding pipe to effect a similar gradual decrease in Reynolds number within a single simulation.

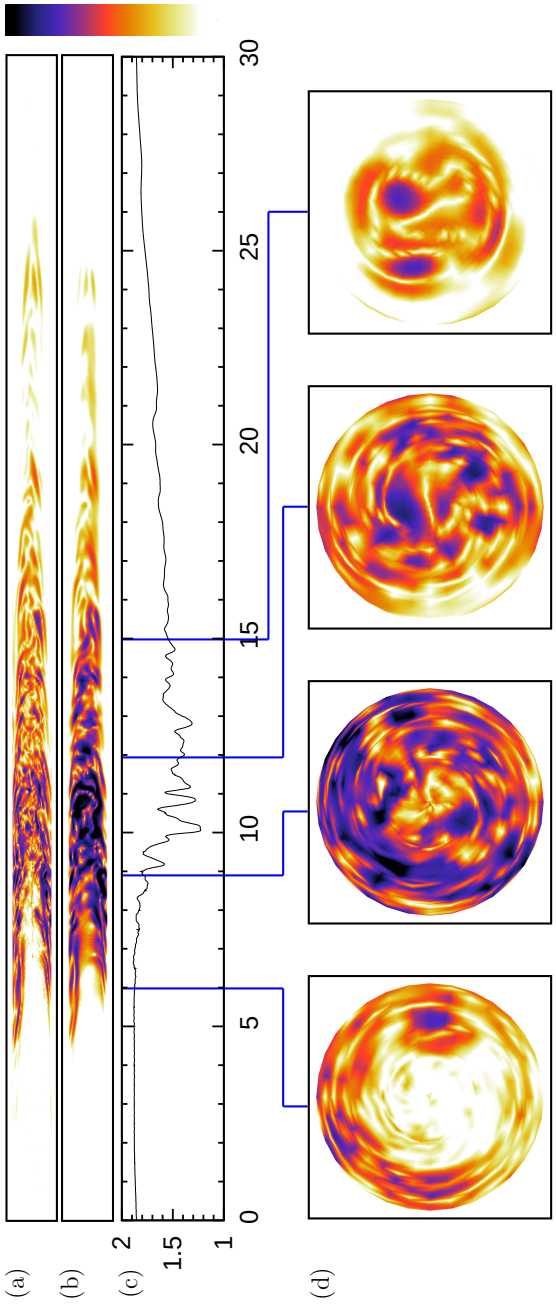

Figure 6.4: Turbulent puff at Re=2050 showing (a) streamwise vorticity magnitude, (b) transverse velocity magnitude, (c) streamwise velocity along centreline of pipe, (d) cross-sections through puff at intervals of $3D_i$. The vorticity and transverse velocity plots are normalised and the scale shows two orders of magnitude.

6.3.2 Large Reynolds Number Drop

To emulate a drop in Reynolds number similar to that of the periodic case above, we use an expansion factor of $\eta = \frac{3}{2}$ with an upstream Reynolds number of $Re_i = 3300$. This culminates in a Reynolds number reduction to $Re_o = 2200$, over a length of $L_e = 30D_i$. An inflow length of $L_i = 30D_i$ is used with an outflow of length $L_o = 90D_i$. The total pipe is therefore $150D_i$ long.

Initially, the turbulent upstream flow propagates through the expansion and into the downstream region, but only begins to laminarise towards the end of the expansion (see Fig. 6.5). The breakdown of the turbulent flow occurs through an increase in the scale of the turbulent structures. Regions of the flow begin to laminarise leaving turbulent pockets which continue to propagate downstream. The speed of the flow in these laminar patches is higher than the mean advection speed of the turbulent regions, especially in the centre of the pipe. This leads to a fast core flow which penetrates the pockets of turbulence creating vortices in the boundary layer which are drawn downstream and subsequently form a puff. By the end of the pipe at $x = 150D_i$, some of these pockets form stable puffs, while others simply decay.

Figure 6.5(b) shows a typical puff as observed in the downstream region of the domain close to the outflow. At $Re = 2200$ the puff structure is present, but the surrounding regions are not entirely laminar. This makes effectively distinguishing the structure of the puff particularly difficult. To effectively observe puffs a lower Reynolds number is required in the outflow.

6.3.3 Small Reynolds Number Drop

We now use a smaller expansion factor of $\eta = \frac{8}{7}$ over a length of $70D_i$ with an upstream Reynolds number of $Re_i = 2200$. This is sufficiently high for turbulence to be maintained

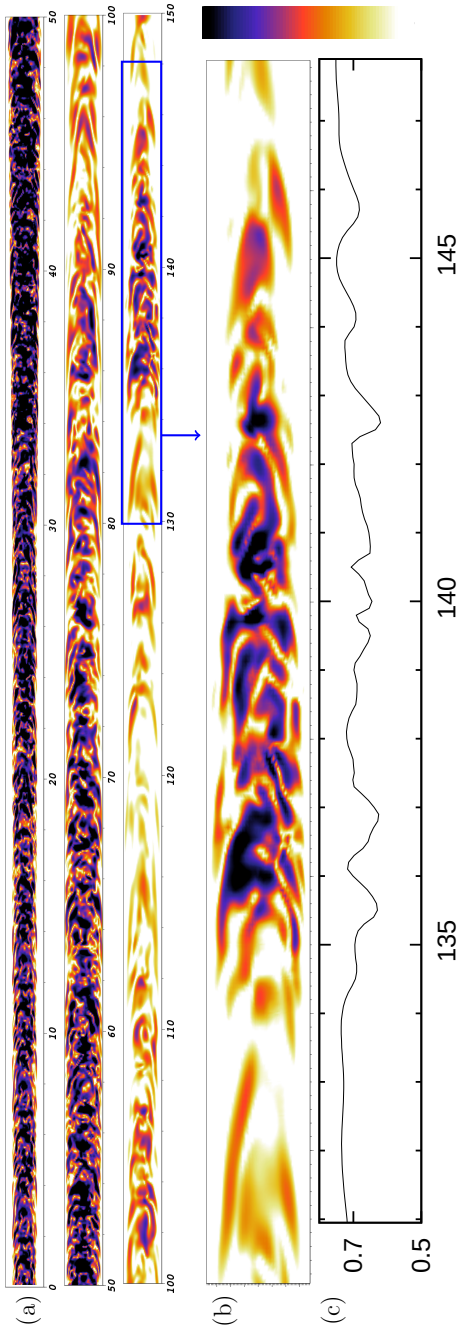

Figure 6.5: Puff structure appearing at a downstream Reynolds number of 2200. The inflow is at $Re = 3300$ and the expansion occurs in the first $50D_i$. The total length is $150D_i$. (a) Full pipe. (b) Downstream puff. (c) Streamwise velocity profile. Visualisations show transverse velocity magnitude. The colour scale shows two orders of magnitude.

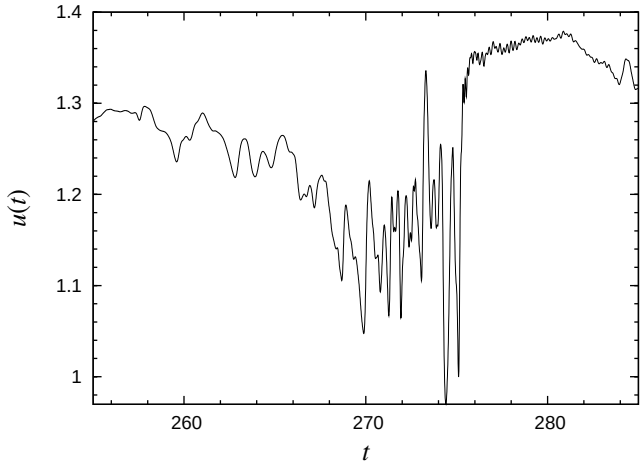

Figure 6.6: Streamwise velocity trace at $x = 250$. It shows the puff in Fig. 6.7(d) passing this point.

and the geometry results in a decrease in Reynolds number to $Re_o = 1925$. An inflow of $30D_i$ is used but the outflow is chosen to be $L_o = 200D_i$. The long outflow length allows sufficient domain for the turbulent structures to develop and be analysed.

Figure 6.6 shows a streamwise velocity trace of a fully developed puff passing a fixed streamwise station at $x = 250$, close to the end of the pipe. The trace is characterised by the gradual drop in velocity starting from the leading edge of the puff, followed by the rapid recovery at the trailing edge. This convincingly matches the typical profile of a puff described in Fig. 6.1. A visualisation of the puff associated with this trace is shown in Fig. 6.7(e).

Figure 6.7(d) shows the streamwise velocity along the centreline of the outflow region at a fixed time instant. The grey region is representative of the pipe diameter at each x position and indicates the location of the expansion. The plot is annotated with snapshots of the various turbulent structures which have formed. Immediately after the expansion the flow is still turbulent with no notable structure (Fig. 6.7(c)). Puffs are found to form shortly after the expansion and, while irregular in the frequency of their

appearance, typically remain stable once formed, propagating the length of the pipe. Figure 6.7(b) shows such a puff, located a few diameters downstream of the end of the expansion. While the regions of flow upstream and downstream of it are not particularly laminar, the puff structure is already evident. Isolated puffs can be observed in the flow as well as groups of two or more puff structures interacting with each other, such as those shown in Fig. 6.7(a). Two puffs can be seen in close proximity, with the shedded vortices of the rear puff being drawn through the trailing edge of the one in front.

Puffs develop as they travel along the outflow section of the pipe. Their structure consolidates and their trailing edge becomes more defined as the surrounding flow becomes increasingly laminar. An example of a puff close to the end of the pipe is given in Fig. 6.7(e). The trailing edge is strongly defined, as emphasised by the velocity plot in Fig. 6.7(d). Cross-sections of the puff are given in Fig. 6.7(f) which highlight the change in the location and scale of the turbulent flow along the length of the puff. The trailing edge is at $x \approx 278$ where the core flow becomes highly turbulent. The scale of the structures can then be seen to increase downstream of this point. These cross-sections both qualitatively and quantitatively match those in Fig. 6.4(d) confirming the presence of the correct structure.

All puffs appear to form a consistent length of approximately $17.5D_o$, although in those groups where the structures exhibit strong self-interaction the individual lengths are difficult to distinguish. This length is shorter than that at $Re = 2050$. It was found by Peixinho and Mullin [2006] that reducing the Reynolds number results in a shortening of the puff.

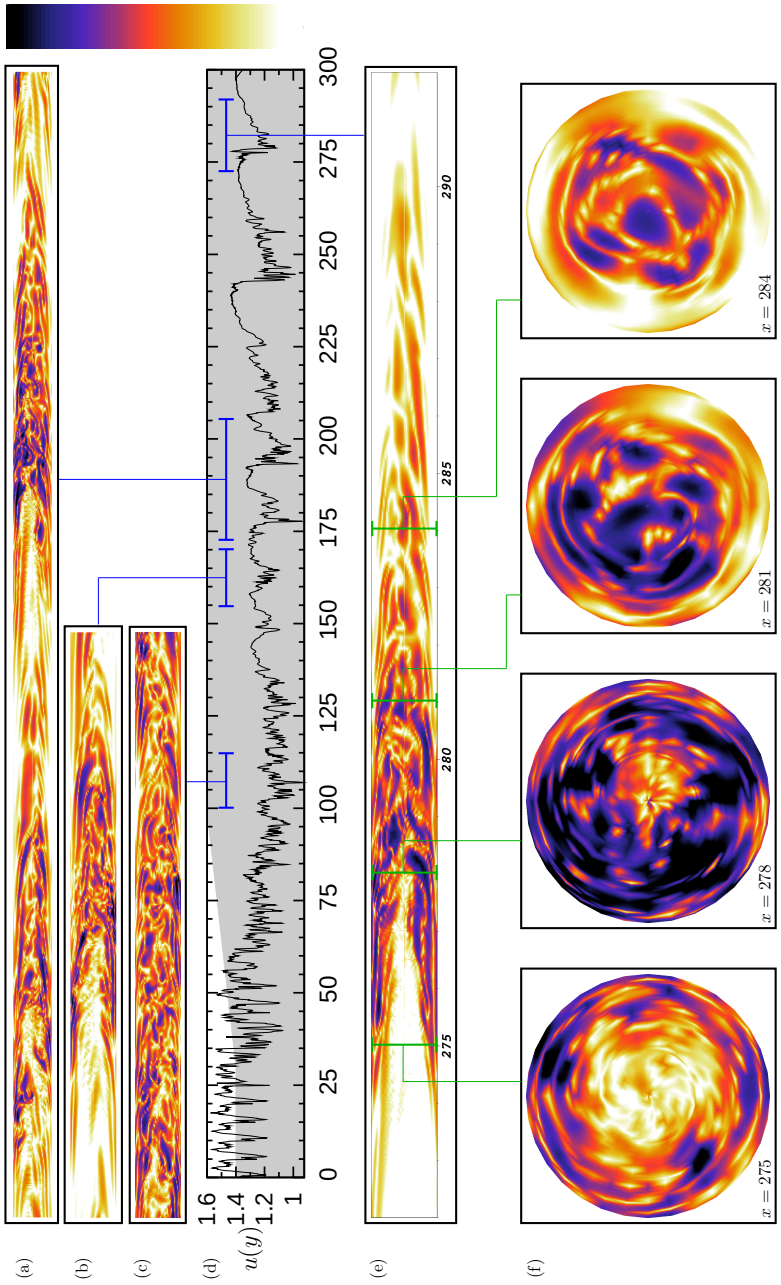

Figure 6.7: Puffs at Re=1925. All visualisations show magnitude of streamwise vorticity and the scale is logarithmic, representing two orders of magnitude. (a) Two puffs in the interval $[172, 207]$. (b) Newly formed puff in the interval $[155, 170]$. (c) The flow is still turbulent immediately after the expansion in the interval $[100, 115]$. (d) Streamwise centreline velocity. Grey area indicates pipe expansion (not to scale). (e) Fully-developed puff near outflow in the interval $[272, 292]$. (f) Cross-sections through downstream puff at intervals of $3D_o$, matching that used in Fig. 6.4.

6.4 Discussion

The production of a continuous stream of turbulent puff structures has been achieved in a single simulation using a gradually expanding non-periodic pipe, driven at a fixed Reynolds number. The gradual expansion creates a continuous drop in Reynolds number which allows the same transitional process to occur as observed in the periodic case. A turbulent field is maintained at the inlet to the pipe through the use of a *copy boundary condition*. The turbulence propagates along the pipe and begins to laminarise as it passes through the expansion. A train of turbulent puffs is then observed in the downstream region of the pipe. Puffs have been observed in this geometry at both downstream Reynolds numbers of $Re = 2200$ and $Re = 1925$. The regions between individual structures in the former case were not convincingly laminar. More acceptable results were observed at $Re = 1925$, producing a sequence of isolated puffs in conjunction with groups of two or more puffs.

From a computational perspective, the gradual expansion is an order of magnitude more costly per time step than the periodic pipe. While this is initially discouraging, the expansion provides several benefits for examining the process of transition. It requires less simulation time to produce a puff and provides a greater scope for examining the formation of puffs due to their continuous formation in the pipe. A $30D_i$ pipe will typically provide one or two puffs, while twice this number can be observed in half the simulation time in the proposed geometry. The expanding pipe also efficiently effects the gradual decrease in Reynolds number which is time-consuming to achieve in the periodic case. It is our experience that the Reynolds number must be decreased gradually to allow the formation of these transitional structures. A sudden drop in Reynolds number typically induces a rapid relaminarisation of the flow.

The expanding pipe may provide fruitful avenues for further research into the

behaviour of puffs and turbulence to laminar transition. The study of the laminarisation of a puff could be conducted by initialising the inflow region of an expanding pipe with a pre-computed puff. This could be compared with experimental studies such as Peixinho and Mullin [2006]. Furthermore, the geometry could be reversed to study the transition of a puff back to the turbulent state.

Chapter 7

Summary and Future Work

Separated flows exhibit regions of convective instability which provide a mechanism for strong transient growth of disturbances. In contrast to the asymptotic analysis, which can be used to assess the local stability properties of parallel flows, a global approach allows convective instability to be determined in a broader range of open flows through the resolution of all aspects of the flow. In particular, the transient dynamics of highly non-parallel flows in abrupt geometries or behind bluff bodies can be effectively analysed.

In this thesis we have examined the transient dynamics of two such prototype flows: the sudden axisymmetric expansion; and the cylinder wake. Both these separated flows exhibit strong transient growth, typically of many orders of magnitude. DNS of a noise-perturbed flow in the axisymmetric expansion has been conducted which confirms the linear analysis. The structures observed in both these flows have been visualised demonstrating what should be observable through experiment. Pursuit of experimental evidence for the observed dynamics would now be an important step forward.

The growth of small perturbations to flows due to convective instability may lead to transition in flows and consequently cause problems for applications in industry. One

important motivation for this work is in flow control, determining the most dangerous perturbations to a flow and finding methods to control such a flow. Transient growth analysis is a highly computationally intensive task, which requires numerous simulations to map out the growth function in the $Re - \tau$ domain. Improving the efficienty of this algorithm would be an important contribution to the field.

Finally, we have also examined the formation of puffs in the transition of pipe flow. These are typically formed in experiment through an impulse to a laminar flow. Computationally, we have described a novel formulation for the creation and study of puffs from a turbulent flow, using a gradual increase in pipe radius to effect a gradual drop in Reynolds number. The puffs produced in the simulations are consistent with those produced using existing experimental and computational techniques in the literature. We have also described how further examination of puff decay could be achieved through the use of our technique and how reversing the geometry could allow the study of transition of a puff into a turbulent flow.

Appendix A

Spectral Element Methods

The aim of this appendix is to collate the background details on spectral element techniques which would otherwise dilute the concepts described in Chapter 3.

A.1 Jacobi Polynomials

The family of Jacobi polynomials are denoted by $P_n^{\alpha,\beta}(x)$. They are a family of polynomial solutions to the *singular Sturm-Liouville* problem. Their relevance to the spectral element method is that they are orthogonal on the interval $[-1, 1]$ in the Legendre inner product, and as such provide a good expansion basis with computationally efficient properties.

Definition The Legendre inner product of two functions f and g is defined as

$$(f, g) = \int_{-1}^{1} f(x)g(x)dx. \tag{A.1}$$

The following is a list of useful expressions and relations for Jacobi polynomials which will be used later in this document. While in general Jacobi polynomials do not

have an explicit representation, they can be evaluated through the following recursion formula

$$a_n^1 P_{n+1}^{\alpha,\beta}(x) = (a_n^2 + a_n^3 x) P_n^{\alpha,\beta} - a_n^4 P_{n-1}^{\alpha,\beta}(x), \tag{A.2a}$$

$$P_0^{\alpha,\beta}(x) = 1, \tag{A.2b}$$

$$P_1^{\alpha,\beta}(x) = \frac{1}{2}[\alpha - \beta + (\alpha + \beta + 2)x], \tag{A.2c}$$

where the coefficients a_n^i are computed as

$$\begin{aligned} a_n^1 &= 2(n+1)(n+\alpha+\beta+1)(2n+\alpha+\beta), \\ a_n^2 &= (2n+\alpha+\beta+1)(\alpha^2-\beta^2), \\ a_n^3 &= (2n+\alpha+\beta)(2n+\alpha+\beta+1)(2n+\alpha+\beta+2), \\ a_n^4 &= 2(n+\alpha)(n+\beta)(2n+\alpha+\beta+2). \end{aligned}$$

An alternative representation is the differential form

$$\frac{d}{dx}\left[(1-x)^{1+\alpha}(1-x)^{1+\beta}\frac{d}{dx}\left(P_n^{\alpha,\beta}(x)\right)\right] = -\lambda_n(1-x)^{\alpha}(1+x)^{\beta}P_n^{\alpha,\beta}, \tag{A.3a}$$

$$\lambda_n = n(n+\alpha+\beta+1). \tag{A.3b}$$

The derivative can be similarly found using a recursive technique

$$\frac{d}{dx}\left[P_0^{\alpha,\beta}(x)\right] = 0, \tag{A.4a}$$

$$b_n^1(x)\frac{d}{dx}\left[P_n^{\alpha,\beta}(x)\right] = b_n^2(x)P_n^{\alpha,\beta}(x) + b_n^3(x)P_{n-1}^{\alpha,\beta}(x), \tag{A.4b}$$

where the coefficients b_n^i are computed as

$$\begin{aligned} b_n^1(x) &= (2n+\alpha+\beta)(1-x^2), \\ b_n^2(x) &= n\left[\alpha-\beta-(2n+\alpha+\beta)x\right], \\ b_n^3(x) &= 2(n+\alpha)(n+\beta), \end{aligned}$$

or using the following relation

$$\frac{d}{dx}P_n^{\alpha,\beta}(x) = \frac{1}{2}(\alpha+\beta+n+1)P_{n-1}^{\alpha+1,\beta+1}(x) \tag{A.6}$$

Further information can be found in Appendix A.1 of Karniadakis and Sherwin [2005].

A.1.1 Special Cases

Special cases of the Jacobi polynomials frequently used in the literature are:

- Legendre polynomials: $\alpha = \beta = 0$,
- Chebyshev polynomials: $\alpha = \beta = -1/2$.

A.2 Interpolation Polynomials

Definition Given a set of $P+1$ points, an interpolating polynomial is an order-P polynomial which is exactly satisfied at those points.

The pth Lagrange polynomial through a set of nodal points ξ_q is given by

$$h_p(\xi) = \frac{\prod_{q=0,q\neq p}^{P}(\xi-\xi_q)}{\prod_{q=0,q\neq p}^{P}(\xi_p-\xi_q)}. \tag{A.7}$$

The following property holds: $h_p(\xi_q) = \delta_{pq}$.

A.3 Nodal Bases

The choice of interpolation points for a nodal basis has important numerical consequences. Certain choices, as noted by Gauss, give rise to a highly accurate representation. The naming of these choices is based on the use of element end-point nodes combined with the Gaussian quadrature interior points on the standard element. The possible choices are:

- Gauss: neither endpoint is included.
- Gauss-Radau: only one endpoint is included (usually -1).
- Gauss-Lobatto: both endpoints are included.

Combining this naming scheme with the choice of (Jacobi) polynomial, for which its zeros are used to generate the interior points, gives the full name as demonstrated in the following examples.

- The Q^{th} order *Gauss-Radau-Chebyshev* scheme would consist of the point -1, and the zeros of the $(Q-1)$-order Chebyshev polynomial.
- The Q^{th} order *Gauss-Lobatto-Legendre* scheme would consist of the points -1 and 1, with the zeros of the $(Q-2)$-order Legendre polynomial.

A.3.1 Zeros and Weights for Nodal Bases

For nodal bases, the values of ξ_q and hence w_q and d_{qr} depend on the choice of scheme used to select the nodes. We let $\xi_{q,P}^{\alpha,\beta}$ denote the qth zero of the Pth order Jacobi polynomial $P_P^{\alpha,\beta}$. For the nodal schemes named above, the nodes, weights and derivatives are computed as follows:

Gauss-Legendre

$$\begin{aligned}
\xi_q &= \xi_{q,Q}^{\alpha,\beta}, \quad q = 0, \ldots, Q-1, \\
w_q^{\alpha,\beta} &= \frac{2}{1-(\xi_q)^2}\left[\frac{d}{d\xi}(P_Q^{\alpha,\beta}(\xi))\Big|_{\xi=\xi_q}\right]^{-2}, \quad q = 0, \ldots, Q-1, \\
d_{qr} &= \begin{cases} \frac{(P_Q^{\alpha,\beta})'(\xi_q)}{(P_Q^{\alpha,\beta})'(\xi_r)(\xi_q-\xi_r)}, & q \neq r, 0 \leq q, r \leq Q-1, \\ \frac{\xi_q}{1-\xi_q^2}, & q = r, \end{cases}
\end{aligned}$$

Gauss-Radau-Jacobi

$$\xi_q = \begin{cases} -1, & q = 0 \\ \xi^{\alpha,\beta+1}_{q-1,Q-1}, & q = 1,\ldots,Q-1 \end{cases}$$

$$w^{\alpha,\beta}_q = \frac{1-\xi_q}{Q^2\left[P^{\alpha,\beta}_{Q-1}(\xi_q)\right]^2}, \quad q = 0,\ldots,Q-1$$

$$d_{qr} = \begin{cases} \frac{-(Q-1)(Q+1)}{4} & q = r = 0, \\ \frac{P^{\alpha,\beta}_{Q-1}(\xi_q)}{P^{\alpha,\beta}_{Q-1}(\xi_r}\frac{1-\xi_r}{1-\xi_q}\frac{1}{\xi_q-\xi_r} & q \neq r, 0 \leq q,r \leq Q-1 \\ \frac{1}{2(1-\xi)} & \end{cases}$$

Gauss-Lobatto-Jacobi

$$\xi_q = \begin{cases} -1, & q = 0 \\ \xi^{\alpha+1,\beta+1}_{q-1,Q-2}, & q = 1,\ldots,Q-2 \\ 1, & q = Q-1 \end{cases}$$

$$w^{\alpha,\beta}_q = \frac{2}{Q(Q-1)\left[P^{\alpha,\beta}_{Q-1}(\xi_q)\right]^2}, \quad q = 0,\ldots,Q-1$$

$$d_{qr} = \begin{cases} \frac{-Q(Q-1)}{4} & q = r = 0, \\ \frac{P^{\alpha,\beta}_{Q-1}(\xi_q)}{P^{\alpha,\beta}_{Q-1}(\xi_r}\frac{1}{\xi_q-\xi_r} & q \neq r, 0 \leq q,r \leq Q-1 \\ 0 & 1 \leq q = r \leq Q-2 \\ \frac{Q(Q-1)}{4} & q = r = Q-1 \end{cases}$$

The nodes ξ_i are computed numerically (e.g. using the Newton-Raphson method), and then the weights and derivatives are computed using the recursive formulae from Eqns. (A.2) and (A.4).

A.4 Modal Bases

Following on from the definition of a modal basis in Sec. 3.1.1, we provide an example of a modal basis formed from Jacobi polynomials (see Sec. A.1). In the specific case of $\alpha = \beta = 1$, we construct a p-type modal expansion basis functions, $\psi_p(\xi)$ on the standard element as:

$$\psi_p^{1,1}(\xi) = \begin{cases} \frac{1-\xi}{2} & p = 0 \\ \left(\frac{1-\xi}{2}\right)\left(\frac{1+\xi}{2}\right) P_{p-1}^{1,1}(\xi) & 0 < p < Q \\ \frac{1+\xi}{2} & p = Q \end{cases}$$

The choice of α and β affects the structure and numerical efficiency of the matrix equations developed later, which in turn affects the performance of the final implementation.

It is evident there is a wide choice of polynomial bases of both the nodal and modal type, each with their particular benefits and flaws. The diagram in Fig. A.4 summarises a classification of different polynomial bases.

A.5 Global Assembly in 2D

The algorithms in Alg. 1 and Alg. 2 describes how to form the global assembly mapping. Algorithm 1 performs the pre-processing stage, sorting the domain components into interior and surface types. Alg. 2 constructs the actual assembly map. The procedure for generating the interior lists is similar to that of the exterior lists and has thus not been repeated.

Algorithm 1 Algorithm to produce the global assembly mapping - preprocessing.

```
create empty edge lists E_A (all), E_S (surface), E_C (common)
create empty point lists V_A (all), V_S (surface), V_C (common)
{create a list of all edges in domain}
for each element e do
  for k = 0 to k = 3 do
    add edge[k] of e to E_A
  end for
end for
{extract interior edges}
for each edge x in E_A do
  for each edge y after x in E_A do
    if x = y then
      add edge x to E_C
      remove edge x and edge y from E_A
    end if
  end for
end for
{remaining edges are surface edges}
for each edge x in E_A do
  add edge x to E_S
end for
{sort points into surface points and common interior points}
for each edge x in E_S do
  add first end point to V_S
end for
for each edge point x in V do
  if x not in V_S then
    add x to V_C
  end if
end for
```

Algorithm 2 Algorithm to produce the global assembly mapping.

```
k_p = 0, k_m = 0
{add surface points to map}
for each x in V_S do
  for each element e do
    for k = 0 to k = 3 do
      y = point k of e
      if x == y then
        i = getAssemblyMapNodeIndex(y)
        set A_P[i] = k_p
        i = getAssemblyMapModeIndex(y)
        set A_M[i] = k_m
      end if
    end for
  end for
end for
k_p += size(V_S), k_m += size(V_S)
{add surface edges to map}
for each edge x in E_S do
  for k = 0 to k = Q − 2 do
    i = getAssemblyMapNodeIndex(point k on edge x)
    A_P[i] = k_p++
  end for
  for k = 0 to k = P − 2 do
    i = getAssemblyMapModeIndex(mode k on edge x)
    A_M[i] = k_m++
  end for
end for
[ repeat similarly for common points/edges and interior points/edges ]
```

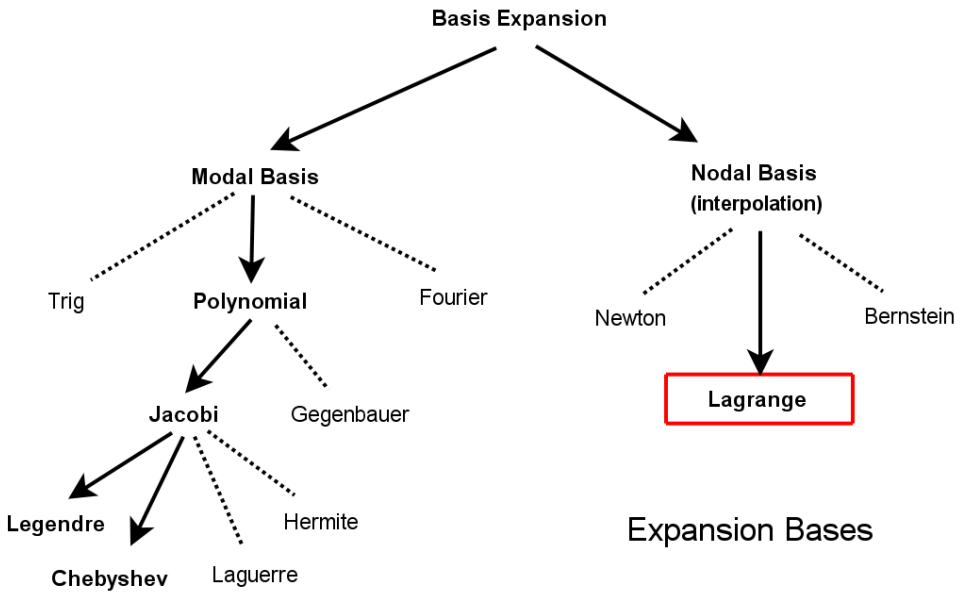

Figure A.1: Tree diagram showing the different options for expansion bases on the standard element. Solid arrows show the commonly used bases in spectral element methods.

A.6 Efficiency of 2D Matrix Systems

We briefly review two efficiency improvements which can be made in computing the Laplacian operator in two dimensions. The matrix described in Sec. 3.3.5 place a large burden on both storage and numerical efficiency. In its current form, computing individual elements of $\boldsymbol{L}$ on the fly would require significant computational cost. However, pre-computing the matrix for each element would necessitate significant storage, especially with an increasing number of elements. To improve this, the matrix operation can be rearranged to increase the separation between element-dependant and element-independent aspects of the equation by exploiting the diagonal nature of $\boldsymbol{\Lambda}_{k,l}$. The

matrix equation in Eqn. (3.7) may be expanded and rearranged to give

$$\begin{aligned}
\boldsymbol{L} &= [\boldsymbol{D}_1\boldsymbol{B}]^\top \boldsymbol{\Sigma_1} [\boldsymbol{D}_1\boldsymbol{B}] + [\boldsymbol{D}_1\boldsymbol{B}]^\top \boldsymbol{\Sigma_2} [\boldsymbol{D}_2\boldsymbol{B}] \\
&\quad + [\boldsymbol{D}_2\boldsymbol{B}]^\top \boldsymbol{\Sigma_2} [\boldsymbol{D}_1\boldsymbol{B}] + [\boldsymbol{D}_2\boldsymbol{B}]^\top \boldsymbol{\Sigma_3} [\boldsymbol{D}_2\boldsymbol{B}] \\
\boldsymbol{\Sigma}_1 &= \left(\boldsymbol{\Lambda}_{1,1}^2 + \boldsymbol{\Lambda}_{1,2}^2\right) \boldsymbol{W}^e \\
\boldsymbol{\Sigma}_2 &= \left(\boldsymbol{\Lambda}_{1,1}\boldsymbol{\Lambda}_{2,1} + \boldsymbol{\Lambda}_{1,2}\boldsymbol{\Lambda}_{2,2}\right) \boldsymbol{W}^e \\
\boldsymbol{\Sigma}_3 &= \left(\boldsymbol{\Lambda}_{2,1}^2 + \boldsymbol{\Lambda}_{2,2}^2\right) \boldsymbol{W}^e
\end{aligned}$$

The diagonal matrices $\boldsymbol{\Sigma_i}$ can be pre-computed on each element upon construction and only require $O(Q^2)$ storage. The matrices $\boldsymbol{D}_1\boldsymbol{B}$ and $\boldsymbol{D}_2\boldsymbol{B}$ are in terms of the standard element and so need only be computed once. Finally, during the construction of the global matrix system, each element can be computed as the $O(Q^2)$ operation

$$\boldsymbol{L}[i][j] = \sum_k \boldsymbol{D}_1\boldsymbol{B}[k][i] \cdot \boldsymbol{\Sigma}_1[k][k] \cdot \boldsymbol{D}_1\boldsymbol{B}[k][j] + \ldots$$

A.6.1 Computing the Diagonal Coefficients

To generate the diagonal matrices $\boldsymbol{\Sigma_i}$ we must derive the values of the $\frac{\partial \xi_i}{\partial \xi_j}$. For the two-dimensional case, consider the function $u(x_1, x_2)$ on a general-shaped element, dependent on two variables $x_1 = \chi_1(\xi_1, \xi_2)$ and $x_2 = \chi_2(\xi_1, \xi_2)$ where the χ_i's are the components of the linear mapping defined earlier. Using the chain rule, we can express the total change in $u(\xi_1, \xi_2)$ as

$$\mathrm{d}u(\xi_1, \xi_2) = \frac{\partial u}{\partial \xi_1}\mathrm{d}\xi_1 + \frac{\partial u}{\partial \xi_2}\mathrm{d}\xi_2$$

Thus for our general element

$$\begin{bmatrix} \mathrm{d}x_1 \\ \mathrm{d}x_2 \end{bmatrix} = \begin{bmatrix} \frac{\partial x_1}{\partial \xi_1} & \frac{\partial x_1}{\partial \xi_2} \\ \frac{\partial x_2}{\partial \xi_1} & \frac{\partial x_2}{\partial \xi_2} \end{bmatrix} \begin{bmatrix} \mathrm{d}\xi_1 \\ \mathrm{d}\xi_2 \end{bmatrix}$$

and inverting this system gives

$$\begin{bmatrix} \mathrm{d}\xi_1 \\ \mathrm{d}\xi_2 \end{bmatrix} = \frac{1}{J} \begin{bmatrix} \frac{\partial x_2}{\partial \xi_2} & -\frac{\partial x_1}{\partial \xi_2} \\ -\frac{\partial x_2}{\partial \xi_1} & \frac{\partial x_1}{\partial \xi_1} \end{bmatrix} \begin{bmatrix} \mathrm{d}x_1 \\ \mathrm{d}x_2 \end{bmatrix}$$

Secondly, if we also assume that the coordinate mappings χ_i are bijective mappings with inverses

$$\xi_1 = (\chi_1)^{-1}(x_1, x_2) \quad \text{and} \quad \xi_2 = (\chi_2)^{-1}(x_1, x_2)$$

then we can apply the chain rule directly to these to give

$$\begin{bmatrix} \mathrm{d}\xi_1 \\ \mathrm{d}\xi_2 \end{bmatrix} = \begin{bmatrix} \frac{\partial \xi_1}{\partial x_1} & \frac{\partial \xi_1}{\partial x_2} \\ \frac{\partial \xi_2}{\partial x_1} & \frac{\partial \xi_2}{\partial x_2} \end{bmatrix} \begin{bmatrix} \mathrm{d}x_1 \\ \mathrm{d}x_2 \end{bmatrix}$$

Equating the coefficients in these matrices then gives expressions for the terms $\frac{\partial \xi_i}{\partial x_j}$, in terms of expressions we can compute directly, as follows.

$$\begin{aligned} \frac{\partial \xi_1}{\partial x_1} &= \frac{1}{J}\frac{\partial x_2}{\partial \xi_2} \\ \frac{\partial \xi_1}{\partial x_2} &= -\frac{1}{J}\frac{\partial x_1}{\partial \xi_2} \\ \frac{\partial \xi_2}{\partial x_1} &= -\frac{1}{J}\frac{\partial x_2}{\partial \xi_1} \\ \frac{\partial \xi_2}{\partial x_2} &= \frac{1}{J}\frac{\partial x_1}{\partial \xi_1}. \end{aligned}$$

Appendix B

Spectral Element Heat Equation Formulation

B.1 Solving the 1D Heat Equation with Forcing

We give a brief example of the application of the spectral element method to solving the heat equation with a constant forcing, g, and Dirichlet boundary conditions,

$$\frac{\partial u}{\partial t} = \alpha \frac{\partial^2 u}{\partial x^2} + \beta g \tag{B.1}$$

Expressing this in the weak Galerkin form gives

$$\left(v, \frac{\partial u}{\partial t}\right) = \alpha \left(v, \frac{\partial^2 u}{\partial x^2}\right) + \beta(v, g)$$

The second-derivative can be rewritten using integration by parts.

$$\left(v, \frac{\partial u}{\partial t}\right)_\Omega + \alpha \left(\frac{\partial v}{\partial x}, \frac{\partial u}{\partial_x}\right)_\Omega = \alpha \left[v, \frac{\partial u}{\partial x}\right]_{\partial\Omega} + \beta(v, g)_\Omega.$$

The boundary terms vanish, since the test functions v_j are zero on Dirichlet boundaries. We now express u and v in terms of the spectral expansion modes ϕ_p, giving rise to the

matrix system

$$\boldsymbol{v}^\top \boldsymbol{M} \frac{\partial \hat{u}}{\partial t} + \alpha \boldsymbol{v}^\top \boldsymbol{L^{(2)}} \hat{\boldsymbol{u}} = \beta \boldsymbol{v}^\top \boldsymbol{M} \hat{\boldsymbol{g}}$$

To complete the matrix equation, $\frac{\partial \hat{u}}{\partial t}$ is discretised using the multi-step scheme in equation (3.5). A first-order implicit scheme is suitable, giving the following matrix equation.

$$\boldsymbol{M} \frac{\hat{\boldsymbol{u}}^{n+1} - \hat{\boldsymbol{u}}^n}{\Delta t} + \alpha \boldsymbol{L^{(2)}} \hat{\boldsymbol{u}}^{n+1} = \beta \boldsymbol{B}^\top \boldsymbol{W} \boldsymbol{g}$$

$$\boldsymbol{S} \hat{\boldsymbol{u}}^{n+1} = \boldsymbol{M} \hat{\boldsymbol{u}}^{n+1} + \alpha \Delta t \boldsymbol{L^{(2)}} \hat{\boldsymbol{u}}^{n+1} = \boldsymbol{M} \hat{\boldsymbol{u}}^n + \beta \Delta t \boldsymbol{B}^\top \boldsymbol{W} \boldsymbol{g}$$

A full time-stepping algorithm including Dirichlet boundary conditions can be expressed as the reduced system

$$\tilde{\boldsymbol{S}} \tilde{\hat{\boldsymbol{u}}}^{n+1} = \tilde{\boldsymbol{M}} \tilde{\hat{\boldsymbol{u}}}^n + (\boldsymbol{\alpha_M} - \boldsymbol{\alpha_S}) \hat{u}[0] + (\boldsymbol{\beta_M} - \boldsymbol{\beta_S}) \hat{u}[P_g - 1] + \beta \Delta t \tilde{\boldsymbol{B}}^\top \tilde{\boldsymbol{W}} \tilde{\boldsymbol{g}}$$

B.1.1 Validation of Results

To ensure the results produced by the numerical method are valid, we compare with an analytic solution to Eqn. (B.1). A brief derivation of an analytic solution using the separation of variables follows to demonstrate the form of the expected solution. Consider the heat equation with positive constant α.

$$\frac{\partial u}{\partial t} = \alpha \frac{\partial^2 u}{\partial x^2}$$

and express $u(x,t) = X(x)T(t)$ to give

$$\frac{\dot{T}(t)}{T(t)} = \alpha \frac{X''(x)}{X(x)} = \lambda$$

for a separation constant λ which gives two ODEs

$$\dot{T}(t) = \lambda T(t)$$

$$X''(x) = \frac{\lambda}{\alpha} X(x)$$

The two cases for $\lambda = 0$ and $\lambda > 0$ are either a trivial zero solution or non-physical. For $\lambda < 0$, let $\frac{\lambda}{\alpha} = -\omega^2$, giving the general solutions

$$X(x) = Acos\omega x + Bsin\omega x$$

$$T(t) = C\exp(-\alpha\omega^2 t)$$

Applying the boundary conditions of $X(x) = 0$ at $x = \pm 2\pi$ gives $A = 0$ and B can be absorbed into the time-dependant term in the solution, leaving partial solutions of the form $X(x) = sin(\frac{nx}{2})$, $n = 0, 1, 2, \ldots$ since $\omega = \frac{n}{2}$ to satisfy boundary conditions. The full general solution is then

$$u(x,t) = \sum_{n=1}^{\infty} C_n \exp\left(\frac{-n^2\alpha t}{4}\right) sin\left(\frac{nx}{2}\right)$$

For example, for an initial condition of $u(x,0) = sin(x)$, we have $C_2 = 1$ and $C_i = 0$ for all $i \neq 2$. Thus, the solution should decay as

$$\frac{u(x,t+\Delta t)}{u(x,t)} = \exp(-\alpha\Delta t)$$

and for $u(x,0) = sin(x/2)$, we have $C_1 = 1$ and $C_i = 0$ for all $i \neq 1$, implying the solution decays as

$$\frac{u(x,t+\Delta t)}{u(x,t)} = \exp\left(-\frac{\alpha}{4}\Delta t\right)$$

The numerical solution for these initial conditions matches the decay rate computed above as can be seen in Fig. B.1. These simulations used a time step of $t = 0.01$ and a nodal expansion basis of order $P = 16$ with $Q = 17$ quadrature points.

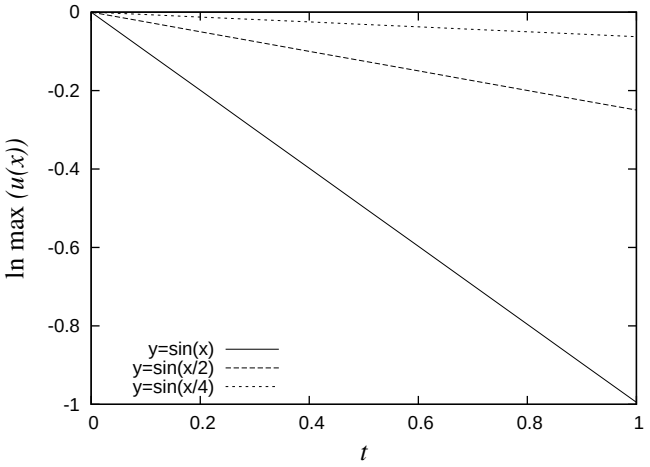

Figure B.1: Plot showing decay rate of numerical simulations of three different sine waves. Gradients match the decay rate results found through the analytical solution.

B.2 Solving the 2D Heat Equation

We solve the 2D heat equation $\frac{\partial \mathbf{u}}{\partial t} = \nabla^2 \mathbf{u}$, which in expanded form is

$$\frac{\partial}{\partial t}u(x,y,t) = \frac{\partial^2}{\partial x^2}u(x,y,t) + \frac{\partial^2}{\partial y^2}u(x,y,t) \tag{B.2a}$$

$$u(x,y,0) = \mathbf{u_0} = sin(mx)sin(my) \tag{B.2b}$$

on the domain $\Omega = [-\pi,\pi]\times[-\pi,\pi]$ with zero Dirichlet boundary conditions $u(\partial\Omega) = 0$. Typical $m \in \mathbb{N}$, although any value for which u_0 satisfies the boundary conditions is acceptable.

The spectral element formulation follows in a similar manner to that described in the one-dimensional formulation, resulting in the same high-level matrix equation, although involving a matrix with more structure, as discussed earlier in this section.

B.2.1 Validation of Results

To validate the spectral element solution, we derive the decay rate of the solution using Fourier analysis. Consider the two-dimensional Fourier expansion

$$u(x,y,t) = \sum_{k_1}\sum_{k_2} \hat{u}_{k_1,k_2} e^{ik_1 x} e^{ik_2 y}.$$

Expressing Eqn. (B.2a) in terms of this expansion gives

$$\begin{aligned}
\sum_{k_1}\sum_{k_2} \frac{\partial \hat{u}_{k_1,k_2}(t)}{\partial t} e^{ik_1 x} e^{ik_2 y} &= \sum_{k_1}\sum_{k_2} \Big[-k_1^2 \hat{u}_{k_1,k_2}(t) e^{ik_1 x} e^{ik_2 y} \\
&\qquad + -k_2^2 \hat{u}_{k_1,k_2}(t) e^{ik_1 x} e^{ik_2 y} \Big] \\
\Rightarrow \frac{\partial \hat{u}_{k_1,k_2}(t)}{\partial t} &= -(k_1^2 + k_2^2)\hat{u}_{k_1,k_2}(t) \quad \text{for each } k_1, k_2 \\
\Rightarrow \hat{u}_{k_1,k_2}(t) &= e^{-(k_1^2+k_2^2)t} \hat{u}_{k_1,k_2}(0).
\end{aligned}$$

If we consider the initial condition given in Eqn. (B.2b) then by expressing the sine function in terms of exponential functions as $sin(z) = \frac{1}{2i}(e^{iz} - e^{-iz})$ we get

$$\begin{aligned}
u(x,y,0) &= -\frac{1}{4}\left(e^{imx} - e^{-imx}\right)\left(e^{imy} - e^{-imy}\right) \\
&= -\frac{1}{4}\left(e^{imx}e^{imy} - e^{-imx}e^{imy} - e^{imx}e^{-imy} + e^{-imx}e^{-imy}\right).
\end{aligned}$$

Therefore, the initial condition consists of four modes, each with decay rate $-(k_1^2+k_2^2) = 2m^2$, and so we expect our solution to decay at the same rate. Results from the spectral element code are presented in Fig. B.2 which match the above analytical result.

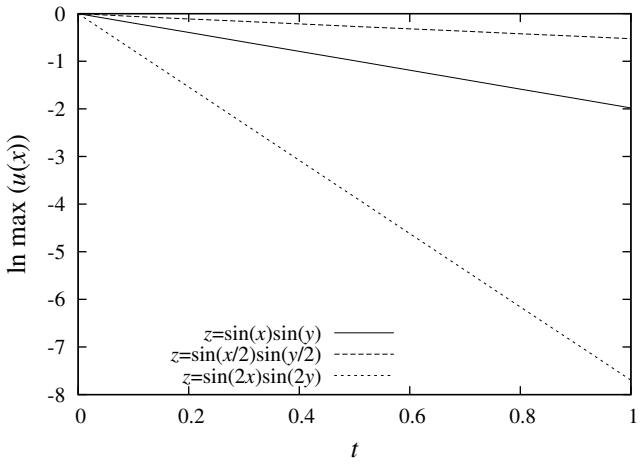

Figure B.2: Plot showing decay rate of numerical simulations of three different two-dimensional sine functions. The gradient matches the decay rate found through Fourier analysis of the problem.

Bibliography

N. Abdessemed, A. S. Sharma, S. J. Sherwin, and V. Theofilis. Transient growth analysis of the flow past a circular cylinder. *Phys. Fluids*, 21:044103, 2009.

A. Acrivos and M. L. Schrader. Steady flow in a sudden expansion at high reynolds numbers. *Phys. Fluids*, 25(6):923–930, June 1982.

E. Åkervik, J. Hœpffner, U. Ehrenstein, and D. S. Henningson. Optimal growth, model reduction and control in a separated boundary-layer flow using global eigenmodes. *J. Fluid Mech.*, 579:305–314, 2007.

W.E. Arnoldi. The principle of minimized iterations in the solution of the matrix eigenvalue problem. *Quart. Appl. Math.*, 9:17–29, 1951.

L. H. Back and E. J. Roschke. Shear-layer flow regimes and wave instabilities and reattachment lengths downstream of an abrupt circular channel expansion. *ASME J. Appl. Mech*, 39:677–681, September 1972.

D. Badekas and D. D. Knight. Eddy correlations for laminar axisymmetric sudden expansion flows. *ASME J. Fluid Engng*, 114:119–121, March 1992.

P. R. Bandyopadhyay. Aspects of the equilibrium puff in transitional pipe flow. *J. Fluid Mech.*, 163:439–458, 1986.

D. Barkley and R. D. Henderson. Three-dimensional Floquet stability analysis of the wake of a circular cylinder. *J. Fluid Mech.*, 322:215–241, 1996.

D. Barkley, M. G. M. Gomes, and R. D. Henderson. Three-dimensional instability in flow over a backward-facing step. *J. Fluid Mech.*, 473:167–190, 2002.

D. Barkley, H. M. Blackburn, and S. J. Sherwin. Direct optimal growth analysis for timesteppers. *Intnl J. Num. Meth. Fluids*, 57:1437–1458, 2008.

J. Beaudoin, O. Cadot, J. Aider, and J.Wesfreid. Three-dimensional stationary flow over a backward-facing step. *Eur. J. Mech. B/Fluids*, 23:147–155, 2004.

L. Bergström. Optimal growth of small disturbances in pipe Poiseuille flow. *Phys. Fluids*, A5(11):2710–20, November 1993.

A. Bers. Linear waves and instabilities. *Physique des plasmas*, 1:117, 1975.

C. Bertolotti, V. Deplano, J. Fuseri, and P. Dupouy. Numerical and experimental models of post-operative realistic flows in stenosed coronary bypasses. *J. Biomechanics*, 34: 1049–1064, 2001.

H. M. Blackburn and S. J. Sherwin. Formulation of a Galerkin spectral element–Fourier method for three-dimensional incompressible flows in cylindrical geometries. *J. Comput. Phys.*, 197:759–778, 2004.

H. M. Blackburn and S. J. Sherwin. Instability modes and transition of pulsatile stenotic flow: Pulse-period dependence. *J. Fluid Mech.*, 573:57–88, 2007.

H. M. Blackburn, D. Barkley, and S. J. Sherwin. Convective instability and transient growth in flow over a backward-facing step. *J. Fluid Mech.*, 603:271–304, 2008a.

H. M. Blackburn, S. J. Sherwin, and D. Barkley. Convective instability and transient growth in steady and pulsatile stenotic flows. *J. Fluid Mech.*, 607:267–277, 2008b.

R. J. Briggs. *Electron-stream interaction with plasmas*. MIT press Cambridge, 1964.

K. M. Butler and B. Farrell. Three-dimensional optimal perturbations in viscous shear flow. *Phys. Fluids A*, 4(8):1637–1650, 1992.

C. D. Cantwell, D. Barkley, and H. M. Blackburn. Transient growth analysis of flow through a sudden expansion in a circular pipe. *Submitted to Physics of Fluids*, 2009.

J. M. Chomaz. Global instabilities in spatially developing flows: non-normality and nonlinearity. *Annu. Rev. Fluid Mech.*, 37:357–392, 2005.

J. M. Chomaz, P. Huerre, and L. G. Redekopp. Bifurcations to local and global modes in spatially developing flows. *Phys. Rev. Let.*, 60(1):25–28, 1988.

J. M. Chomaz, P. Huerre, and L. G. Redekopp. A frequency selection criterion in spatially developing flows. *Stud. App. Math.*, 84(2):119–144, 1991.

K. A. Cliffe, E. J. C. Hall, and P. Houston. A numerical investigation of the bifurcation structure of flow in a pipe with a sudden expansion. To be published.

C. Cossu and J. M. Chomaz. Global measures of local convective instabilities. *Phys. Rev. Let.*, 78(23):4387–4390, 1997.

A. G. Darbyshire and T. Mullin. Transition to turbulence in constant-mass-flux pipe flow. *J. Fluid Mech.*, 289:83–114, 1995.

R. J. Deissler. Spatially growing waves, intermittency, and convective chaos in an open-flow system. *Physica D*, 25(1-3):233–260, 1987.

P. G. Drazin and W. H. Reid. *Hydrodynamic stability*. Cambridge University Press, 1981.

D. Drikakis. Bifurcation phenomena in incompressible sudden expansion flows. *Phys. Fluids*, 9(1):76–87, January 1997.

F. Durst, J. C. F. Pereira, and C. Tropea. The plane symmetric sudden-expansion flow at low reynolds numbers. *J. Fluid Mech.*, 248:567–581, 1993.

U. Ehrenstein and F. Gallaire. On two-dimensional temporal modes in spatially evolving open flows: the flat-plate boundary layer. *JFM*, 536:209–218, 2005.

R. M. Fearn, T. Mullin, and K. A. Cliffe. Nonlinear flow phenomena in a symmetric sudden expansion. *J. Fluid Mech.*, 211:595–608, 1990.

I. A. Feuerstein, G. K. Pike, and G. F. Round. Flow in an abrupt expansion as a model for biological mass transfer experiments. *J. Biomechanics*, 8:41–51, 1975.

N. Furuichi, Y. Takeda, and M. Kumada. Spatial structure of the flow through an axisymmetric sudden expansion. *Expts Fluids*, 34:643–650, 2003.

C. W. Gear. *Numerical Initial Value Problems in Ordinary Differential Equations*. Prentice Hall PTR, 1971. ISBN 0136266061.

F. Giannetti and P. Luchini. Structural sensitivity of the first instability of the cylinder wake. *J. Fluid Mech.*, 581:167–197, 2007.

G. H. Golub and C. F. Van Loan. *Matrix computations*. Johns Hopkins Univ Pr, 1996.

M. D. Griffith, T. Leweke, M. C. Thompson, and K. Hourigan. Steady inlet flow in stenotic geometries: convective and absolute instabilities. *J. Fluid Mech.*, 616:111–133, 2008.

K. J. Hammad, M. V. Otugen, and E. B. Arik. A piv study of the laminar axisymmetric sudden expansion flow. *Expts Fluids*, 26:266–272, 1999.

D. A. Hammond and L. G. Redekopp. Local and global instability properties of separation bubbles. *Eur. J. Mech. B/Fluids*, 17(2):145–164, 1998.

R. D. Henderson and G. E. Karniadakis. Unstructured spefctral element methods for simulation of turbulent flows. *J. Comput. Phys.*, 122:191–217, 1995.

D. S. Henningson and E. Åkervik. The use of global modes to understand transition and perform flow control. *Phys. Fluids*, 20:031302, 2008.

P. Huerre and P. A. Monkewitz. Local and global instabilities in spatially developing flows. *Annu. Rev. Fluid Mech.*, 22(1):473–537, 1990.

A. Iribarne, F. Frantisak, R. Hummel, and J. Smith. An experimental study of instabilities and other flow properties of a laminar pipe jet. *A. I. Ch. E. J.*, 18(4):689–698, 1972.

L. Kaiktsis, G. E. Karniadakis, and S. A. Orszag. Onset of three-dimensionality, equilibria, and early transition in flow over a backward-facing step. *J. Fluid Mech.*, 231: 501–528, 1991.

L. Kaiktsis, G. E. Karniadakis, and S. A. Orszag. Unsteadiness and convective instabilities in two-dimensional flow over a backward-facing step. *J. Fluid Mech.*, 321: 157–187, 1996.

G. E. Karniadakis and S. J. Sherwin. *Spectral/hp Element Methods for Computational Fluid Dynamics*. Oxford University Press, second edition, 2005.

G. E. Karniadakis, M. Israeli, and S. A. Orszag. High-order splitting methods for the incompressible navier-stokes equations. *J. Comput. Phys.*, 97:414–443, 1991.

L. Kelvin. Stability of fluid motion: rectilinear motion of viscous fluid between two parallel plates. *Phil. Mag*, 24(5):188–196, 1887.

D. J. Latornell and A. Pollard. Some observations on the evolution of shear layer instabilities in laminar flow through axisymmetric sudden expansions. *Phys. Fluids*, 29(9):2828–2835, September 1986.

P. Le Gal and V. Croquette. Visualization of the space-time impulse response of the subcritical wake of a cylinder. *Phys. Rev. E*, 62(3):4424–4426, 2000.

E. O. Macagno and T.-K. Hung. Computational and experimenal study of a captive annular eddy. *J. Fluid Mech.*, 28(1):43–64, 1967.

X. Mao, S. J. Sherwin, and H. M. Blackburn. Transient growth and bypass transition in stenotic flow with a physiological waveform. *Theoret. Comput. Fluid Dynamics*, 2009. ISSN 0935-4964.

O. Marquet, J. M. Chomaz, D. Sipp, J. Laurent, and M. Lombardi. Direct and adjoint global modes of a recirculation bubble: Lift-up and convective nonnormalities. *J. Fluid Mech.*, 622:1–21, 2008a.

O. Marquet, D. Sipp, J. M. Chomaz, and L. Jacquin. Amplifier and resonator dynamics of a low-Reynolds number recirculation bubble in a global framework. *J. Fluid Mech.*, 605:429–443, 2008b.

O. Marquet, D. Sipp, and J. Laurent. Sensitivity analysis and passive control of the cylinder flow. *J. Fluid Mech.*, 615:221–252, 2008c.

P. A. Monkewitz. The absolute and convective nature of instability in two-dimensional wakes at low reynolds numbers. *Phys. Fluids*, 31:999, 1988.

T. Mullin and J. Peixinho. Transition to turbulence in pipe flow. *J. Low Temp. Phys.*, 145(1):75–88, 2006.

T. Mullin, J. R. T. Seddon, M. D. Mantle, and A. J. Sederman. Bifurcation phenomena in the flow through a sudden expansion in a circular pipe. *Phys. Fluids*, 21:014110–1–6, 2009.

G. Mutschke, G. Gerbeth, V. Shatrov, and A. Tomboulides. Two-and three-dimensional instabilities of the cylinder wake in an aligned magnetic field. *Phys. Fluids*, 9:3114, 1997.

B. R. Noack and H. Eckelmann. A global stability analysis of the steady and periodic cylinder wake. *J. Fluid Mech.*, 270:297–330, 1994.

W. M. F. Orr. The stability or instability of the steady motions of a perfect liquid and of a viscous liquid. part ii: A viscous liquid. In *Proceedings of the Royal Irish Academy. Section A: Mathematical and Physical Sciences*, pages 69–138. Hodges, Figgis, & Co., 1907.

S. A. Orszag, M. Israeli, and M. O. Deville. Boundary conditions for incompressible flows. *J. Sci. Comp.*, 1(1):75–111, 1986.

A. T. Patera. A spectral element method for fluid dynamics: Laminar flow in a channel expansion. *J. Comput. Phys.*, 54:468–488, 1983.

J. Peixinho and T. Mullin. Decay of turbulence in pipe flow. *Phys. Rev. Let.*, 96(9): 94501, 2006.

J. Peixinho and T. Mullin. Finite-amplitude thresholds for transition in pipe flow. *J. Fluid Mech.*, 582:169–178, 2007.

B. Pier. On the frequency selection of finite-amplitude vortex shedding in the cylinder wake. *J. Fluid Mech.*, 458:407–417, 2002.

A. Pollard. A contribution on the effects of inlet conditions when modelling stenoses using sudden expansions. *J. Biomechanics*, 14(5):349–355, 1981.

W. H. Press, S. A. Teukolsky, W. T. Vetterling, and B. P. Flannery. *Numerical Recipes in C*. Cambridge University Press, 1992.

I. Proudman and J. R. A. Pearson. Expansions at small reynolds numbers for the flow past a sphere and a circular cylinder. *J. Fluid Mech.*, 2(03):237–262, 1957.

M. Provansal, C. Mathis, and L. Boyer. Benard-von karman instability: transient and forced regimes. *J. Fluid Mech.*, 182:1–22, 1987.

L. Rayleigh. On the instability of jets. *Proc. Lon. Math. Soc.*, 1(1):4, 1878.

L. Rayleigh. Investigation of the character of the equilibrium of an incompressible heavy fluid of variable density. *Proc. Lon. Math. Soc.*, 14(1):170–177, 1883.

S. C. Reddy and D. S. Henningson. Energy growth in viscous channel flows. *J. Fluid Mech.*, 252:209–238, 1993.

O. Reynolds. An experimental investigation of the circumstances which determine whether the motion of water shall be direct or sinuous, and of the law of resistance in parallel channels. *Phil. Trans. Roy. Soc. Lond. A*, pages 935–982, 1883.

E. J. Roschke and L. H. Back. The influence of upstream conditions on flow reattachment lengths downstream of an abrupt circular channel expansion. *J. Biomechanics*, 9:481–483, 1976.

P. J. Schmid and D. S. Henningson. Optimal energy density growth in Hagen–Poiseuille flow. *J. Fluid Mech.*, 277:197–225, 1994.

P. J. Schmid and D. S. Henningson. *Stability and transition in shear flows*. Springer Verlag, 2001.

H. Shan, B. Ma, Z. Zhang, and F. T. M. Nieuwstadt. Direct numerical simulation of a puff and a slug in transitional cylindrical pipe flow. *J. Fluid Mech.*, 387:39–60, 1999.

S. J. Sherwin and H. M. Blackburn. Three-dimensional instabilities and transition of steady and pulsatile axisymmetric stenotic flows. *J. Fluid Mech.*, 533:297–327, 2005.

K. R. Sreenivasan and P. J. Strykowski. An instability associated with a sudden expansion in a pipe flow. *Phys. Fluids*, 26(10):2766–2768, October 1983.

R. G. Teyssandier and M. P. Wilson. An analysis of flow through sudden enlargements in pipes. *J. Fluid Mech.*, 64(1):85–95, 1974.

C. E. Tinney, M. N. Glauser, E. L. Eaton, and J. A. Taylor. Low-dimensional azimuthal characteristics of suddenly expanding axisymmetric flows. *J. Fluid Mech.*, 567:141–155, 2006.

L. N. Trefethen and M. Embree. *Spectra and Pseudospectra: the behavior of non-normal matrices and operators*. Princeton University Press, 2005.

L. S. Tuckerman and D. Barkley. Bifurcation analysis for timesteppers. In E. Doedel and L. S. Tuckerman, editors, *Numerical Methods for Bifurcation Problems and Large-Scale Dynamical Systems*, pages 453–566. Springer, 2000.

S. S. Varghese, S. H. Frankel, and P. F. Fischer. Direct numerical simulation of stenotic flows. part1. steady flow. *J. Fluid Mech.*, 582:253–280, 2007.

J. Vétel, A. Garon, D. Pelletier, and M.-I. Farinas. Asymmetry and transition to turbulence in a smooth axisymmetric constriction. *J. Fluid Mech.*, 607:351–386, 2008.

A. P. Willis and R. R. Kerswell. Critical behavior in the relaminarization of localized turbulence in pipe flow. *Phys. Rev. Let.*, 98(1):14501, 2007.

I. J. Wygnanski and F. H. Champagne. On transition in a pipe. part 1. the origin of puffs and slugs and the flow in a turbulent slug. *J. Fluid Mech.*, 59(02):281–335, 1973.

I. J. Wygnanski, M. Sokolov, and D. Friedman. On transition in a pipe. part 2. the equilibrium puff. *J. Fluid Mech.*, 69(02):283–304, 1975.

X. Yang and A. Zebib. Absolute and convective instability of a cylinder wake. *Phys. Fluids A*, 1:689, 1989.

H. Q. Zhang, U. Fey, B. R. Noack, M. König, and H. Eckelmann. On the transition of the cylinder wake. *Phys. Fluids*, 7:779, 1995.